# Tensor Analyzing Power Measurements for $D(d,p)^3H$ and $D(d,n)^3He$ at Very Low Energies

**Kurtis A. Fletcher**

**University of North Carolina-Chapel Hill**

A dissertation submitted to the faculty of the University of North Carolina in partial fulfillment of the requirements for the degree of Doctor of Philosophy in the Department of Physics and Astronomy.

Chapel Hill, North Carolina

1992

Approved by

E. J. Ludwig, Advisor

W. J. Thompson, Reader

H. J. Karwowski, Reader

**KURTIS A. FLETCHER. Tensor Analyzing Power Measurements for D(d,p)$^3$H and D(d,n)$^3$He at Very Low Energies (Under the direction of Edward J. Ludwig.)**

## ABSTRACT

Angular distributions of the tensor analyzing powers $A_{zz}$ and $A_{xx}$-$A_{yy}$ have been measured for the fusion reactions D(d,p)$^3$H and D(d,n)$^3$He at incident deuteron energies of 25, 40, 60, and 80 keV. Precise measurements of these observables are necessary to reveal the mechanisms which govern these complex charge-symmetric reactions, to indicate the effect of polarization on fusion reaction rates, and to provide additional information for an on-going global analysis of the energy levels of $^4$He. To collect these data, which are among the lowest energy analyzing powers ever measured, a low energy beam facility was constructed, novel thin film deuterated targets were fabricated, and a deuteron tensor polarimeter was designed and calibrated. The data indicate that entrance quintet S waves are important for these reactions, and that the use of polarized fuel would not produce an aneutronic fusion reactor. These analyzing power distributions are compared to other recent data at low energies, to R-matrix predictions made without these data, and to a global R-matrix parametrization which includes these data.

# ACKNOWLEDGMENTS

To a greater extent than most scholarly endeavors, experimental nuclear physics is a group activity. I have been fortunate to work with talented, dedicated people, and their hard work has made this thesis research possible. Professors Ed Ludwig, Hugon Karwowski, Bill Thompson, and Tom Clegg provided me with valuable (and occasionally conflicting) advice and were always available to help me wrestle with experimental problems. The combined talents and experience of these gentlemen are a great asset to any graduate student.

Many people, especially Drs. Ludwig and Karwowski, spent long hours working on my data-collection runs. These include our post-doctoral researchers Dr. Rupak Das and Dr. Zeid Ayer, and my colleagues Dr. Eric Crosson, Dr. Susan Lemieux, Tim Black, Jeff Blackmon, Dennis Dinge, Beata Kozlowska, Lijun Ma, Tony Ackley, Brian Hendrix, and Colin "Taz" Philp. While I am very thankful for their time and energy, I am even more grateful for their friendship and understanding.

My research lead me to Los Alamos National Labs, where I was treated to the hospitality of Dr. Gerry Hale and the members of the Nuclear Theory and Applications Group. I was able to investigate some of the effects of including my data in the R-matrix parametrization thanks to Gerry's efforts. Dr. Yoshihiro Tagishi of the University of Tsukuba, Japan, taught us how to deposit deuterated parapolyphenyl targets during a visit here. He also provided us with addition DPP powder which was very useful for collecting the 25 keV data.

The construction of the original Low Energy Beam Facility was aided by the excellent technical staff of the Triangle Universities Nuclear Lab: Ken Sweeton, Paul Carter, Sidney Edwards, Pat Mulkey, and Al Lovette. In addition to being proficient in technical areas, these folks are very good teachers, contributing to the educational mission of TUNL.

My graduate school experience was profoundly enriched by my participation with the UNC Lutheran Campus Ministry community and Holy Trinity Lutheran Church. I am indebted to my many friends at LCM for their support and to my pastor, Larry Hartsell, one of the "teachers of the law" referred to in Matthew 13:52.

Finally, I am thankful for the encouragement and sacrifices of my parents, grandparents, in-laws, and siblings. Most of all, I am thankful for my wife, Leah, who gave me a fortune cookie insert which sums up our marriage: "Life to you is a dashing and bold adventure." I look forward to many more shared adventures.

As J.S. Bach wrote on his manuscripts, "Soli Deo Gloria."

# TABLE OF CONTENTS

# LIST OF TABLES

# LIST OF FIGURES

# I. Introduction: Genesis of this project

Precise and accurate determinations of tensor analyzing powers for $D(d,p)^3H$ and $D(d,n)^3He$ at low energies are useful for uncovering the reaction mechanisms of these surprisingly complex reactions, for evaluating the proposal that using polarized ions in a $^3He(d,p)^4He$ fusion reactor would eliminate the production of neutrons [Kul82], and for investigating the $^4He$ energy levels using the R-matrix parametrization. For these reasons we have measured angular distributions of the Cartesian analyzing powers $A_{zz}$ and $A_{xx}$-$A_{yy}$.

In this chapter, after a brief overview to introduce the research topic, we discuss the motivations for this inquiry, review the previous theoretical approaches to the system, and present recent experimental results. Lastly, we mention limitations which prevented us from measuring other polarization observables.

## 1.1 Overview

To study the $D(d,p)^3H$ and $D(d,n)^3He$ fusion reactions, we have completed angular distribution measurements of two tensor analyzing powers at deuteron bombarding energies of 25, 40, 60, and 80 keV. An analyzing power is a ratio between a cross section measured with a beam of ions prepared with magnetic substates unequally populated (polarized beam) and a cross section measured with equal population of the magnetic substates (unpolarized beam). A review of the formalism and definitions pertaining to measurements with polarized beams and unpolarized targets is presented in Appendix A. Because of the high Q-values for the reactions ($Q_{(d,p)}$ = 4.033 MeV and $Q_{(d,n)}$ = 3.269 MeV), all three charged-particle groups

were easily measured simultaneously in surface-barrier, charged-particle detectors. The data from the $^3$H and $^3$He peaks were converted to the center-of-mass angles for (d,p) and (d,n), respectively. The results are compared with those of other researchers and with the expectations from a global fit to the four-nucleon system. They are included in a new version of this fit.

Because this was our first experience with very low energy nuclear physics and with a new type of polarized ion source, we spent a great deal of time developing thin film deuterated targets, novel ways of collecting analyzing power data with rapid changing of spin states, and a new experimental station, the Low Energy Beam Facility (LEBF) at the Triangle Universities Nuclear Laboratory (TUNL). In the process, we calibrated a deuteron tensor polarimeter useful for this energy range.

## 1.2 Motivation for this project

There are at least three related reasons why analyzing power measurements for D(d,p)$^3$H and D(d,n)$^3$He are of interest. The reaction mechanisms which govern these two reactions are complicated and cannot be established by cross section measurements alone, making polarization experiments necessary. It has also been suggested [Kul82] that polarizing the deuterium plasma in future fusion reactors would improve their efficiency. Measurements of the analyzing powers, particularly $A_{xx}$-$A_{yy}$, test the conditions necessary for this hypothesis [Hof86]. Finally, additional data on the $^4$He system contribute to the charge-independent R-matrix analyses being made at Los Alamos National Laboratory (LANL) by G.M. Hale [Hal80].

### 1.2.1 D(d,p)$^3$H and D(d,n)$^3$He reaction mechanism

Cross section and analyzing power data indicate that the D(d,p)$^3$H and D(d,n)$^3$He reactions are governed primarily by transitions from S-, P-, and D-waves in the entrance channel. The presence of higher order partial waves greatly increases the

complexity of the reaction mechanism. In a transition matrix element analysis by Ad'yasevich [Ady69], continued by Lemaître [Lem90], sixteen complex matrix elements are included for each reaction. These are listed in Table 1.1. Using the notation of [Lem90] and [Ady69] with 'a' indicating the entrance channel and 'e' the exit channel, the matrix elements are $\left\langle {}^{2S_a+1}l_{a_J} \left| J^{\pi} \right| {}^{2S_e+1}l_{e_J} \right\rangle$.

Table 1.1. Matrix elements for D(d,p) and D(d,n) in the notation of [Ady69].

| | |
|---|---|
| $\alpha_0 = \left\langle {}^1S_0 \left\| 0^+ \right\| {}^1S_0 \right\rangle$ | $\gamma_1 = \left\langle {}^5S_2 \left\| 2^+ \right\| {}^1D_2 \right\rangle$ |
| $\alpha_{10} = \left\langle {}^3P_0 \left\| 0^- \right\| {}^3P_0 \right\rangle$ | $\gamma_2 = \left\langle {}^5D_0 \left\| 0^+ \right\| {}^1S_0 \right\rangle$ |
| $\beta_{11} = \left\langle {}^3P_1 \left\| 1^- \right\| {}^1P_1 \right\rangle$ | $\gamma_3 = \left\langle {}^5D_2 \left\| 2^+ \right\| {}^1D_2 \right\rangle$ |
| $\alpha_{11} = \left\langle {}^3P_1 \left\| 1^- \right\| {}^3P_1 \right\rangle$ | $\delta_1 = \left\langle {}^5S_2 \left\| 2^+ \right\| {}^3D_2 \right\rangle$ |
| $\alpha_{12} = \left\langle {}^3P_2 \left\| 2^- \right\| {}^3P_2 \right\rangle$ | $\delta_2 = \left\langle {}^5D_1 \left\| 1^+ \right\| {}^3S_1 \right\rangle$ |
| $\alpha_2 = \left\langle {}^1D_2 \left\| 2^+ \right\| {}^1D_2 \right\rangle$ | $\delta_3 = \left\langle {}^5D_1 \left\| 1^+ \right\| {}^3D_1 \right\rangle$ |
| $\beta_2 = \left\langle {}^1D_2 \left\| 2^+ \right\| {}^3D_2 \right\rangle$ | $\delta_4 = \left\langle {}^5D_3 \left\| 3^+ \right\| {}^3D_3 \right\rangle$ |
| $\alpha_3 = \left\langle {}^3P_2 \left\| 2^- \right\| {}^3F_2 \right\rangle$ | $\delta_5 = \left\langle {}^5D_2 \left\| 2^+ \right\| {}^3D_2 \right\rangle$ |

It is instructive to ask why these sixteen elements of the transition matrix, and no others, are included. The first assumption made is that $l_a \leq 2$. In the entrance channel, the channel spin of the two spin-1 deuterons can be 0, 1, or 2. The channel spin in the exit channel can be 0 or 1. By parity conservation, the orbital angular momenta in the entrance and exit channels must both be even or both be odd. The identical particles in the entrance channel provide a further symmetry rule: the sum of the entrance channel orbtial angular momentum and channel spin must be even. This leads to a restriction on the unpolarized cross section that only even-order Legendre polynomials can enter in the expansion of $\sigma(\theta)$. Finally, it is also assumed that the orbital momentum in the exit channel is restricted to $l_e \leq 3$. A tabular representation in figure 1-1 illustrates which matrix elements are eliminated and why.

| | | $S_e$ | 0 | 1 | 0 | 1 | | | 0 | 1 | | | 0 | 1 | | |
|---|---|---|---|---|---|---|---|---|---|---|---|---|---|---|---|---|
| | | $\ell_e$ | 0 | 1 | 1 | 0 | 1 | 2 | 2 | 1 | 2 | 3 | 3 | 2 | 3 | 4 |
| $S_a$ | $\ell_a$ | J | 0 | | 1 | | | | 2 | | | | 3 | | | |
| 0 | 0 | 0 | $\alpha_0$ | $\pi$ | | | | | | | | | | | | |
| 1 | 1 | | $\pi$ | $\alpha_{10}$ | | | | | | | | | | | | |
| 2 | 2 | | $\gamma_2$ | $\pi$ | | | | | | | | | | | | |
| 0 | 1 | 1 | | | $\langle\ \rangle$ | $\langle\pi\rangle$ | $\langle\ \rangle$ | $\langle\pi\rangle$ | | | | | | | | |
| 1 | 0 | | | | $\langle\pi\rangle$ | $\langle\ \rangle$ | $\langle\pi\rangle$ | $\langle\ \rangle$ | | | | | | | | |
| | 1 | | | | $\beta_{11}$ | $\pi$ | $\alpha_{11}$ | $\pi$ | | | | | | | | |
| | 2 | | | | $\langle\pi\rangle$ | $\langle\ \rangle$ | $\langle\pi\rangle$ | $\langle\ \rangle$ | | | | | | | | |
| 2 | 1 | | | | $\langle\ \rangle$ | $\langle\pi\rangle$ | $\langle\ \rangle$ | $\langle\pi\rangle$ | | | | | | | | |
| | 2 | | | | $\pi$ | $\delta_2$ | $\pi$ | $\delta_3$ | | | | | | | | |
| | 3 | | | | $\langle\_\rangle$ | $\langle\underline{\pi}\rangle$ | $\langle\_\rangle$ | $\langle\underline{\pi}\rangle$ | | | | | | | | |
| 0 | 2 | 2 | | | | | | | $\alpha_2$ | $\pi$ | $\beta_2$ | $\pi$ | | | | |
| 1 | 1 | | | | | | | | $\pi$ | $\alpha_{12}$ | $\pi$ | $\alpha_3$ | | | | |
| | 2 | | | | | | | | $\langle\ \rangle$ | $\langle\pi\rangle$ | $\langle\ \rangle$ | $\langle\pi\rangle$ | | | | |
| | 3 | | | | | | | | $\underline{\pi}$ | $\_$ | $\underline{\pi}$ | $\_$ | | | | |
| 2 | 0 | | | | | | | | $\gamma_1$ | $\pi$ | $\delta_1$ | $\pi$ | | | | |
| | 1 | | | | | | | | $\langle\pi\rangle$ | $\langle\ \rangle$ | $\langle\pi\rangle$ | $\langle\ \rangle$ | | | | |
| | 2 | | | | | | | | $\gamma_3$ | $\pi$ | $\delta_5$ | $\pi$ | | | | |
| | 3 | | | | | | | | $\langle\underline{\pi}\rangle$ | $\langle\_\rangle$ | $\langle\underline{\pi}\rangle$ | $\langle\_\rangle$ | | | | |
| | 4 | | | | | | | | $\_$ | $\underline{\pi}$ | $\_$ | $\underline{\pi}$ | | | | |
| 0 | 3 | 3 | | | | | | | | | | | $\langle\_\rangle$ | $\langle\underline{\pi}\rangle$ | $\langle\_\rangle$ | $\langle\overline{\underline{\pi}}\rangle$ |
| 1 | 2 | | | | | | | | | | | | $\langle\pi\rangle$ | $\langle\ \rangle$ | $\langle\pi\rangle$ | $\langle^{-}\rangle$ |
| | 3 | | | | | | | | | | | | $\_$ | $\underline{\pi}$ | $\_$ | $\overline{\underline{\pi}}$ |
| | 4 | | | | | | | | | | | | $\langle\underline{\pi}\rangle$ | $\langle\_\rangle$ | $\langle\underline{\pi}\rangle$ | $\langle^{-}_{-}\rangle$ |
| 2 | 1 | | | | | | | | | | | | $\langle\ \rangle$ | $\langle\pi\rangle$ | $\langle\ \rangle$ | $\langle\overline{\underline{\pi}}\rangle$ |
| | 2 | | | | | | | | | | | | $\pi$ | $\delta_4$ | $\pi$ | $^{-}$ |
| | 3 | | | | | | | | | | | | $\langle\_\rangle$ | $\langle\underline{\pi}\rangle$ | $\langle\_\rangle$ | $\langle\overline{\underline{\pi}}\rangle$ |
| | 4 | | | | | | | | | | | | $\underline{\pi}$ | $\_$ | $\underline{\pi}$ | $^{-}_{-}$ |
| | 5 | | | | | | | | | | | | $\langle\_\rangle$ | $\langle\underline{\pi}\rangle$ | $\langle\_\rangle$ | $\langle\overline{\underline{\pi}}\rangle$ |

Figure 1-1. Tabular representation of the matrix elements for the $D(d,p)^3H$ and $D(d,n)^3He$ reactions. The entrance channel ("absorbed" channel) orbital angular momentum ($l_a$) and channel spin ($S_a$) are shown for each total angular momentum (J) along the vertical axis, and their exit channel ("emitted" channel) counterparts, ($l_e$ and $S_e$) are shown along the horizontal axis. The notation of [Ady69] is used to identify the matrix elements. The symbol "$\pi$" in a certain position indicates that the matrix element

with those angular momenta vanishes because of parity conservation. A bracket "⟨ ⟩" indicates that the matrix element vanishes because of identical particles in the entrance channel. An underline "_" indicates that the matrix element vanishes because of the assumption that only S, P, and D waves contribute in the entrance channel, and an overbar "‾" indicates that the matrix element vanishes because of the assumption that only S, P, D, and F waves contribute in the exit channel. Some matrix elements vanish for more than one reason, as shown.

Because of the absence of nearby resonances and the large Q-values for the reactions, the energy dependence of the matrix elements in the matrix element analysis of [Lem90] is assumed to be due to the entrance channel Coulomb penetrability and phase shift only. This still leaves 31 parameters (magnitude and phases of the transition amplitudes less one overall arbitrary phase) to be determined from a fit to the low energy data. Clearly, cross section measurements alone are not sufficient to determine the parameters. Analyzing power measurements, which are sensitive to interference terms between the matrix elements, are required for the determination of the reaction mechanism to be successful, and analyzing power measurements made at different energies may be useful in testing the energy dependence assumption of model. The analysis by [Lem90] is discussed in section 1.3.1.

Finally, simultaneous measurement of the two branches $D(d,p)^3H$ and $D(d,n)^3He$ allows for comparisons of the two reactions with data taken under identical conditions. Differential and total cross section measurements indicate differences in the two branches, as discussed in section 1.3.2. There are very small differences in the analyzing powers as well, and a possible reason for differences between the two branches is discussed in section 6.1.

### 1.2.2 Connection to fusion reactor design

As part of a discussion of the possible benefits of using polarized ions in the plasma of future fusion reactors, Kulsrud et al. [Kul82] suggested that the D-D reaction rates could be *enhanced* by a factor of two by initiating them with the target and projectile deuterons prepared in the $m_I = 0$ substates. Alternatively, the rates were predicted to be *suppressed* if the spins of the ions were all parallel to the magnetic field. These predictions were based on the results of [Ady69], as discussed in section 1.3.2. The complete suppression of the D-D reactions in a reactor based on $^3He(d,p)^4He$ would result in aneutronic fusion, thereby preventing the removal of energy from the plasma by neutrons and the activation of the reactor components by neutron bombardment.

Preparation of plasma ions with spins parallel to the quantization axis is equivalent to preparation of entrance channel $^5S_2$, or quintet S-states. If the neutrons and protons inside the deuterons are in a relative S-state, the Pauli principle would seem to dictate that the interaction of these configurations would be forbidden. Such arguments have been given to justify ignoring this configuration [Kon48], [Roo61]. As discussed in section 1.3.1, angle asymmetries about 90° in the tensor analyzing powers indicate the presence of entrance quintet S-waves.

### 1.2.3 A=4 parametrization: R-matrix

The parametrization of the four-nucleon system using the R-matrix, done predominantly by Hale at LANL [Hal80], [Hal90] has yielded new information regarding the levels in $^4He$ [Til92]. The specifics of the R-matrix technique and its application in this system are discussed in section 6.1. In essence it provides a global fit to data on total and differential cross sections, analyzing powers, polarizations, and polarization-transfer quantities for the various two-body channels of the $^4He$

system corresponding to excitation energies below 29 MeV. The R-matrix parameters (reduced-width amplitudes and energy levels) are varied to obtain the best fit to all the data simultaneously. Once the best-fit parameters are determined, they can be used to predict unmeasured observables. Analyzing power data at very low energies complement the cross section data in this energy range by providing a more complete data set for the determination of the R-matrix parameters and the S-matrix elements near the D+D threshold.

## 1.3 Review of previous work

The discussion surrounding the concept of polarized plasma fusion reactors (section 1.2.2) renewed interest in the very low energy aspects of $D(d,p)^3H$ and $D(d,n)^3He$ polarization observables. Although these are among the earliest nuclear reactions studied, several experimental and theoretical groups have recently contributed to an improved understanding of these reactions. Much of the recent work has been summarized in a review article by Schieck [Sch88], and in recent papers from the Köln group [Sch92], [Bec92]. In this section, some of the recent work will be summarized.

### 1.3.1 Theory

Though they may at first appear to be very simple, the $D(d,p)^3H$ and $D(d,n)^3He$ reactions have proven to be resistant to simple theoretical interpretation. Even at very low energies the reaction mechanisms are complex, with P- and D-waves in the entrance channel contributing even at energies below $E_d = 100$ keV. The "neutron-lean" or "aneutronic" polarized fusion plasma concept, which rests on the question of suppression of quintet S-states, generated a renewed interest in these reactions.

Even before the introduction of the polarized fusion question, Ad'yasevich and Fomenko [Ady69] investigated transition matrix elements up to D-waves in the entrance channel using the available data from 100 to 500 keV for the $D(d,p)^3H$ reaction. This

approach provided guidance for the later Köln matrix element fit, which included lower energy data and both reactions [Lem90]. In [Ady69], the correspondence between the matrix elements and the analyzing powers was indicated explicitly, and one interesting observation from this analysis was that any asymmetry about 90° in the tensor analyzing powers is a direct indication of the presence of quintet S-states. The authors gave values for the squares of several of the matrix elements and for several interference terms and reported that transitions from quintet states are present, but assumed them to be small. In a later analysis including their own data for both reactions [Ady81], the authors concluded that quintet S-state transitions were "significantly hindered" in $D(d,n)^3H$ as compared to $D(d,p)^3H$.

The transition matrix element fit of [Lem90] included available data on the $D(d,p)^3H$ and $D(d,n)^3He$ reactions below 500 keV. Data included total and differential cross sections, analyzing powers, and polarizations of outgoing particles. The energy dependence of the matrix elements was assumed to be due to Coulomb and centrifugal barriers in the entrance channel, and was factored out, leaving energy independent amplitudes to be determined from the fit. A set of these energy independent factors which provided the best fit to the data was determined for each reaction. The authors repeated the search from many different initial values in order to try to locate the absolute minimum of the $\chi^2$ surfaces. These results indicated that quintet S-waves and quintet D-waves are large and cannot be ignored in any analysis of these reactions. On the question of polarized fusion, the authors concluded that polarized reaction rates for the D-D reactions are actually larger than rates for unpolarized particles, so that polarizing the fuel in a fusion plasma reactor would actually have an adverse effect [Sch92].

Resonating group model (RGM) calculations [Hof84] indicated that transitions from quintet-S states were not suppressed and that the ratio of polarized to unpolarized cross sections was close to unity. In this article the authors suggested that channel spin

transitions such as $\Delta S=2$ were permitted because of the D-state component of $^3H$ and $^3He$, where all three nucleons have parallel spins. Entry into this configuration is mediated by the central force, without requiring the action of spin-orbit or tensor forces to flip the spin of a nucleon. A later analysis by Hofmann [Hof86] improved the resonating group model by using a more realistic nucleon-nucleon potential and by including D-states in the entering deuterons. His results agreed with R-matrix results from Hale. With the modified RGM, the authors reached the same conclusions; namely, that transitions from quintet S-states were about as large as those from singlet and triplet S-states.

However, Zhang et al. [Liu85,Zha86] calculated polarized and unpolarized $D(d,n)^3He$ cross sections below $E_{cm}$=150 keV using the distorted-wave Born approximation (DWBA) and claimed that the ratio of polarized to unpolarized cross sections was less than 10%, so that a neutron-lean reactor would be feasible. In support of their results, the authors remarked that their calculation of unpolarized cross section data was within 20% of the experimental data, whereas the RGM cross section calculation [Hof84 ] was a factor of two smaller than the data. They also expressed doubts that the quintet S-states could gain entry to the singlet and triplet D-waves via the central interaction with amplitudes as large as those for the singlet S-state transitions as suggested in [Hof84]. In a comment [Fic85], the RGM group expressed doubts about the applicability of DWBA for reactions involving light ions near threshold and defended their mechanism for generating large matrix elements for transitions from quintet S-waves.

The DWBA approach of [Zha86] came under further attack by the Surrey group [Abu88], who included all internal D-states for the nuclei in an approximate calculation which was a hybrid of the DWBA and RGM methods. This calculation overestimated the cross section by a factor of 120 at $E_{cm}$ = 55 keV. In trying to explain the superior agreement to data in [Zha86], the authors criticized Zhang et al. for using in their

calculation deuteron wavefunctions which were not eigenfunctions of the n-p Hamiltonian. In addition, the Surrey group used a more realistic d-$^3$He overlap wavefunction than Zhang et al.. They were able to reproduce the results of [Zha86] by using the improper wavefunction and d-$^3$He overlap, suggesting that the good agreement with data in [Zha86] is an accidental result of calculation deficiencies. Despite their poor agreement with the data, the authors of [Abu88] concluded that volume effects are more important than surface effects for these reactions at fusion energies.

A resonating group model calculation carried out by a Ukrainian group [Vas90] for D(d,p)$^3$H and D(d,n)$^3$He generated ratios of the D(d,p)$^3$H to D(d,n)$^3$He cross sections as well as the energy dependence of the astrophysical S-factors with quantitative agreement below 50 keV only. In this calculation, transitions from entrance channel D-waves and quintet S-waves were found to have little effect on the S-factor. However, there was quantitative disagreement between the calculation and the data of [Kra87] at energies above 50 keV, where Legendre expansions of cross section data have concluded that entrance D-waves are nonzero.

Koonin and Mukerjee [Koo90] compared the two reactions using second-order DWBA to examine whether the lack of neutrons detected in "cold fusion" experiments [Pao89] and discrepancies between data and theory in recent $^6$Li(d,p)$^7$Li and $^6$Li(d,n)$^7$Be measurements [Cec85] resulted from suppression of the neutron branch relative to the proton branch at very low energies caused by the Oppenheimer-Phillips mechanism (OP) [Opp35]. With the simplifying and erroneous assumption that deuterium is an infinitely massive target, and including only S-waves in the D-D channel, Koonin and Mukerjee concluded that OP corrections to $\sigma$(d,p)/$\sigma$(d,n) were smaller than 10% and relatively independent of energy in the region below $E_d$=2 MeV. No discussion was offered about the effect of the OP mechanism on polarized cross sections.

Estimates of electron screening effects in $D(d,p)^3H$ at very low energies have been discussed in reference to nuclear astrophysics. Assenbaum et al. [Ass87] used the Born-Oppenheimer approximation to give upper limits for the enhancement of the cross section for a screened nucleus over a bare nucleus. For $D(d,p)^3H$ they concluded that the enhancement is negligible at energies above 5 keV. In their model the cross section for a screened nucleus was written as the the product of an enhancement factor and the cross section for a bare nucleus. With such assumptions, electron screening should play no role in analyzing-power measurements, where ratios of cross sections are formed, provided that the enhancement factor is not spin dependent.

### 1.3.2 Experiments

In the 1980's two groups investigated the unpolarized differential cross sections for $D(d,p)^3H$ and $D(d,n)^3He$ to provide a more accurate determination of the astrophysical S-factor for these reactions and more accurate reaction rates for fusion reactors. Using the Los Alamos Low-Energy Fusion Cross Section apparatus, Brown and Jarmie [Bro90] used a windowless gas target to measure $D(d,p)^3H$ and $D(d,n)^3He$ cross section angular distributions at eleven energies from $E_d$=20 to 117 keV. They obtained data with standard deviations of about 2% and scale errors of 1.3%. Kraus et al. [Kra87] measured $D(d,p)^3H$ and $D(d,n)^3He$ angular distributions from $E_d$=6 to 325 keV using a supersonic gas jet target. They reported their results in terms of Legendre polynomial expansion coefficients, normalized so that $a_0$ is unity. There was slight disagreement between the two sets of measurements, although both groups concluded that there is larger angular asymmetry for $D(d,n)^3He$ than for $D(d,p)^3H$, that P-waves are present down to the lowest energies measured, and that D-waves are important at energies above about 60 keV.

Recent analyzing power measurements have been made at Moscow [Ady81], Giessen [Pfa85], Köln [Sch92, Bec92], and at Tsukuba, Japan [Tag92].

Ad'yasevich at al. [Ady81] measured angular distributions of $A_y$, $A_{zz}$, $A_{xz}$, and $A_{xx}$-$A_{yy}$ for both branches at bombarding energies ranging from 60 to 485 keV over an angular range in the laboratory frame from 20° to 150°. A gas target was used. The tensor polarization was monitored continuously using the $^3H(d,\alpha)n$ reaction and the vector polarization was inferred from the tensor polarization. Unfortunately, because these data are only available in graphical form, little can be said about them apart from the authors' conclusions. They concluded that the P-wave contributions are greater for $D(d,n)^3He$ than for $D(d,p)^3H$, and that quintet S-states are hindered in $D(d,n)^3He$ relative to $D(d,p)^3H$. This last conclusion was based upon the fact that the quantity $A_{zz}(0°)$-$A_{zz}(180°)$ was consistently smaller for $D(d,n)^3He$ than for $D(d,p)^3H$ for their data.

The Giessen group reported angular distributions for the vector analyzing power [Pfa85] of both reactions at 80, 160, 200, 460 keV, and 1 MeV. Measurements of the complete set of tensor analyzing powers have also been made over a similar energy range [Pfa89], but to date these have not been published. These researchers used deuterated parapolyphenyl thin films (see [Iri73] and section 2.3.2.2 of this work) as targets for their low energy work.

The Köln group has complemented their extensive fit of the $D(d,p)^3H$ and $D(d,n)^3He$ transition matrix elements [Lem90] with angular distributions of the four analyzing powers measured at a reaction energy of 28 keV for both branches [Bec92]. They also used deuterated parapolyphenyl thin films as targets, and accelerated the beam produced in their Lamb-shift source to tandem-accelerator energies to measure the beam polarizations. Although they stated that their results disagreed slightly with the R-matrix predictions of Hale, examination of their ($A_{xx}$-$A_{yy}$) data near 90° reveals considerable quantitative differences. The R-matrix prediction indicated a larger magnitude for this observable than the Köln results reported. By concentrating on a complete set of observables near 30 keV, the Köln group added data to their matrix

element fit at energies where the D-wave contributions are vanishingly small. Including their new data into the fit of [Lem90] did not substantially alter the conclusions of that analysis, which included that quintet S-states are not suppressed in either reaction and, therefore, the use of polarized fuel in a $^3$He(d,p)$^4$He-based reactor would not eliminate the neutrons arising from D(d,n)$^3$He. From an applied-physics point of view, these measurements were important because they were the first published analyzing power measurements made at energies which might be accessible by early-generation fusion reactors.

Tagishi et al. [Tag92] measured the four analyzing powers $iT_{11}$, $T_{20}$, $T_{21}$, and $T_{22}$ at $E_d$ = 30, 50, 70, and 90 keV for the D(d,p)$^3$H branch only. [For relations between the Cartesian and spherical analyzing powers, see section A.1, especially (A.12).] These measurements, as well as some unpublished data measured by them using the same apparatus, serve as the polarimeter calibration for the present work (see section 4.2). Deuterated parapolyphenyl targets were used, and the beam polarizations for beams produced using a Lamb-shift source were determined by the quench-ratio [Ohl71] of currents measured on target. At 30 keV near 90°, the observable $T_{22}$ measured by Tagishi et al. was larger in magnitude than that implied from the Köln values for $(A_{xx}-A_{yy})$. The data from [Tag92] are more consistent with the R-matrix predictions than are the Köln data.

A schematic showing the experimental situation for the analyzing-power measurements is displayed in Figure 1-2.

### 1.4 Factors limiting analyzing power measurements

It is reasonable to ask why our measurements did not include $A_y$ and $A_{xz}$ angular distributions. To minimize errors, the vector analyzing power measurement requires a beam prepared with a large vector polarization, $P_z$. The beginning of this project coincided with the installation and commissioning of the atomic beam polarized

ion source at TUNL. At that time, the transition units on the source (see section 2.1) were not producing deuteron beams with large vector polarizations, making vector analyzing power measurements impractical. Very recent modifications to the transition units have remedied this situation.

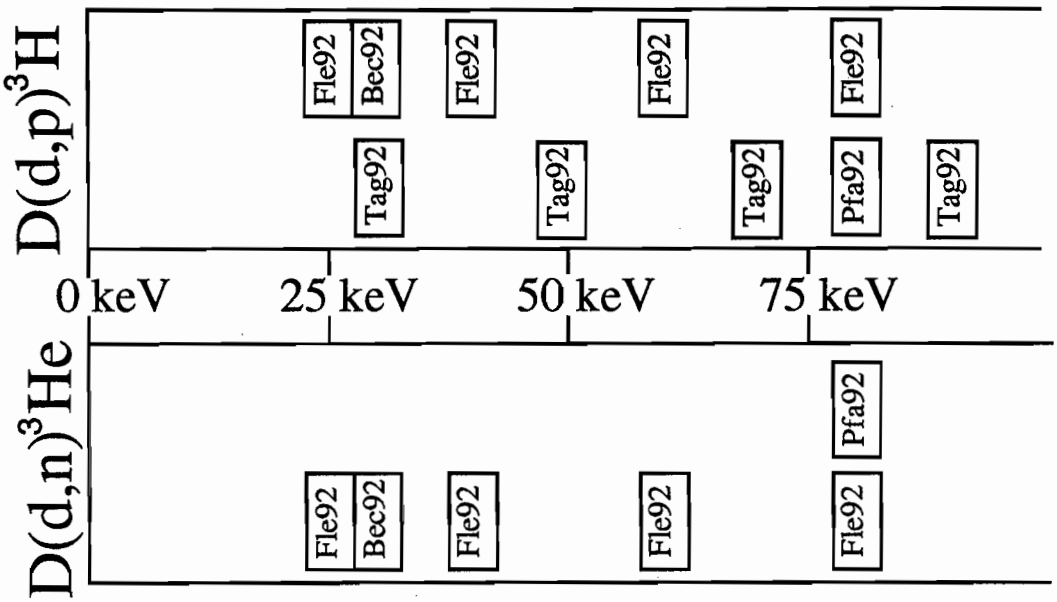


Figure 1-2. Energies at which analyzing powers have been measured for $D(d,p)^3H$ and $D(d,n)^3He$. The codes correspond to the references for each work, with the exception that [Fle92] indicates this thesis.

The measurement of $A_{xz}$ in our scheme is especially sensitive to spin axis misalignment errors ($\Delta\beta$,$\Delta\phi$), as described in section 4.4. Our Wien filter calibration was performed with protons at high energies (in the 52° chamber, following the tandem accelerator) and the proper settings for low energies were calculated from this calibration. Because this investigation was our first encounter with many of the problems inherent in precise, low energy analyzing power measurements with a new type of ion source, we decided not to try to measure a quantity that is so sensitive to the Wien filter calibration. It would be wise to repeat the calibration before any low-energy $A_{xz}$ measurements are attempted.

# II. Development - deuterium beams and deuterated targets: Deuteronomy

To study analyzing powers for the D-D reactions, one must have a source of polarized deuterium beam and targets which contain deuterium atoms. Source development has been carried out by the talented ABPIS personnel at TUNL, and a considerable amount of the author's time was spent on target development. This chapter, then, is a medieval tale of sorcery and targetry.

## 2.1 Characteristics of the TUNL Atomic Beam Polarized Ion Source

The Atomic Beam Polarized Ion Source (ABPIS), developed at TUNL [Cle93, Cro93, Din93], produces intense polarized beams of hydrogen or deuterium. By exchanging power supply modules and moving ground and power cables, one can switch from negatively-charged to positively-charged beams in several minutes. For our low-energy work, positive beams were used. The source regularly produces ~30 μA of positive beam, as measured immediately after the inflection magnet (see figure 2-4 in section 2.2.1, below). For reasons that are not quite clear, but are related to the emittance of the ABPIS beam and the optics of the Low Energy Beam Facility (LEBF), we routinely achieve only a few microamperes of beam in the LEBF chamber. This is acceptable for this project, however, because more intense beams would exacerbate our target degradation problems (described in section 2.3.3 ).

### 2.1.1 Theory of source operation

The production of a polarized deuterium beam in the ABPIS (figure 2-1) follows several steps. First, a beam of atoms is produced in the dissociator, where gas molecules are dissociated into neutral atoms. Molecular deuterium from a gas bottle is admitted at 30 cc / minute into a small bore tube in the dissociator. The deuterium passes through a radio frequency field region where the molecular bonds are broken, and the atoms decelerate as they transverse the copper cold nozzle, or accomodator, which is maintained at a temperature of 30 K. The average speed of the beam at this point, as measured for sources similar to ours, is around 800 m/s [Tho92].

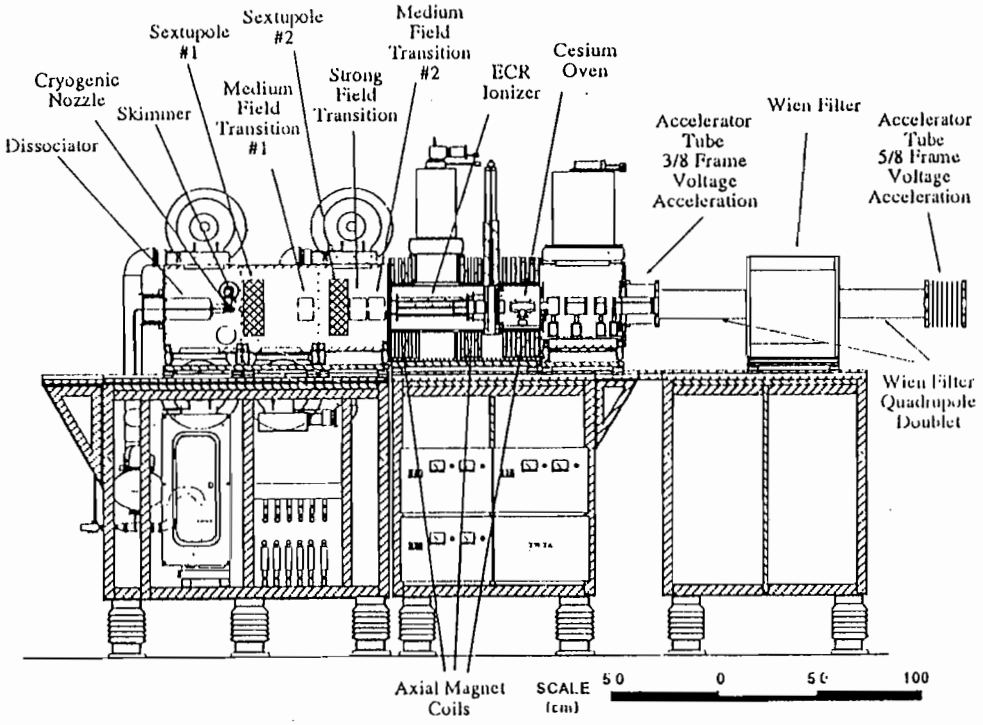


Figure 2-1. TUNL atomic beam polarized ion source. Starting in the left-most chamber, the atoms are dissociated from molecules, polarized by the transition units, and ionized in an ECR plasma before they are accelerated and enter the Wien filter.

The unpolarized, neutral atomic beam then passes through the first sextupole magnet. In the presence of a magnetic field, the hyperfine states of the deuterium atom separate in energy as indicated in the Breit-Rabi diagram in figure 2-2. For an unpolarized beam, all the nuclear substates are equally populated, as are the two atomic substates. Therefore, half of the atoms have electron spins pointing along the magnetic field direction and half the electron spins are antiparallel to this axis. The radial component of the magnetic field of a sextupole magnet is proportional to the square of the perpendicular distance from the axis. An atom with magnetic moment $\vec{\mu}$ in any magnetic environment possesses potential energy equal to the negative of the inner product of $\vec{\mu}$ and $\vec{B}$, and the associated force on the atom is equal to the negative of the gradient of the potential energy. An atom in a sextupole magnet, therefore, experiences a force in the radial direction which is proportional to the distance of the atom from the magnetic axis and proportional to the magnitude and sign of the magnetic moment projection of the atom onto this axis.

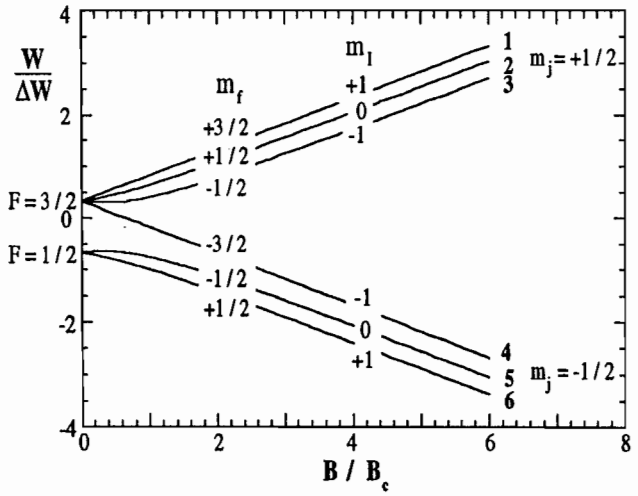


Figure 2-2. Breit-Rabi plot of the energy levels in a deuterium atom as a function of local magnetic field. On the vertical axis the energy is plotted in frequency units of $\Delta W = 327.4$ MHz. The magnetic field is plotted in units of $B_C = 117$ G for deuterium.

Atoms which are travelling along the magnetic axis experience no radial force and pass through the magnet undeflected. Because of the sign on the electron charge, the direction of the atomic magnetic moment is opposite to the electron spin direction. Those atoms with electron spins pointing along the magnetic field (the upper three substates in figure 2-2), have "negative" magnetic-moment projections and if they are off-axis, they experience a radial force which pulls them in towards the axis. However, atoms with electron spins opposite to the magnetic field (the lower three substates in figure 2-2) have "positive" magnetic-moment projections. Such atoms which are off-axis experience a radial force outwards which increases as they are pushed away from the beam axis, are lost from the beam, and are subsequently pumped away. A sextupole magnet, therefore, acts as a spatial filter to reject from the beam those atoms which are in the substates labelled 4, 5, and 6 in figure 2-2. Atoms are not transformed by a sextupole magnet; "spin-down" atoms are simply removed, and only atoms with atomic spin "up" remain in the atomically polarized beam.

The beam then passes through the first set of transition units, strong field 1 (SF1) and medium field 1 (MF1). These were not used in our early work, but during the 25 keV run, MF1 was employed. In the transition units, mutually orthogonal magnetic and radio frequency fields are produced. If the parameters are correctly set, atoms in the beam will undergo transitions between certain nuclear hyperfine states. For example, in our use of the MF1, we effectively produced transitions which change atoms in state 1 to state 4 (both the electron and nuclear spins are "flipped"), and vice versa. Since the first sextupole eliminated atoms in the lower three states, the beam enters MF1 with states 1, 2, and 3 equally populated and exits with atoms in states 2, 3, and 4. The beam traverses a second sextupole before passing through the strong field 2 (SF2) and medium field 2 (MF2) transition units. Continuing our example above, the beam which enters the second sextupole with atoms in states 2, 3, and 4 leaves the sextupole with state 4 atoms removed. This reduces the beam intensity by

one-third. The beam travels through SF2, where, in our example, transitions between atoms in states 3 and 5 occur. Since there are no atoms in state 5 to populate state 3, the beam leaves SF2 with atoms in states 2 and 5 and progresses through MF2 (which is turned off) unchanged. The tensor polarization component $P_{zz}$ is given by

$$P_{zz} = 1 - 3N_0 \tag{2.1}$$

where $N_0$ is the fraction of atoms with $m_I = 0$. In the above example all the atoms are in states 2 and 5, with $m_I = 0$, and the maximum possible $P_{zz}$ of this beam is -2. Of course, factors such as the efficiencies of the transition units and the sextupoles, plus the presence of the on-axis atoms which are not discarded by the sextupoles regardless of their spin state, conspire to reduce the magnitude of this optimal value for $P_{zz}$. After leaving the sextupole magnets and transition units, the beam is now a nuclear polarized atomic beam.

The atoms of the beam are next transformed into positive ions in the electron cyclotron resonance (ECR) plasma ionizer. The plasma is confined by the three solenoidal magnets, which also establish the spin axis along the beam. In the plasma, some atoms are stripped of one electron each and are accelerated by lenses 1 through 4 into the cesium oven region. The cesium oven, which was not used for these investigations, transforms positively charged ions into negatively charged ions for injection into the tandem Van de Graaff or the minitandem accelerators. After leaving the cesium oven, the polarized ion beam is accelerated to 3/8 of its final energy and enters the Wien filter which has perpendicular magnetic and electric fields to rotate the spins of the beam to whatever orientation is desired. Finally, the beam is accelerated to the selected energy and focussed through several lenses into the inflection magnet.

### 2.1.2 Transitions and polarizations used in this work

There were two modes of source operation used in this work, and the cartoon below (figure 2-3) summarizes the transitions and polarizations which were used in the

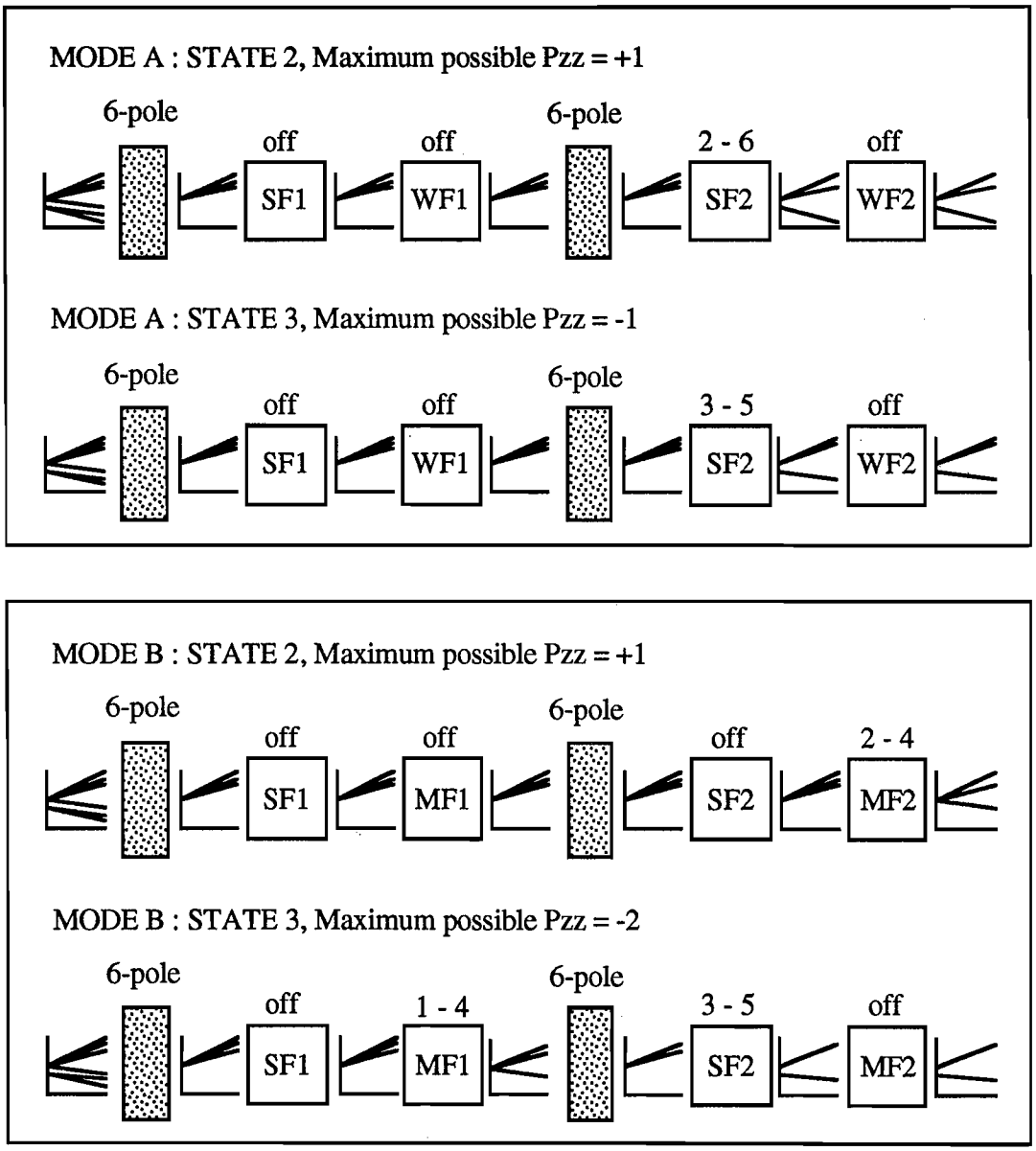


Figure 2-3. Schematic of the polarization states used in this work and how they were created in the TUNL atomic beam polarized ion source. Mode A involved changing the magnetic field in SF2 to obtain maximally positive and negative tensor polarizations. In mode B, the rf fields in SF2 and MF2 were switched on and off.

data collection. For both modes, the beam was switched through three states, with state 1 being unpolarized, state 2 with $P_{zz} > 0$, and state 3 with $P_{zz} < 0$. The medium-field transition units were not installed on the ABPIS for the 80, 60, and 40 keV runs. So, to obtain beams of maximally positive and maximally negative tensor polarizations for these runs, the magnetic field strength in the SF2 cavity was varied between two values, making $2 \leftrightarrow 6$ (state 2) and $3 \leftrightarrow 5$ (state 3) transitions to produce maximum tensor polarizations of +1 and -1 respectively. This was mode A. After the introduction of the medium field units, MF2 was used alone to provide $P_{zz} = +1$ for state 2, and MF1 and SF2 were used in combination for state 3 with $P_{zz} = -2$. This was mode B.

In both modes, the states were switched automatically by the data collection computer. States were switched about once per minute for mode A, and once every several hundred milliseconds for mode B. Faster state switching was impractical for mode A, because the magnetic field strength of SF2 had to be varied, and there was time lag involved in this process. In mode B state switching was accomplished by turning on and off the rf power supplies of the various transition units.

## 2.2 The Low Energy Beam Facility at TUNL

Titling this subsection "The Low Energy Beam Facility at TUNL" implies that that : (a) such a thing exists (it does), and (b) that it has a definite, physical form. It is this latter assumption which is troublesome, because, while the Low Energy Beam Facility (LEBF) does indeed have a form at any given instant, it is constantly changing in time, like the waves off the Carolina shore. During the 16 months over which the data were collected, slits, lenses, drift spaces, beamstops, acceleration tubes, and a minitandem were inserted, removed, or rearranged on this beamline. The aforementioned minitandem [Bla92] was not used in this work. Basically, however,

the various incarnations of the beamline can be divided into two major periods: before and after the insertion of the minitandem accelerator.

### 2.2.1 Beam transport system

The general location of LEBF with respect to the rest of the laboratory is shown in figure 2-4. The Atomic Beam Polarized Ion Source (ABPIS) injects polarized beam into an analyzing magnet which can be operated at either polarity to bend positive or negative beams to the right or left as needed. The beamline leading to the TUNL tandem Van de Graaff accelerator is thirty degrees to the left of the ABPIS line, and the

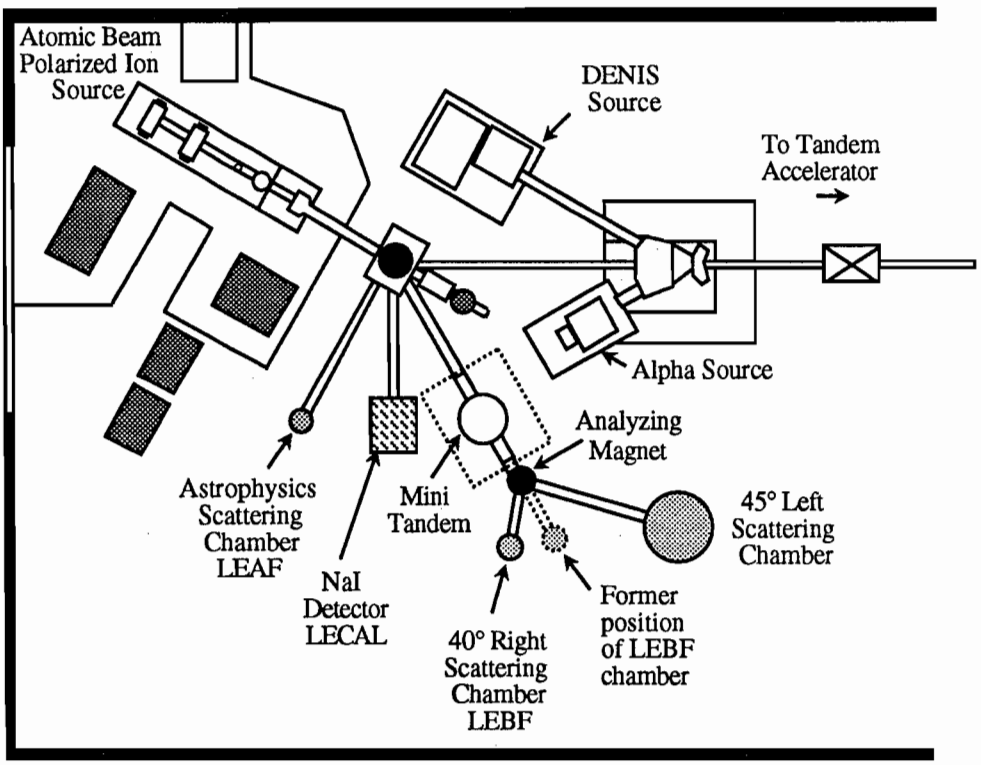


Figure 2-4. The low energy bay at TUNL. Beam created in the atomic beam polarized ion source is switched via a bending magnet into one of several low energy stations or sent to the tandem Van de Graaff accelerator for high energy experiments. For all our work, the LEBF chamber was located at the 0° port of the analyzing magnet, identified in the figure as the former position.

entrance to LEBF is 30° to the right.

The initial manifestation of LEBF is displayed schematically in figure 2-5. The entering beam passed through horizontal entrance slits; the operator used these to establish the proper magnetic field by adjusting the magnet current to balance the beam current on the left and right slits. The beam was focussed by an electrostatic quadrupole triplet lens and then steered by horizontal and vertical coil steerers. These steerers were controlled through a feedback system which adjusts current in the horizontal (vertical) steerer to minimize the difference in the beam deposited on the left-right (up-down) slits downstream. Following these slit-controlled steerers was the LEBF1 beamstop, an electron-suppressed, air-activated cup used to determine the beam current at this point. After a drift space, the beam passed through the slits used for the feedback system mentioned above and through the second set of slit-controlled steerers. The next element was the wire scanner. In this device, a bent wire rotates quickly, intercepting the beam horizontally and vertically and sending a signal to an oscilloscope, where the horizontal and vertical profiles of the beam are displayed. The LEBF2 beamstop was positioned after the scanner, and the second feedback slits were mounted before the entrance to the chamber. The second slit-controlled steerers were originally controlled by the slits preceding the chamber and later by "snout slits" in the chamber itself. Early on, a second electrostatic quadrupole triplet lens was installed ahead of the scanner, thereby improving the transmission of the beam into the chamber.

The later version of the LEBF beamline, displayed in figure 2-5 differs from the earlier one primarily by the insertion of the minitandem accelerator, designed by T.C. Black [Bla92], and built by our instrument makers. For the purposes of this thesis, the accelerator was grounded, in effect producing a long drift space. A bending magnet was also added to the beamline, following the minitandem, to permit separation of the various charge states produced in the minitandem stripper foil. This device was degaussed and turned off for our measurements.

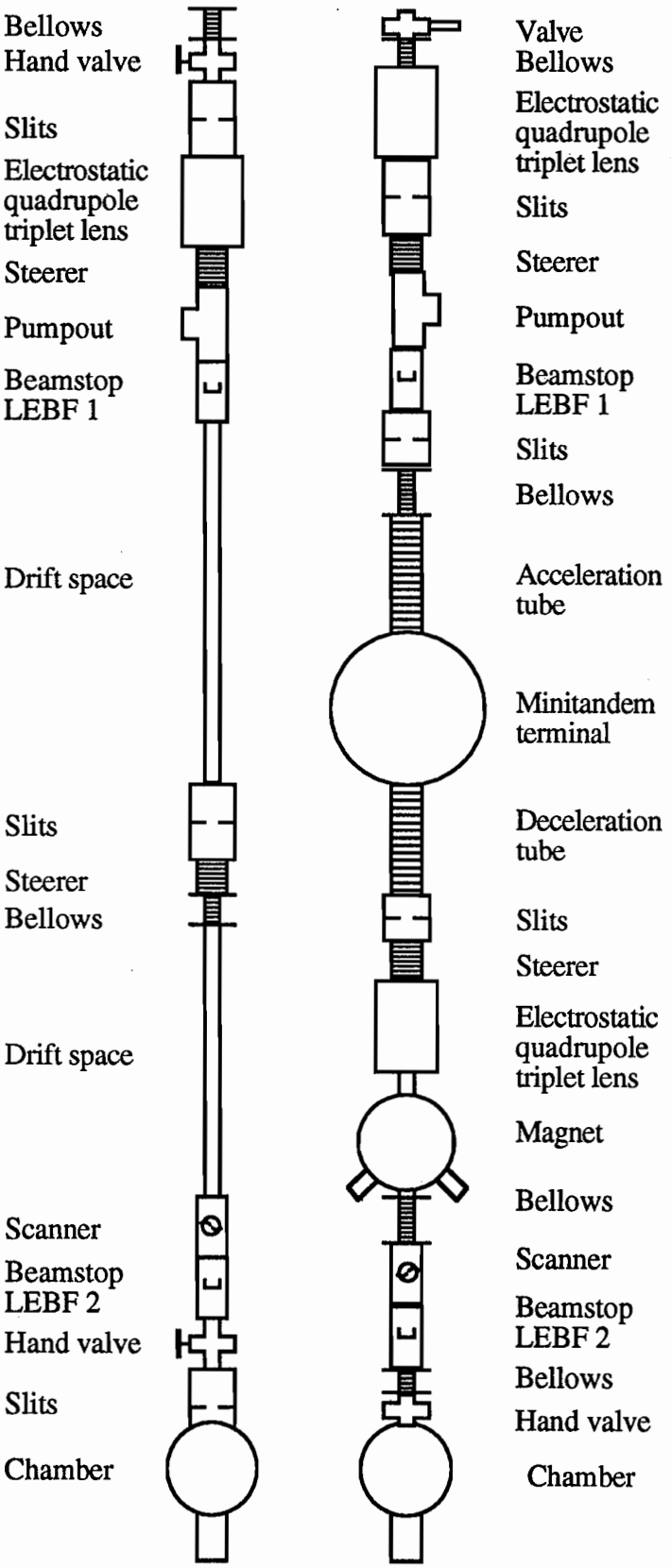


Figure 2-5. The low energy beam facility (LEBF) at two points in time. The version on the left is before the mintandem accelerator was installed, and the version on the right is after installation. The minitandem was not used for this work.

The vacuum system for LEBF consists of a diffusion pump near the entrance to the beamline with the pumpout located before the LEBF1 beamstop. The diffusion pump is equipped with a water-cooled baffle to minimize oil contamination in the vacuum, and a thermocouple gauge and high vacuum gauge are mounted on the pumpout. At the opposite end, a Balzers Turbopump is used to evacuate the chamber, and thermocouple and high vacuum gauges are mounted on the chamber.

### 2.2.2 LEBF scattering chamber and polarimeter

The LEBF scattering chamber was designed by the author and built by the Duke Instrument Shop with some components fabricated at the UNC Shop. The major components of the chamber are constructed of aluminum. The chamber was designed to be used as part of a planned gas jet target system, which we were unable to acquire. This expected use dictated many of the unusual features of the chamber, notably its size and the rotating detector plate mechanism in the lid. A cross sectional view of the chamber is given in figure 2-6.

The inside of the chamber is 15.24 cm in height, and there are 10.16-cm entrance and exit ports, as well as two viewing ports, in the side. The viewing port on the right side (with respect to the beam direction) is at right angles to the beam axis, and the left side window is at 30°. There is also a blank-off flange with a high vacuum gauge at 135° on the left. The inner diameter of the chamber is 30.48 cm. The main novelty of the chamber is its lid, which features two nested collars which can be independently rotated from the outside, without breaking vacuum. Inside, detector mounting plates are attached to the collars — the right detector plate on the inner collar and the left plate on the outer collar. The original detector plates each supported three detector holders, but new plates, specially designed for the 25 keV run, were constructed to hold four detector holders each. On the old and new plates, the detectors were spaced 15° apart. Detector holders which attach to these plates hold the solid state

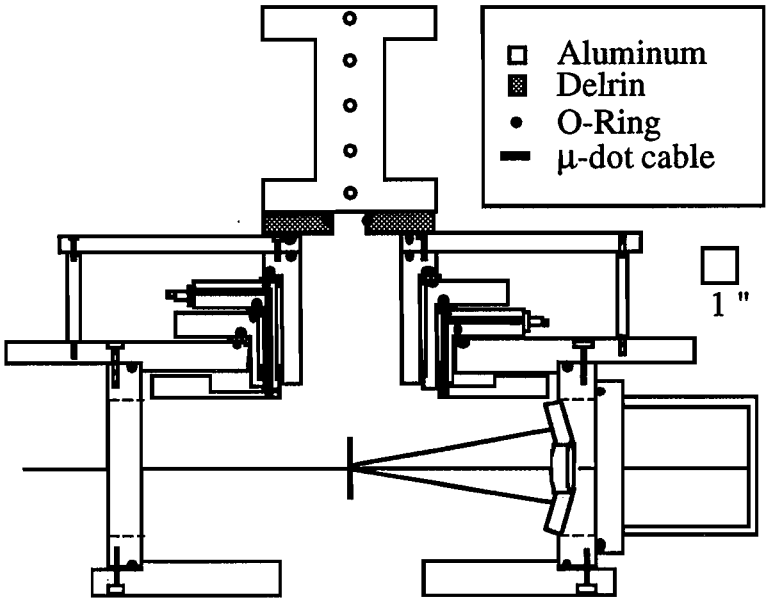


Figure 2-6. The LEBF scattering chamber. Beam enters from the left, interacts with the target in the center, and particles which scatter at 10° are detected in the polarimeter. The chamber detectors (not shown) attach to the rotating plates in the chamber lid.

detectors, with snouts in front for collimator slits. Small magnets on the snouts prevent scattered electrons from striking the detector surface, and thick carbon foils mounted on the front slits stop elastically scattered deuterons. Microdot cables which carry the detector signals to the outside pass through feedthrus in the nested collars, so that the cables move with the detectors, and are not stressed or pulled when the detectors are rotated. The centers of the detectors are 7.62 cm from the bottom of the chamber, in the plane of the target. A target rod which is interchangeable with those used in the TUNL 52° chamber is inserted through the lid in a Delrin flange with an o-ring seal. A snout which supports anti-electron-scattering slits is mounted on the entrance port and insulated from the chamber. Originally designed for use in the TUNL high resolution chamber, these slits define the size of the beamspot on the target and are used in feedback-control of steerers.

The beam polarization monitor (or polarimeter) is mounted on the exit port of the chamber, and is displayed in figure 2-7. This device consists of four solid state detectors, two in the horizontal plane and two in the vertical plane. The detectors are held in an aluminum plate by set screws, pointing at 10° with respect to the beam axis toward the center of the chamber. The target for the analyzing power measurements also serves as the polarimeter target. Anti-electron scattering collimator snouts, like

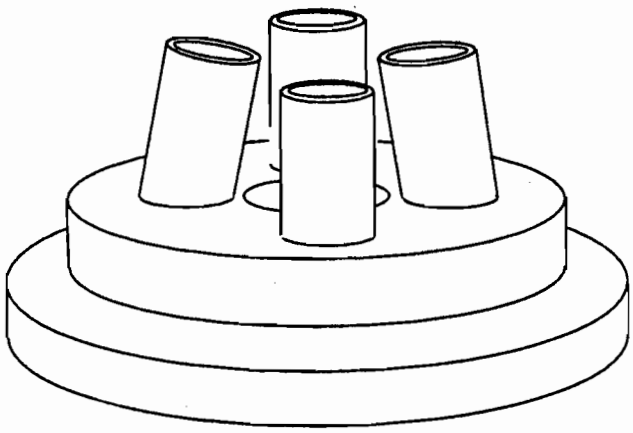

Figure 2-7. The polarimeter. Four solid-state detectors are mounted at 10° with respect to the beam, two in the horizontal plane and two in the vertical plane (Figure 1b in [Fle92]).

those described above for the chamber detectors, are attached in front of the detectors. Elastically scattered deuterons are stopped in 0.1 mil thick aluminized Mylar foils in front of the detectors. The collimator slits, along with the holes machined in the aluminum plate, establish the 10° lines. There is also a set of holes drilled through the aluminum plate to aid pumping, and a larger hole in the center of the plate, through which the unscattered beam passes. A 10.15-cm diameter beampipe with electrical feedthrus for the polarimeter signals attaches to the back of the polarimeter plate. A

mechanical gauge, a thermocouple gauge, and a roughing vacuum pumpout are also mounted on this piece.

### 2.2.3 Beam current integration

Absolute beam current integration, which is essential for cross section measurements, is not necessary for tensor analyzing power measurements. However, relative integration from polarization state to state *is* important. In other words, the integration need not be absolute, but should not vary as the polarization states change in the course of the measurement. Nevertheless, we have endeavored to provide accurate absolute integration at the LEBF chamber. Other researchers, who measured cross sections [Kra87, Bro90], have approached this problem by using a calorimeter. This device measures the power dissipated when the beam stops in it, and the beam energy is used to infer the intensity.

We elected to collect all of the charge deposited by the beam on the chamber and target. The chamber was isolated from the pumping stand by a large Delrin spacer, and from the beamline and slit snout by a smaller Delrin flange. Delrin covers insulated all the detectors from the detector holders (which were electrically connected to the chamber) and the electrical feedthrus were also electrically insulated. When the thermocouple and high vacuum gauges were disconnected, the chamber was truly isolated from ground. To integrate the beam, one cable was attached to the chamber and another to the target rod. The currents through the two were summed and inputted to the Brookhaven Instrument Corp. beam current integrator in the control room, which produced the beam current integration signal sent to the computer. We found that copious numbers of electrons are produced when the beam passes through the target at these energies, and the target rod was positively biased to attract these electrons back to the rod by connecting the target rod to the positive terminal of a 90 V battery and connecting the negative terminal to the integrator. The charge division between the

chamber and target was determined by disconnecting either input to the integrator. Tests were conducted comparing results for targets in place with results for empty target rings, as well as with other variations. Our studies showed that this arrangement provided a reliable, consistent determination of the relative beam intensity, as needed for this work.

### 2.3.1 Target requirements

In selecting an appropriate target material for a given experiment, there are several general requirements which must be considered. The target must contain a sufficient quantity of the desired target isotope to provide a reasonable count rate with the expected beam current. The target material must be free of contaminants which would produce peaks that interfere with the peaks of interest in the spectra. The density of the desired target nuclei in the target material should remain constant under bombardment of the beam, or, failing that, the depletion of the target must be slow enough that it does not affect the results of the experiment. The target should be relatively easy to manufacture or purchase and not pose a health risk to those who will handle it.

The targets used in this work were subject to additional restrictions because they were used in very low energy experiments. First, the overall energy loss of the incident deuteron beam had to be small enough that the reaction energy could be determined in a reasonable way to within a few keV. Furthermore, the target had to be thin enough to permit the $^3$He recoils to escape and be detected.

The low-energy nature of our work prohibited the use of a conventional deuterium gas cell for this investigation. Any foil which might have been used to confine the gas would have stopped the incident deuterons, preventing reactions from occurring. A differentially-pumped gas jet target was considered for these experiments, and such a gas jet target was used for cross section measurements for D(d,p)$^3$H and

$D(d,n)^3He$ in our energy range [Kra87]. When we were unable to borrow a supersonic gas jet target, however, we decided that designing and building such a device from scratch was too large a technical problem to undertake at the time. The target deuterium, therefore, had to be dissolved or contained within a solid medium, and in order that energy losses be small, that medium had to be in the form of a thin film.

Other researchers had indicated that deuterated polyethylene was a poor choice, because of rapid depletion of deuterium from the bombarded polymer [Sch87], and our own investigations agreed with this conclusion (see section 2.3.3). Our initial experience with deuterated parapolyphenyl, $(C_6D_4)_n$, or DPP, [Iri73] was disheartening. We had obtained some DPP targets mounted on rings and some deposited on slides from the University of Giessen group, who had used them successfully in their work [Pfa85], but we found that the targets broke easily under bombardment, were extremely fragile, and were difficult to float off the glass slides. Clearly DPP targets could only be used for data collection if a suitably large supply was available, and this was not the case. Therefore, we developed the method for preparing thin film deuterated titanium (TiD) targets. The TiD targets were used for all of the data collected at bombarding energies of 80, 60, and 40 keV. When we were ready to collect the 25-keV data, we returned to the DPP targets, having obtained a sufficient quantity of DPP from Y. Tagishi of the University of Tsukuba, Japan. The higher concentration of deuterium in these DPP targets made it possible for us to collect high precision data at this energy, where the cross section is very small (~0.02 mb/sr).

It is customary in nuclear physics to use "target thickness" to indicate the amount of material in a target. The target thickness is the product of the density and the physical thickness of the target. The areal density can be expressed as a mass density or an atomic density, so that the units of the target thickness can be in $\mu g/cm^2$ or $atoms/cm^2$. For example, the density of carbon is 2.0 $g/cm^3$, so a carbon film that is $10^{-6}$ cm thick corresponds to a target thickness of 2.0 $\mu g/cm^2$ of carbon.

### 2.3.2 Target fabrication

All of the thin film targets used in this work were deposited at the UNC nuclear group's thin film deposition station. The vacuum system for this facility includes a roughing pump with a molecular sieve trap which is used to evacuate the bell jar to about 50 mT, and a CTI Cryogenics Cryo-Torr 8 High Vacuum Cryopump and model 8300 helium compressor which can evacuate the system to base pressures in the $10^{-7}$ Torr range. The pressure is measured by an ionization gauge, and film thicknesses are determined using a Sloan rate-deposition monitor. This facility can be used for sputter, electron gun, or resistive heating deposition.

Both types of deuterated targets were deposited onto thin film carbon substrates, purchased from the Arizona Carbon Foils Company. A substrate was necessary because the target films themselves were too thin to be self-supporting. For both the TiD and DPP targets, the target films were deposited onto carbon foils that had already been floated and mounted onto rings. We tried depositing titanium onto carbon foils mounted on glass slides and then floating afterwards, but the extreme conditions obtained during the electron gun deposition apparently sublimed the salt layers from the slides, making the foils impossible to float off. The thickness of the carbon film on each slide is provided by the manufacturer, and 5, 10, and 20 $\mu g/cm^2$ films were used as target substrates, with 10 $\mu g/cm^2$ being the most prevalent.

#### 2.3.2.1 Deuterated titanium targets

The TiD targets were produced by depositing the titanium film and then heating it in a deuterium atmosphere so that deuterium gas was absorbed into the titanium. Titanium is a well-known "getter" for gases. Fabricating a batch of TiD targets was accomplished in three steps. First, the carbon films were mounted onto target rings as described above. The target rings have identifying marks, and the ring identification

and thickness of the carbon layer were recorded. Second, the rings were mounted in the bell jar on the bottom plate of a copper oven used to heat them in step three. The configuration of the equipment in the bell jar for TiD target fabrication is shown schematically in figure 2-8. A pellet of titanium (natural abundance) was placed in the water-cooled copper crucible and the system was evacuated to base vacuum. After confirming that the system was properly grounded, the electron gun was then preheated, as per the manufacturer's instructions, and the electron gun power was increased to the desired value, which was ultimately chosen to be 0.3 W at 11 kV. Deposition of the titanium layer was monitored using the rate deposition meter, and the electron gun was turned off once the appropriate thickness was obtained. In step three, the temperature of the oven was increased at a pace slow enough to prevent significant film breakage. This temperature was determined by a chromel-alumel thermocouple imbedded in the copper oven. Once the oven temperature exceeded 400° C, the chamber was isolated from the cryopump and deuterium gas was admitted into the chamber to a pressure of 30 mT, and the power of the oven was adjusted so that the equilibrium temperature was about 400° C. The system was then allowed to sit for several hours before the oven power was slowly lowered and the targets returned to room temperature. The deuterium gas was then pumped away, the system backfilled with argon, and the targets recovered.

Prior to the construction of the copper oven, the deuteration phase was accomplished using a slightly different setup. Rather than placing an oven in a vacuum system, we placed a vacuum system inside an oven. We had obtained a cylindrical oven which operated in atmosphere, creating an approximately 8 cm heated region. A quartz glass tube of about 3.81 cm diameter was inserted inside the cylindrical cavity of the oven so that the two ends of the tube extended outside the oven by about 30.5 cm. Aluminum vacuum flanges with o-rings were pushed into the ends of the tube, and the system was connected to the bell jar at one end so that it could be

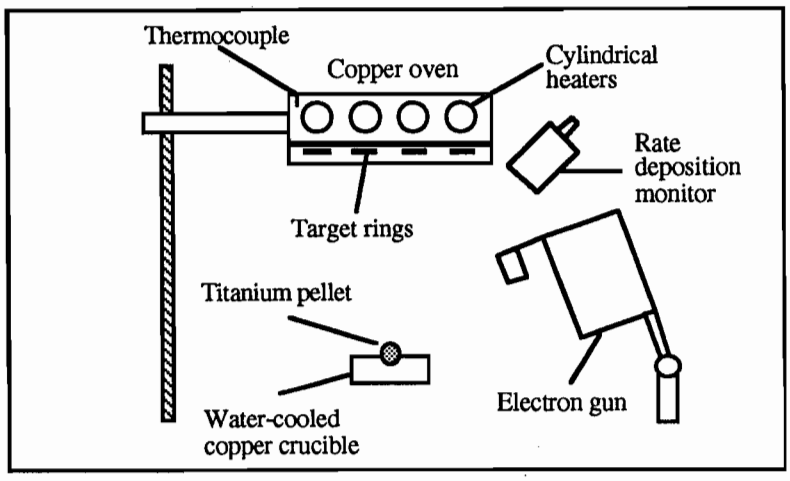


Figure 2-8. The set-up for evaporation of titanium thin films inside an evacuated bell jar.

evacuated with the cryopump. Vacuum gauges and electrical feedthrus were mounted on the flange of the opposite end. Using this system, titanium films were deposited by the electron gun in the bell jar, removed, and heated in a stainless steel target holder which was placed into the glass tube to the center of the oven. This system was judged inferior because of the difficulty in obtaining high vacuum base pressures in the tube, the necessity of moving the films between deposition and deuteration, the limited number of targets which could be deuterated in the small heated region of the oven, and the fragility of the thin-walled tube itself, which cracked on several occasions.

We varied the temperatures and pressures of the deuteration, but the optimal values listed above closely follow the results of McQuillan [McQ50]. This excellent paper treats deuterium in titanium as a thermodynamic system, and the temperature and pressure values above maximize the deuterium content without using an unacceptably large amount of deuterium gas. References [Gal72], [Gal85], and [Gal87] also describe the experience of other researchers with deuterated titanium. In general, the concentration of deuterium in the titanium films we produced was smaller than the values given in [McQ50], where bulk samples of titanium were used. We hypothesize

that diffusion of deuterium in titanium is inhibited by the amorphous nature of the film as compared to the crystalline structure of a bulk sample. After experience with these targets indicated that deuterium was probably concentrated in the front surface of the titanium, we developed a layering technique of depositing a thinner layer of titanium, deuterating, and repeating these steps until the desired thickness was obtained. These targets were referred to as "Dagwood" targets, because the construction was similar to Dagwood sandwiches from the "Blondie" comic strip. A summary of the characteristics of the targets used in the measurements is provided in section 2.3.4, below.

#### 2.3.2.2 Deuterated parapolyphenyl targets

Chemically produced deuterated parapolyphenyl was obtained in powder form from Dr. Y. Tagishi at Tsukuba, Japan, who used such targets in his own work [Tag92]. The synthesis of this compound and its use as a target for nuclear physics experiments has been described by Irie [Iri73]. To produce useful targets from this fine, light brown powder, a measured mass of DPP was loaded into a standard resistive evaporation boat in the bell jar, configured as in figure 2-9. In order to prevent the light-weight powder from blowing out of the boat during pump-down, a few drops of alcohol were placed on it. After floating carbon onto rings and loading them onto the target ring mount, the system was evacuated to base pressure. The current through the boat was slowly increased while the vacuum pressure and the rate deposition meter were monitored. Once deposition began, the pressure in the chamber would increase and the deposition monitor would register the increasing film thickness. After a minute or so at a given current the deposition would cease, and the current would have to be increased. This is presumably due to the fact that the DPP in contact with the boat would "burn", leaving a black, ashy residue that insulated the upper DPP layers from the heat of the boat. Increasing the power dissipated by the boat permitted the upper

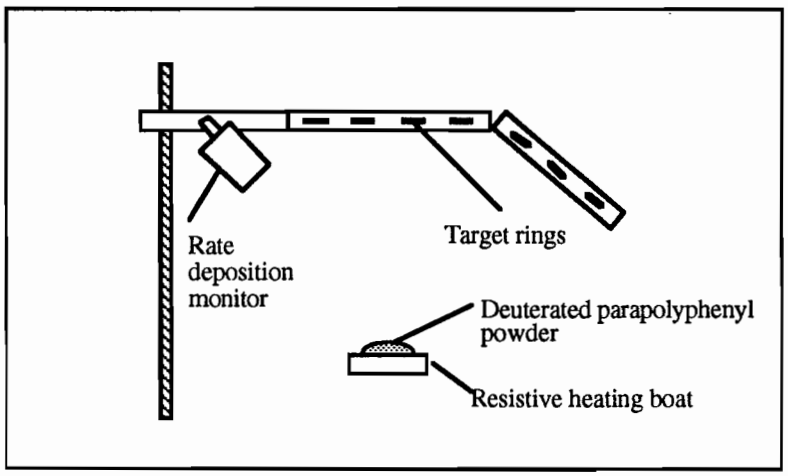


Figure 2-9. The set-up for evaporation of deuterated parapolyphenyl thin films inside an evacuated bell jar.

layers of DPP to evaporate. Once the desired film thickness, as measured by the rate deposition monitor, had been obtained, the current through the boat was turned off and the system was allowed to cool before the targets were removed. The deposition process took roughly 20 minutes to complete.

In general, the DPP targets are far easier and faster to produce than the TiD targets. The process of heating and cooling the titanium films requires eight to twelve hours of constant supervision, and the use of explosive deuterium gas demands careful handling. Also, resistive deposition is much simpler than electron gun deposition, which produces very high temperatures inside the bell jar and requires high electric fields (corresponding to 11 kV). These violent conditions indicate that electron beam deposition should be attempted with care, and the materials used inside the vacuum system be thoughtfully chosen.

### 2.3.3 Target thickness measurements

Both the TiD and DPP targets exhibited depletion of deuterium under bombardment by intense, low energy beams. The stopping power — the energy loss

for a beam of a given energy through a certain thickness of material — reaches its maximum value for most materials at energies within our range of study. The energy lost by the beam is deposited in the target as heat, causing deuterium to evaporate from the target. In figure 2-10 this is illustrated for the TiD and DPP targets used in this work, as well as for $CD_2$ targets which were also investigated. The $CD_2$ targets were evaporated from solid flakes of polyethylene using the resistive evaporation procedure described above. The TiD targets were examined with a 2 μA beam. For the polymer samples, the initial target thickness was determined using a 30 nA beam, then the beam intensity was raised to 1.6 μA for the depletion measurements. All measurements were made with 80-keV deuterons.

The DPP and $CD_2$ batches were both fabricated to have total target thicknesses of 20 $\mu g/cm^2$, and, taking into account their chemical formulae, we expected the $CD_2$ targets to have 2.2 times more deuterium than the DPP targets. Experimentally, based on this small sample size, we saw that there was 1.9 times more deuterium in the $CD_2$ targets than in the DPP targets. The TiD concentration remained reasonably steady, although it was lower than that of the polymers. However, the initially high deuterium concentration for the $CD_2$ targets deteriorated to almost that of the TiD targets within the first few minutes, as shown in figure 2-10. The deuterium content of the DPP targets decreased initially, then reached a plateau. This figure illustrates the inferiority of the $CD_2$ targets and the advantages of the DPP targets.

Because of the high Q-value for $D(d,p)^3H$ and $D(d,n)^3He$, and the high Coulomb barriers for any other reactions, the low-energy spectra for the TiD and the DPP targets simply consisted of the proton, triton and $^3$helium peaks from the fusion reactions and contained no information on titanium, carbon or other elements in the targets. However, the incident beam loses energy in passing through the target, and the primary energy loss mechanism is scattering from the electrons of the higher-Z elements. Therefore, to determine the reaction energy (the mean energy of the reactions

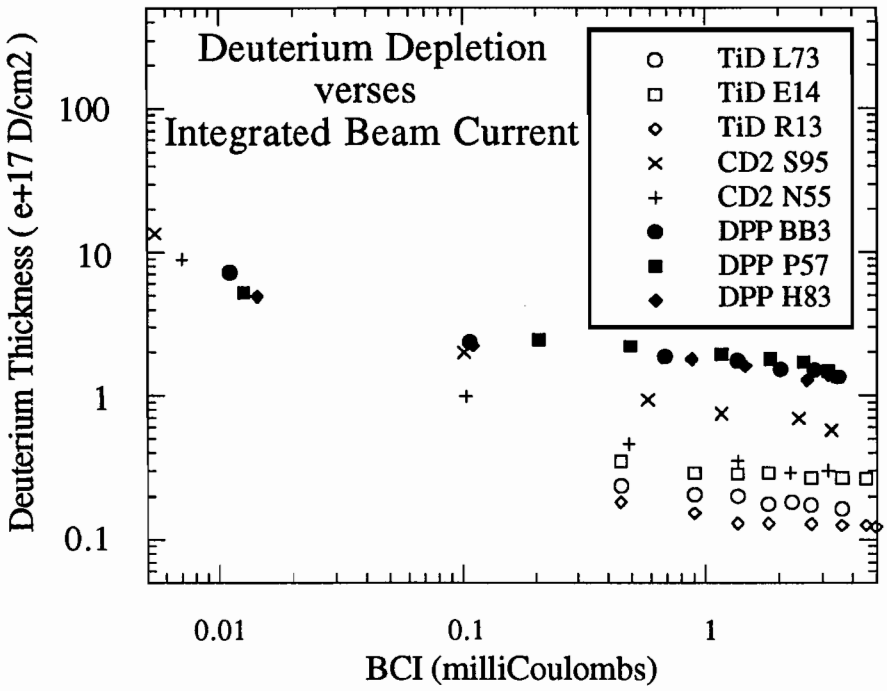


Figure 2-10. Comparison of the deuterium thicknesses determined from the $D(d,p)^3H$ yields from deuterated titanium and deuterated polymer targets. The horizonal axis is the total amount of beam incident upon the target.

which produced the detected particles), the major components of the targets had to be quantified. In general, this could not be done with low-energy beams, so high-energy beams were used.

Because of deuterium depletion and target breakage at low energies, dozens of targets were used in measuring a given tensor analyzing power at a given energy. It was unreasonable to measure the target thicknesses for every target used in the measurements, so thickness measurements were made for a sample of targets from each batch. The thicknesses were measured using tandem-accelerated deuteron beams in the 52° chamber at TUNL. Thicknesses were determined from deuteron elastic scattering yields. The cross sections for D(d,d)D at 6.0 and 12.0 MeV were taken from [Wil69]; Rutherford scattering was assumed for the $^{48}Ti(d,d)^{48}Ti$ cross sections, since use of

reasonable optical model parameters did not predict cross sections appreciably different from the Rutherford predictions. The Rutherford cross section formula was also used for oxygen, since the differences from the data of [Cor69] were small at the relevant energies and angles.

### 2.3.4 Summary of data on targets used in this work

Table-2.1 below summarizes the target thickness information for the target batches used in the tensor analyzing power measurements. Note that the layered "Dagwood" batches do not appear to have a higher concentration of deuterium than the single-layer targets. However, this table lists only results for batches used in the data collection, which have the highest amounts of deuterium. A smaller fraction of the layered batches were discarded for unacceptably low deuterium content, as compared with the single-layered batches. High-energy target thickness measurements were not made for the targets used for the 80-keV $A_{zz}$ data, the first tensor analyzing power collected. We expected to make such measurements after the data collection, but all of the targets from the 02/24/91 batch were used in obtaining the $A_{zz}$ data. However, thickness measurements were made on the 02/26/91 batch, which was made two days after the 02/24/91 batch. The final titanium film thickness, as indicated by the rate deposition monitor, was identical for the two cases. Therefore, the titanium and oxygen thicknesses indicated below for the 02/24/91 batch are those obtained for the 02/26/91 batch.

Table 2.1 does not indicate the errors on the target thicknesses, and the values given are composite values for one or more sample targets tested for the batch. The variation in thicknesses for the different targets in a given batch is presumed to be larger than the uncertainty on the measurement for a single target. This is because in the bell jar individual targets were positioned at varying distances and orientations with respect to the evaporation source. In the cases where more than two targets from a given batch

were sampled, the ratio of the standard deviation to the mean was not bigger than 15%. This observation is based on a small sample size, however. To err on the side of overestimating the uncertainty in the thicknesses, an overall uncertainty of 50% of the values in the table is estimated. The impact of this estimate is in discussed in section 4.1.1.

Table 2.1 Target thickness summary.

| Target | Batch | Layers | $E_d$ | $\times 10^{16}$ D/cm$^2$ | $\times 10^{16}$ O/cm$^2$ | $\times 10^{16}$ Ti/cm$^2$ |
|---|---|---|---|---|---|---|
| TiD | 02/24/91 | 1 | 80 keV | 3.4 | 41.6* | 15.5* |
| TiD | 06/22/91 | 1 | 6 MeV | 5.2 | 32.0 | 28.4 |
| TiD | 07/04/91 | 1 | 6 MeV | 1.1 | 13.7 | 9.8 |
| TiD | 07/25/91 | 1 | 6 MeV | 4.1 | 16.3 | 7.8 |
| TiD | 07/29/91 | 1 | 6 MeV | 5.6 | 12.6 | 5.4 |
| TiD | 10/10/91 | 7 | 6 MeV | 6.8 | 32.9 | 12.4 |
| TiD | 10/30/91 | 7 | 6 MeV | 6.1 | 36.5 | 14.2 |
| TiD | 11/01/91 | 5 | 6 MeV | 6.6 | 22.0 | 7.6 |
| TiD | 01/20/92 | 7 | 6 MeV | 4.4 | 14.5 | 6.5 |

| Target | Batch | Layers | $E_d$ | $\times 10^{16}$ D/cm$^2$ | | $\times 10^{16}$ C/cm$^2$ |
|---|---|---|---|---|---|---|
| DPP | 06/09/92 | 1 | 12 MeV | 85.6 | - | 156.5 |
| DPP | 06/25/92 | 1 | 12 MeV | 112.0 | - | 200.0 |

*The titanium and oxygen thickness obtained for the 02/26/91 batch, as discussed in the text.

## III. Experimentation: Lamentations

Much of the experimental design was dictated by the beam polarization states available from the source and by the decreasing deuterium content of the target. These factors were responsible for modifications of the data-collections schemes previously used in our group.

### 3.1. Analyzing power formalism

Because the source was newly commissioned when this work began, and because it fundamentally differs from the Lamb shift source previously used at TUNL, much effort went into developing an appropriate data collection scheme for use with the transitions available from the ABPIS. When data were taken using the Lamb shift source, certain assumptions were made regarding the polarizations of the beam in different states — assumptions which do not hold for beams produced in the ABPIS. Also, with the scheme of [Ton80] the target thickness was assumed to be constant over the course of a run. For our low energy work, the new scheme had to account for the deuterium depletion of the targets. We also did not need to produce a general data collection scheme that could also be used for vector analyzing power measurements.

With these thoughts in mind, an adaptation of the "three spin state method" discussed by Ohlsen and Keaton [Ohl73] was implemented. Data are collected in three states: an unpolarized state, a state with maximum-positive $P_{zz}$, and a state with maximum-negative $P_{zz}$. For purposes of notation, we label these states 1, 2, and 3, respectively, and use $P_{zz}^{(2)}$ to refer to the tensor polarization in state 2 and $P_{zz}^{(3)}$ to indicate the polarization for state 3. The counts collected in state 3 for the left detector (in the

Madison convention [Mad70] sense) are indicated by $L_3$. It is more instructive to deviate from the numerical labelling for state 1 and use $L_u$ rather that $L_1$ to emphasize that this is the unpolarized state.

In Appendix A we show (A.9) that for detectors labelled left, right, up, and down according to the Madison conventions, that is, for those placed at $\phi = 0°$, 180°, 270°, and 90°, the expressions for the number of counts in a polarized state p are given by

$$
\begin{aligned}
L_p &= I_L(\theta)\left\{1+\frac{3}{2}P_z^{(p)}A_y(\theta)\sin\beta+\frac{1}{2}P_{zz}^{(p)}\left[A_{yy}(\theta)\sin^2\beta+A_{zz}(\theta)\cos^2\beta\right]\right\} \\
R_p &= I_R(\theta)\left\{1-\frac{3}{2}P_z^{(p)}A_y(\theta)\sin\beta+\frac{1}{2}P_{zz}^{(p)}\left[A_{yy}(\theta)\sin^2\beta+A_{zz}(\theta)\cos^2\beta\right]\right\} \\
U_p &= I_U(\theta)\left\{1+P_{zz}^{(p)}A_{xz}(\theta)\sin\beta\cos\beta+\frac{1}{2}P_{zz}^{(p)}\left[A_{xx}(\theta)\sin^2\beta+A_{zz}(\theta)\cos^2\beta\right]\right\} \\
D_p &= I_D(\theta)\left\{1-P_{zz}^{(p)}A_{xz}(\theta)\sin\beta\cos\beta+\frac{1}{2}P_{zz}^{(p)}\left[A_{xx}(\theta)\sin^2\beta+A_{zz}(\theta)\cos^2\beta\right]\right\}
\end{aligned}
\tag{3.1}
$$

Recall that the $I_0(\theta)$ factors, which differ for each detector, include the number of incident beam particles, the target atom density, the detector efficiency and solid angle, and the unpolarized cross section. An $A_{zz}$ measurement requires that the spin axis of the beam be collinear with the incident momentum, that is, $\beta = 0°$. An $A_{yy}$ measurement, used to determine $(A_{xx}\text{-}A_{yy})$, requires that the spin axis of the beam be orthogonal to the incident momentum ($\beta = 90°$), and that the chamber detectors correspond to left and right detectors, as defined by the Madison convention. For chamber detectors in the horizontal plane, this means that the spin axis must be aligned vertically. The Wien filter must be set so that these conditions are met. We now consider the $A_{zz}$ and $A_{yy}$ cases individually.

*$\beta = 0°$, measuring $A_{zz}$*

In this case, with the spin axis parallel to the incident momentum direction, the equations describing the number of counts in the detectors are all identical. That is, there is no real distinction between left, right, up and down detectors. This holds for the detectors in the chamber as well as those in the polarimeter. For the "left" detector, for example,

$$L_p = I_L(\theta)\left\{1+\frac{1}{2}P_{zz}^{(p)}A_{zz}(\theta)\right\}. \tag{3.2}$$

If we assume that the $I_L(\theta)$ factor is the same for all states, we can eliminate the $I_L(\theta)$ factors by forming a ratio of the polarized and unpolarized counts, $\frac{L_p(\theta)}{I_L(\theta)}$; we denote such ratios by lower-case variable names.

$$l = r = u = d = \left\{1+\frac{1}{2}P_{zz}^{(p)}A_{zz}(\theta)\right\} \tag{3.3}$$

The polarization is determined by summing the four polarimeter monitor detector ratios,

$$S = l+r+u+d = \left\{4+2P_{zz}^{(p)}A_{zz}^{mon}\right\}, \tag{3.4}$$

so that,

$$\boxed{P_{zz}^{(p)} = \frac{S-4}{2A_{zz}^{mon}}}. \tag{3.5}$$

The polarization of state p is determined from the monitor counts in the polarized state p and the monitor counts in the unpolarized state.

For the left and right detectors in the chamber, however, all three states are used to calculate the analyzing power from the ratio R:

$$R = \frac{S_2}{S_3} = \frac{l_2 + r_2}{l_3 + r_3} = \frac{\left\{2 + P_{zz}^{(2)} A_{zz}(\theta)\right\}}{\left\{2 + P_{zz}^{(3)} A_{zz}(\theta)\right\}} \tag{3.6}$$

so that

$$\boxed{A_{zz}(\theta) = \frac{2(R-1)}{\left(P_{zz}^{(2)} - RP_{zz}^{(3)}\right)}} \tag{3.7}$$

*$\beta = 90°$, orthogonal to the reaction plane, measuring $A_{yy}$*

The game is now self-explanatory. If we insert $\beta = 90°$ in the expression for the detector counts and define the sum S and the ratio R as above, we get

$$\boxed{P_{zz}^{(p)} = \frac{4 - S}{A_{zz}^{mon}}} \tag{3.8}$$

$$\boxed{A_{yy}(\theta) = \frac{2(R-1)}{\left(P_{zz}^{(2)} - RP_{zz}^{(3)}\right)}}. \tag{3.9}$$

The error expressions for these values are discussed in chapter 4. From this formalism, it is evident that we must be able to prepare the beam in two tensor-polarized states and one unpolarized state. Since the ratio R may be close to unity, the denominator of the expression for the analyzing powers is such that the difference of the tensor polarizations for the two polarized states should be as large as possible. Such is the case when we use maximally positive and maximally negative $P_{zz}$ values for the two states.

### 3.2. Precise tensor analyzing power measurements

The angular distributions for $A_{zz}$ and $(A_{xx}-A_{yy})$ were measured at the TUNL Low Energy Beam Facility described in section 2.2. The polarized beam was produced by the atomic beam polarized ion source (see section 2.1).

### 3.2.1 Detectors

Surface barrier solid state detectors were mounted in the chamber and polarimeter, as described in section 2.2.2. Detectors with thicknesses of 300 microns and 100 microns were used. The 100-micron detectors do not completely stop the $D(d,p)^3H$ protons, but they were found to be less noisy and more reliable, and the energy loss of the protons in the detectors was more than sufficient for particle identification. For the measurements at 80, 60, and 40 keV, three detectors were mounted on each side of the chamber, 15° apart, with the defining slit 11.11 cm from the target. The slits used in these runs were rectangular, 0.953 cm by 0.635 cm. The solid angle was, therefore, 4.9 msr. The back slits on the polarimeter detectors, 16.51 cm from the target, were 1.270 cm by 0.635 cm with rounded edges from a 0.635 cm cutting tool, defining a 2.6 msr solid angle. For the lower yield 25 keV measurements, the 12.3 msr chamber detector solid angle was defined by circular slits, 1.270 cm diameter, and moved to a target-slit distance of 10.16 cm. A fourth pair of detectors was added in the chamber for these runs to increase the efficiency of data collection. The polarimeter slits were also 1.270-cm diameter circular slits, yielding a solid angle of 4.6 msr for the 25-keV runs.

As discussed in section 2.2.2, thin carbon films of approximately 150 $\mu g/cm^2$ thickness were mounted on the front slits of the chamber detector collimators. These films stopped elastically-scattered deuterons from striking the detectors while permitting the protons, tritons, and helium-3 nuclei to pass. The proper thickness of carbon was calculated using the data from [And77] so as to stop the deuterons while minimizing the energy loss for the helium-3 recoils. Electrons produced in the target and in the collimator films were prevented from striking the detector surface by small permanent magnets mounted on the collimator sides. On the polarimeter, 0.1 mil aluminized mylar films were used to stop the elastically scattered deuterons, and magnets were mounted to bend away electrons.

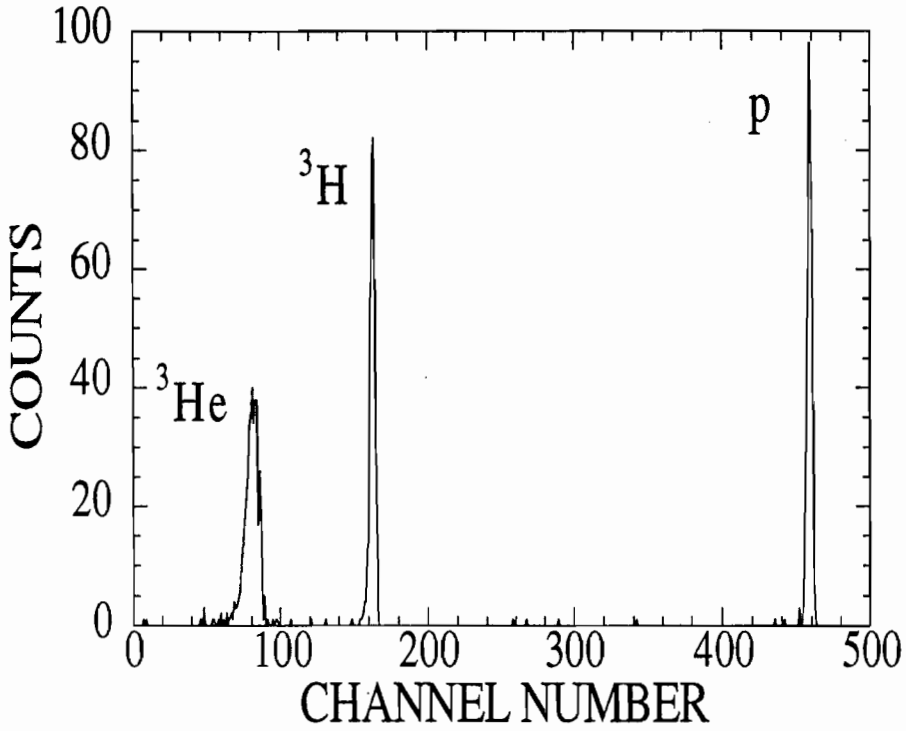


Figure 3-1. Spectrum from one of the polarimeter detectors ($\theta_{lab}$ = 10°) for 25 keV incident deuterons on a deuterated parapolyphenyl target (Figure 2 in [Fle92]).

A spectrum from the left monitor detector, taken at a beam energy of 25 keV in run 6255 is displayed in figure 3-1. The three charged-particle groups are clearly separated. Background subtraction, using commands from the TUNL XSYS data acquisition system [Gou81], was used when necessary, especially when low energy noise interferred with the helium-3 recoils. This occurred, for example, at angles near 90°, with the target at about 50° when helium-3 nuclei lost significant amounts of energy in passing through the target to the detector. In some cases, the recoils could not be cleanly separated from the noise and in those cases the helium-3 peaks were not summed.

### 3.2.2 Data acquisition

*80, 60, and 40 keV runs*

The data acquisition scheme for the 80, 60, and 40 keV runs is displayed in figures 3-2 and 3-3. Signals from the detectors travel through microdot cables in the scattering chamber through vacuum feedthrus to the preamps in the low energy bay then via 90 ohm coaxial cables to the amplifiers in the control room. For the chamber detectors, each left and right detector pair was routed into a single Northern ADC. For the polarimeter, all four signals were fed into one of the Lecroy 12-input ADC units. Pulser signals for dead time calculation were sent through the electronics for the right detectors for the chamber pairs and through the down detector for the polarimeter. Data were stored in a DEC MicroVax 3500 workstation.

State switching for the 80, 60, and 40 keV runs was controlled by software instruction to the TUNL Output Register. The bits of the output register were used to

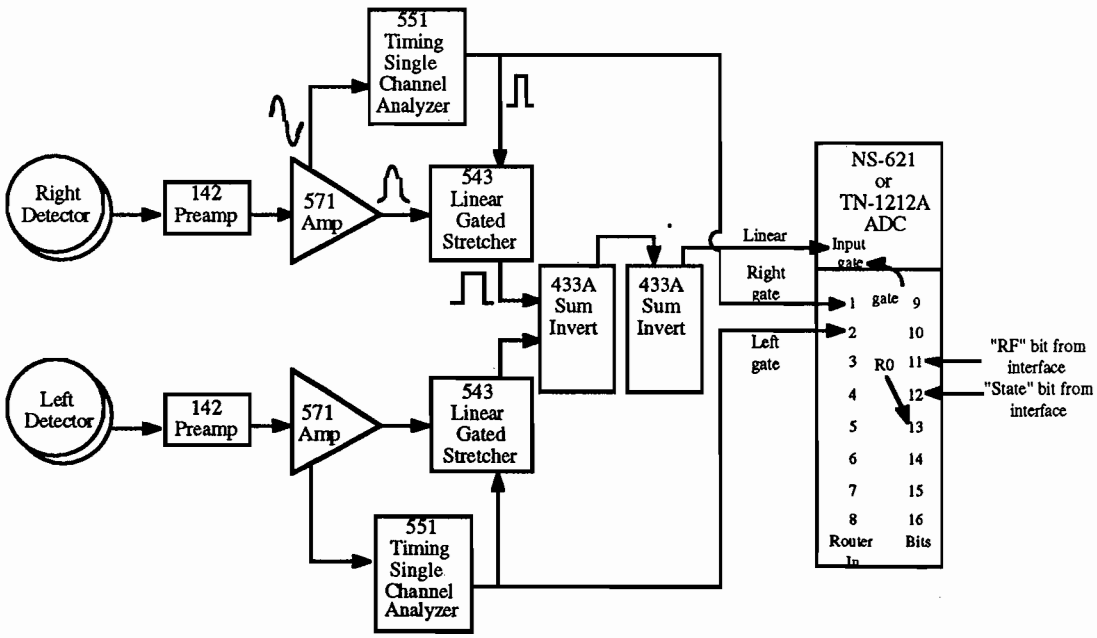


Figure 3-2. Data acquisition electronics for one of the left-right pair of chamber detectors. The model number refer to EG&G ORTEC modules, unless specified.

control the transition units on the polarized ion source, to store the energy signals in the proper data areas, and to increment the appropriate scalers. The command file which controlled data collection performed the following tasks at each state change:

1) Started a run in a particular state.

2) Waited for a specified number of seconds while counts were stored in the appropriate data areas.

3) Halted data collection once the time expired.

4) Set the bits on the output register to the proper values for the next state.

5) Waited a short period while the ABPIS transition unit magnets stabilized.

6) Returned to step 1).

In order to minimize the effects of deuterium depletion in the targets, the states were switched once every 60 seconds. One complete "loop" consisted of states collected in the pattern 3-1-2-2-1-3, so that, to first-order, target depletion effects were unimportant. A given "run" stored in the computer consisted of several (typically 5 to 10) loops.

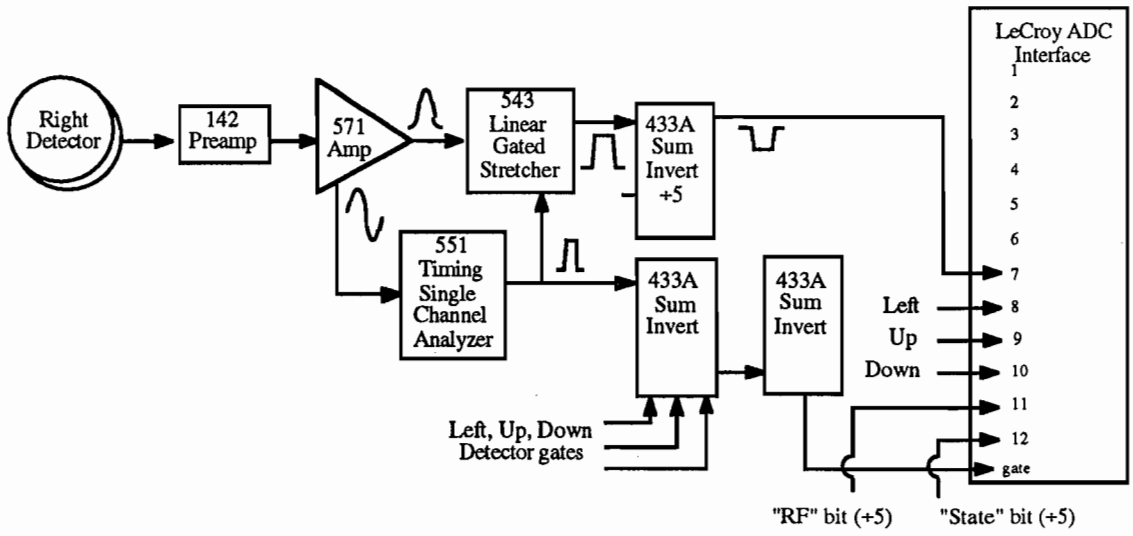


Figure 3-3. Data acquisition electronics for one of the polarimeter detectors.

*25 keV run*

The medium field transition units were installed and tested on the source just prior to the 25 keV run (see section 2.1.2). This was fortuitous, indeed, because compared to the previous method of preparing the beam, the medium field units permit much faster state switching for the same states because rf power supplies, rather than magnetic fields, are switched off and on. Deuterated parapolyphenyl targets were used in the 25-keV run, and deuterium depletion was of greater concern. Any systematic errors caused by such depletion were reduced by employing state switching every few hundred milliseconds.

It is impossible to control state switching on the several hundred millisecond timescale using software control as described above, since control of the output register is a slow process. Instead, we borrowed some of the technology used by the

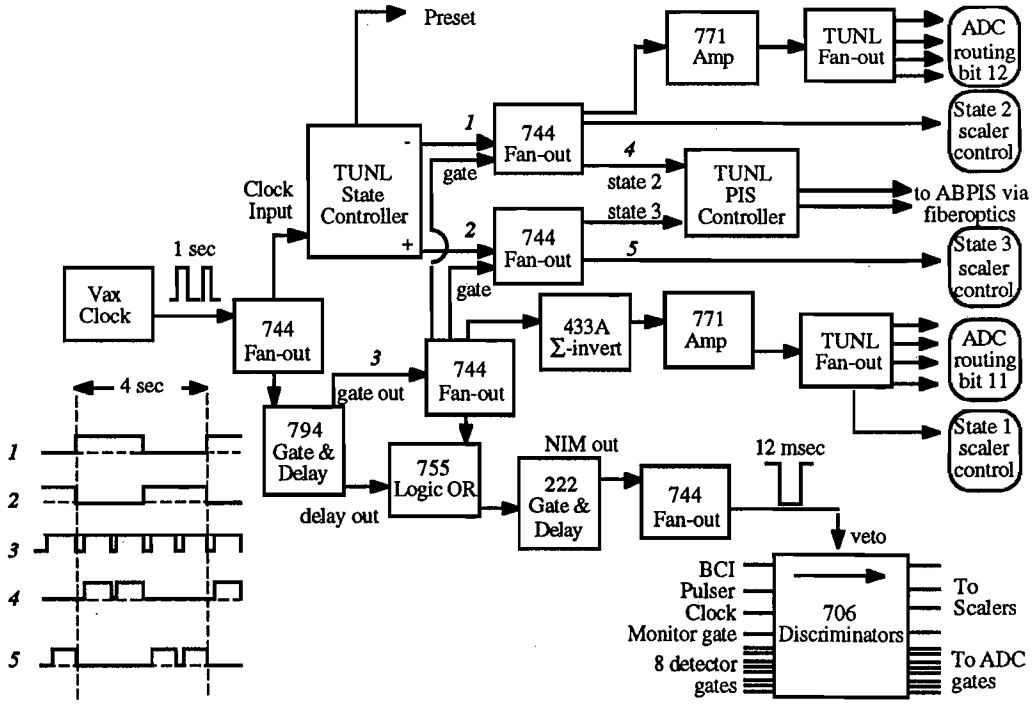


Figure 3-4. The scheme for rapid state-switching, employed for the 25-keV experiments.

polarized-target group at TUNL, and used the VAX clock to control state switching. The polarized target group had designed a circuit to produce high and low levels at the input clock frequency, suitable for their two-polarization state needs. This device was used to generate the necessary control signals for our three-state method. This system is shown in figure 3-4. This fast state changing system has been modified since the 25-keV run, so this diagram is outdated. Here the state switching sequence is 3-1-3-1-2-1-2-1, with data collected for 270 msec for each state 1 step and 730 msec for the steps in states 2 and 3. For 12 msec following each state change a veto signal was generated to halt storage of data and scalers while the transition unit was responding. The data acquisition schemes in figures 3-2 and 3-3 were modified accordingly.

## IV. Data reduction : Numbers

The counts collected in the spectra were combined to form tensor analyzing powers according to the prescriptions given in section 3.1. In order to do this, the actual reaction energy had to be determined, as well as the polarization of the beam from some absolute standard. In addition, the errors on the measurements were estimated after careful consideration.

### 4.1. Determination of the reaction energies

The deuterons in the beam strike the target with some intial energy, $E_d$ , and lose energy as they traverse the target. Because of the strong energy dependence of the cross section, averaging over the target thickness is an important consideration. Consider a target divided into N layers. The beam enters the first layer with an initial energy $E_d$ and produces reaction products at a rate proportional to $\sigma(E_d)\,\Delta t_d$, the product of the cross section at $E_d$ and the deuterium thickness in the layer, $\Delta t_d$. In the next layer, the beam energy is reduced by the total energy loss from the previous layer. The cross section for the reaction changes accordingly. We define the cross-section weighted reaction energy as

$$E_R = \frac{\sum_{i=1}^{N} E_i \sigma_{tot}(E_i)}{\sum_{i=1}^{N} \sigma_{tot}(E_i)} \tag{4.1}$$

where the energy in the $(i+1)^{th}$ layer is

$$E_{i+1} = E_i - \sum_a (stopping\ power)_a (\Delta t)_a \qquad (4.2)$$

and the sum over "a" represents the various elements in the target. Our convention is to use $E_d$ to indicate the incident energy of the beam and $E_R$ to indicate the cross-section weighted reaction energy (4.1). This reaction energy is calculated for a target of known thickness and composition by using the stopping powers reported in [And77]. The target components are assumed to be uniformly distributed throughout the target.

Table 4.1 Target energy summary. All energies are in keV.

| Batch | TAP | $E_{entrance}$ | $E_{exit}$ | $E_R$ | 50% thicker | 50% thinner |
|---|---|---|---|---|---|---|
| 02/24/91 | Azz80 | 80 | 69.8 | 75 | 73 | 78 |
| 06/22/91 | Azz60 | 60 | 49.0 | 55 | 53 | 57 |
| 07/04/91 | Azz60 | 60 | 55.8 | 58 | 57 | 59 |
| 07/25/91 | Ayy40 | 40 | 36.4 | 38 | 38 | 39 |
| 07/29/91 | Azz40 | 40 | 37.0 | 39 | 38 | 39 |
| 10/10/91 | Ayy80 | 80 | 71.6 | 76 | 74 | 78 |
| | Ayy60 | 60 | 52.4 | 56 | 55 | 58 |
| 10/30/91 | Ayy80 | 80 | 70.7 | 76 | 74 | 78 |
| | Ayy60 | 60 | 51.6 | 56 | 54 | 58 |
| 11/01/91 | Ayy60 | 60 | 55.0 | 58 | 56 | 59 |
| | Ayy40 | 40 | 35.7 | 38 | 37 | 39 |
| 01/20/92 | Ayy40 | 40 | 36.8 | 38 | 38 | 39 |
| 06/09/92 | Azz25 | 25 | 9.8 | 21 | 21 | 22 |
| | Ayy25 | 25 | 9.8 | 21 | 21 | 22 |
| 06/25/92 | Azz25 | 25 | 6.6 | 21 | 21 | 22 |
| | Azz25 | 25 | 6.6 | 21 | 21 | 22 |

The thicknesses and compositions for the target batches used in the data collection are listed in Table 2.1 in section 2.3.4. The mean reaction energies are reported in Table 4.1. The second column, labelled "TAP" indicates the observable and the incident energy for the measurement performed using targets from the batch. In section 2.3.4 the overestimate of the target thickness uncertainty was chosen as 50%, and this is reflected in the last two columns in Table 4.1. The effect of this uncertainty on the determination of the beam polarization is discussed in the next section.

## 4.2 Calibration of the D(d,p)$^3$H 10° polarimeter

The calibration of the D(d,p)$^3$H polarimeter has been described in [Fle92], but relevant sections of this description are repeated here for completeness. The calibration data for the polarimeter comes from [Tag92] and additional measurements performed at the University of Tsukuba, Japan.

Angular distribution measurements for the analyzing powers $iT_{11}$, $T_{20}$, $T_{21}$, and $T_{22}$ have been completed for D(d,p)$^3$H at deuteron energies of 30, 50, 70, and 90 keV by Tagishi et al. [Tag92] using deuterated parapolyphenyl thin film targets. For the tensor analyzing powers, these data were obtained from 0° to 160° in 10° steps using proportional gas counters and near 180° using an annular solid state detector. In addition to the measurements reported in [Tag92], angular distributions in 20° increments have been measured at energies of 20, 40, 60, and 80 keV. Polarized beam was provided by the University of Tsukuba Tandem Accelerator Center Lamb-shift polarized ion source [Tag79], and the beam polarization was determined at the target position by the quench-ratio method [Ohl71] which we now describe briefly.

The polarization of a deuteron beam produced in a Lamb-shift source results from the admixture of the 100% polarized $^2$H(2S) metastable atoms and an unpolarized background component from $^2$H(1S) atoms. In the quench-ratio method the beam current is measured with and without the $^2$H(2S) atoms quenched so that the magnitude

of the background component can be determined. The beam polarization determination from the quench ratio is estimated to be correct to within 2%, with an overall normalization uncertainty of 4% for the Tsukuba measurements.

Calibration of the TUNL D(d,p)$^3$H polarimeter required determination of $A_{zz}$ as a function of energy for the protons collected at a lab angle of 10°. The data at 20, 40, 60, and 80 keV do not include 10° measurements, so these data were fitted and the desired values interpolated from the fits. Although the 30, 50, 70, and 90 keV data include measurements at 10°, values obtained from fits to the angular distributions were used to provide a consistent data set and to minimize sensitivity to measurements at a single angle.

At each of the eight energies, the $T_{20}$ angular distributions were fitted according to the usual Legendre polynomial expansion with the angle θ given in the CM system. The data were eventually converted to $A_{zz}$ (= $\sqrt{2}$ $T_{20}$).

$$T_{20}(\theta) = \frac{1}{\sigma_0(\theta)} \sum_{L=0}^{L_{max}} C_L P_L(\cos\theta) \tag{4.3}$$

The unpolarized cross section $\sigma_0(\theta)$ at each energy was simultaneously fit to the data of Brown et al. [Bro90]:

$$\sigma_0(\theta) = \sum_{L=0,2,4} A_L P_L(\cos\theta) \tag{4.4}$$

In this differential cross section expansion the odd-L terms vanish because the particles in the entrance channel are identical. For the fits to $T_{20}(\theta)$ the summation was terminated at $L_{max} = 4$, which is consistent with the cutoff used in [Tag92]. Legendre polynomial expansion coefficients which minimized $\chi^2$ are given in Table 4.2. These expansion coefficients, $A_L$ and $C_L$, are consistent, within error estimates, with those given for $\sigma_0(\theta)$ in [Bro90], and, for the 30, 50, 70, and 90 keV $T_{20}$ fits, with those

given in [Tag92]. These fits were used to calculate $T_{20}(\theta_{lab} = 10°)$ for the protons, and these values (converted to $A_{zz}$) are given in Table 4.3.

The errors on the $T_{20}$ values estimated from the fits include both uncorrelated and correlated terms. Therefore, since

$$T_{20}(\theta) = \frac{\sigma_{20}(\theta)}{\sigma_0(\theta)} = \frac{\sum_{L=0}^{L_{max}} C_L P_L(\cos\theta)}{\sum_{L=0,2,4} A_L P_L(\cos\theta)} \tag{4.5}$$

the appropriate error expression is

$$\begin{aligned}
[\Delta T_{20}(\theta)]^2 = \; & \frac{1}{[\sigma_0(\theta)]^2}\left\{\sum_{L=0}^{L_{max}} [\Delta C_L P_L(\cos\theta)]^2 \right. \\
& \left. + \sum_{K,L}^{L\neq K} \Delta C_L \Delta C_K \rho(C_L, C_K) P_L(\cos\theta) P_K(\cos\theta)\right\} \\
& + \left\{\frac{\sigma_{20}(\theta)}{[\sigma_0(\theta)]^2}\right\}^2 \left\{\sum_{L=0,2,4} [\Delta A_L P_L(\cos\theta)]^2 \right. \\
& \left. + \sum_{K,L}^{L\neq K} \Delta A_L \Delta A_K \rho(A_L, A_K) P_L(\cos\theta) P_K(\cos\theta)\right\} \\
& - \left\{\frac{\sigma_{20}(\theta)}{[\sigma_0(\theta)]^3}\right\}\left\{\sum_{K,L}^{L\neq K} \Delta C_L \Delta A_K \rho(C_L, A_K) P_L(\cos\theta) P_K(\cos\theta) \right. \\
& \left. + \sum_{K,L}^{L\neq K} \Delta A_L \Delta C_K \rho(A_L, C_K) P_L(\cos\theta) P_K(\cos\theta)\right\}
\end{aligned} \tag{4.6}$$

Here $\rho(A_K, C_L)$ is the correlation coefficient between the expansion coefficients $A_K$ and $C_L$. The correlation coefficients were calculated as part of the fitting routine. Their interpretation is discussed in section 4.3.1. The errors on the expansion coefficients result from the statistical errors of the measurements, so the overall normalization uncertainty of 4% from [Tag92] must be applied here as well. The fits and the data are shown in figures 4-1 and 4-2.

Table 4.2. Legendre polynomial expansion coefficients for $T_{20}$ and $D(d,p)^3H$, fit to the data of [Bro90,Tag92] and unpublished data from the Univ. of Tsukuba group.

| $E_d$ | 20 keV | 30 keV | 40 keV | 50 keV |
|---|---|---|---|---|
| $A_0$ | 0.0216±.0006 | 0.0949±.0012 | 0.211±.0017 | 0.356±.0025 |
| $A_2$ | 0.0014±.0015 | 0.0130±.0031 | 0.047±.0044 | 0.0756±.0065 |
| $A_4$ | 0.0003±.0015 | 0.0022±.0034 | 0.0104±.0052 | 0.0016±.0072 |
| $C_0$ | -0.00087±.0002 | -0.0057±.0006 | -0.0149±.0013 | -0.031±.0014 |
| $C_1$ | 0.00013±.0002 | 0.00145±.0008 | -0.0028±.0020 | -0.014±.0019 |
| $C_2$ | -0.0119±.0006 | -0.060±.0017 | -0.125±.0031 | -0.215±.0037 |
| $C_3$ | 0.0029±.0004 | 0.013±.0013 | 0.024±.0030 | 0.0343±.0029 |
| $C_4$ | -0.00022±.0007 | -0.0031±.0019 | -0.0123±.0038 | -0.0078±.0041 |
| $\frac{\chi^2}{d.f.}$ | 0.69 | 0.74 | 0.87 | 1.8 |

Table 4.2 continued.

| $E_d$ | 60 keV | 70 keV | 80 keV | 90 keV |
|---|---|---|---|---|
| $A_0$ | 0.524±.0035 | 0.697±.0041 | 0.868±.0048 | 1.05±.0030 |
| $A_2$ | 0.123±.0089 | 0.190±.010 | 0.259±.012 | 0.333±.0075 |
| $A_4$ | -0.0008±.0104 | 0.010±.011 | 0.0382±.014 | 0.0315±.0084 |
| $C_0$ | -0.0481±.0026 | -0.0700±.0021 | -0.093±.0034 | -0.119±.0038 |
| $C_1$ | -0.0319±.0040 | -0.0704±.0032 | -0.0997±.0057 | -0.127±.0063 |
| $C_2$ | -0.303±.0061 | -0.394±.0056 | -0.491±.0084 | -0.606±.0083 |
| $C_3$ | 0.0278±.0061 | 0.0213±.0048 | 0.0139±.0083 | 0.0232±.0094 |
| $C_4$ | -0.0169±.0077 | -0.0199±.0063 | -0.0127±.010 | -0.0458±.010 |
| $\frac{\chi^2}{d.f.}$ | 0.918 | 1.7 | 2.5 | 1.0 |

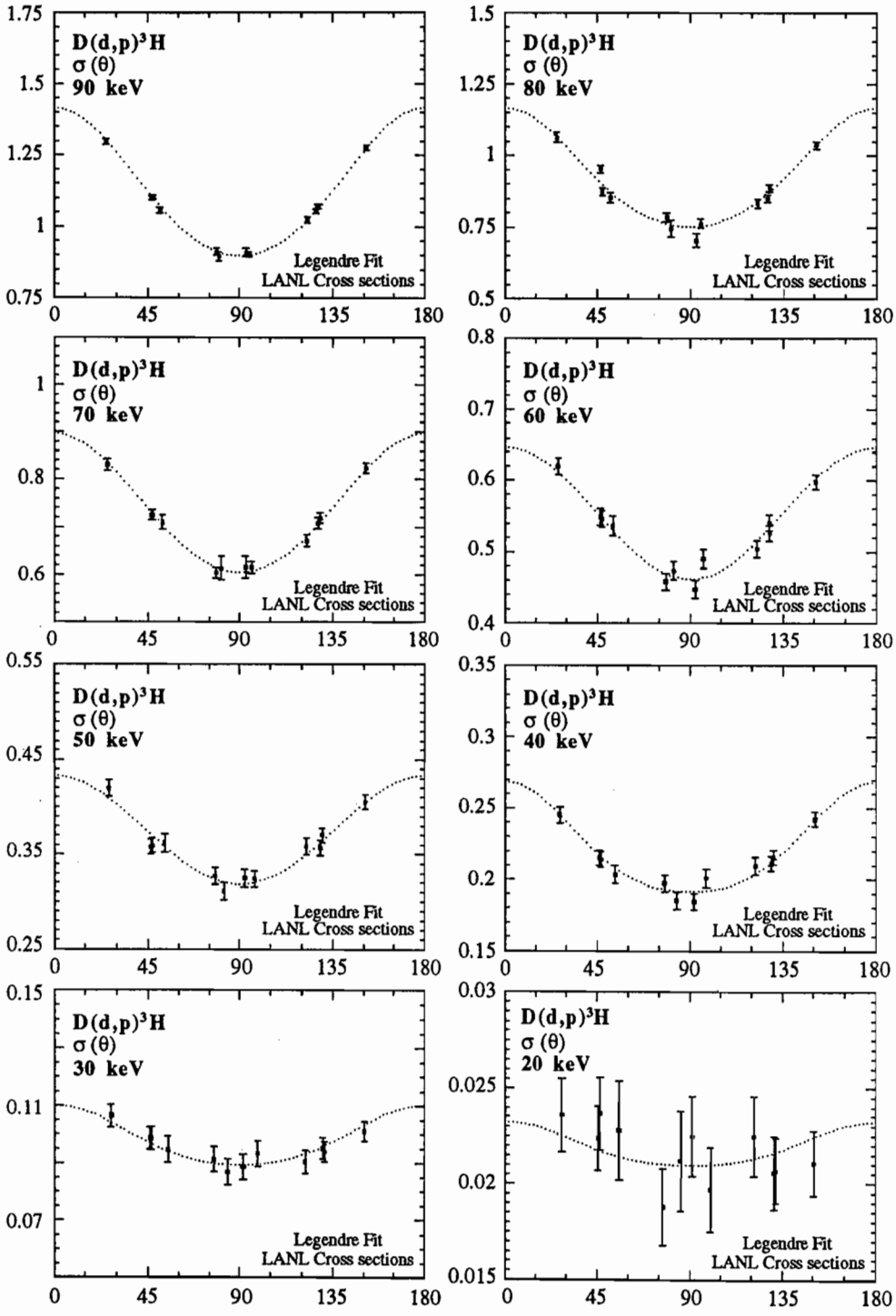


Figure 4-1. The Legendre polynomial fits to the cross section data of [Bro90]. The cross sections, in units of millibarns, are plotted as a function of angle in the center of mass system. The dotted lines are the Legendre polynomial fits used in the polarimeter calibration.

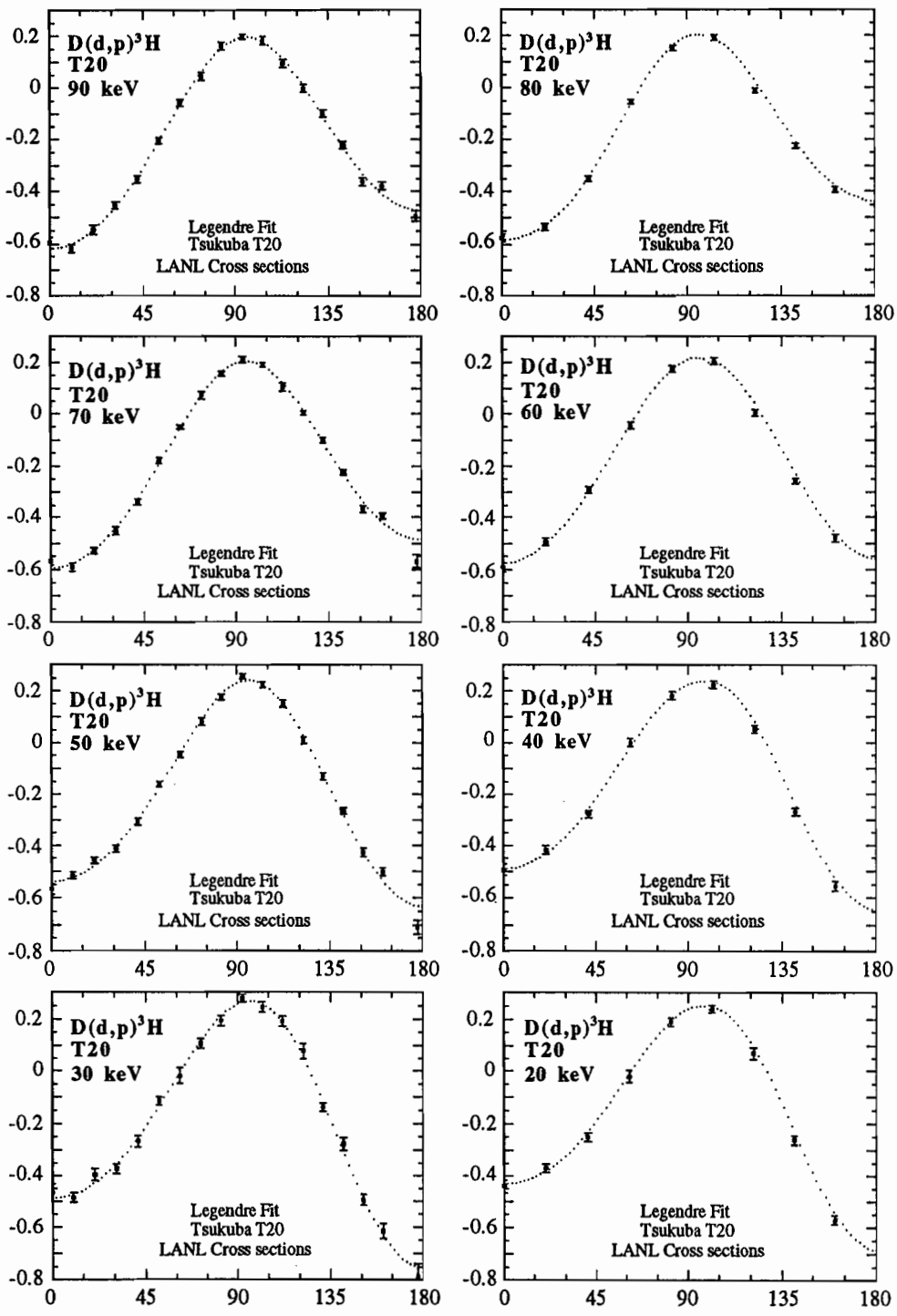


Figure 4-2. The Legendre polynomial fits (dotted lines) to the analyzing power data of [Tag92] and additional data [Y. Tagishi, private communication], plotted as a function of center of mass angle.

Table 4.3. Results of the Legendre polynomial fits to angular distributions for $A_{zz}(10°)$.

| Beam Energy $E_d$ (keV) | Reaction Energy $E_R$ (keV) | $A_{zz}(10°)$ (from Legendre fits) |
|---|---|---|
| 20 | 18.0 ± 0.4 | -0.590 ± 0.022 |
| 30 | 27.4 ± 0.6 | -0.668 ± 0.018 |
| 40 | 36.9 ± 0.8 | -0.668 ± 0.020 |
| 50 | 46.6 ± 0.9 | -0.741 ± 0.012 |
| 60 | 56.3 ± 1.0 | -0.788 ± 0.017 |
| 70 | 66.1 ± 1.0 | -0.816 ± 0.011 |
| 80 | 75.9 ± 1.0 | -0.809 ± 0.015 |
| 90 | 85.8 ± 1.1 | -0.850 ± 0.014 |

The analyzing power data for these fits were taken using deuterated parapolyphenyl ($(C_6D_4)_n$) thin film targets with deuterium thicknesses in the range 0.7 $\mu g/cm^2$ to 1.2 $\mu g/cm^2$ [Tag92], and the carbon content was estimated from the stoichiometric formula for the polymer. The reaction energies, $E_R$, appropriate for these targets are reported in Table 4.3. The values given there correspond to targets with a deuterium thickness of 0.9 $\mu g/cm^2$ , which is in the middle of the range of thicknesses used. In order to estimate the uncertainty in this procedure, the reaction energies were recalculated using the endpoint values for the thicknesses, and the uncertainties listed result from this calculation. These uncertainties on the energy are therefore not statistical errors. In all cases the uncertainty in the reaction energy is small (less than 2%), and in the calculation of the calibration curve these uncertainties are ignored because of their negligible effect.

Some additional discussion of the angular distribution fits is necessary. The $\chi^2$ values for the 80 keV and 50 keV fits are rather large, and these fits fail a statistical goodness-of-fit test at the 25% level. As a test, these two energies were omitted from the set of $A_{zz}(10°)$, and the energy distribution function was refitted as described above. The resulting calibration curve fell within the one standard deviation band of the original fit, which was based on all eight energies. The conclusion from this test was that the "suspicious" values from the 80 keV and 50 keV fits do not drastically alter the calibration, and so the original energy distribution fit remains the calibration curve for the polarimeter.

The error which results from averaging over the opening angle of the detectors used in the Tsukuba measurements ($\Delta\theta = 3°$) was estimated to lowest order by determining the Taylor expansion of the Legendre polynomials about $\theta$ and integrating over the angle opening. Since the corrections to the $A_{zz}$ values were less than 0.0012, this effect was deemed negligible in comparison with other errors.

The simultaneous fitting of analyzing power data measured with solid $(C_6D_4)_n$ targets and cross section data measured with a gas target requires consideration, since the energy averaging is different for the two targets. The absence of carbon atoms in the gas target greatly reduces the energy loss in the target. The effect of combining measurements made at two different reaction energies is largest at the lowest energies, where the energy dependence of the cross section is greatest. We have estimated this effect using the data from [Bro90]. For the 20 keV data, the ratio of the total cross section at the reaction energy for the polarized data to that at the reaction energy for the unpolarized cross section data is 0.60. As a test, the differential cross section values were multiplied by 0.60, to approximate the cross section distribution at the $T_{20}$ reaction energy, and the fitting procedure was repeated. The resulting analyzing powers were identical, within errors, to the original values, demonstrating that this effect is not important in our measurements.

Figure 4-3 shows the energy dependence of the analyzing powers determined for protons detected at a lab angle of 10°. This energy dependence is well reproduced by a second-order polynomial, indicated by a solid line on the figure.

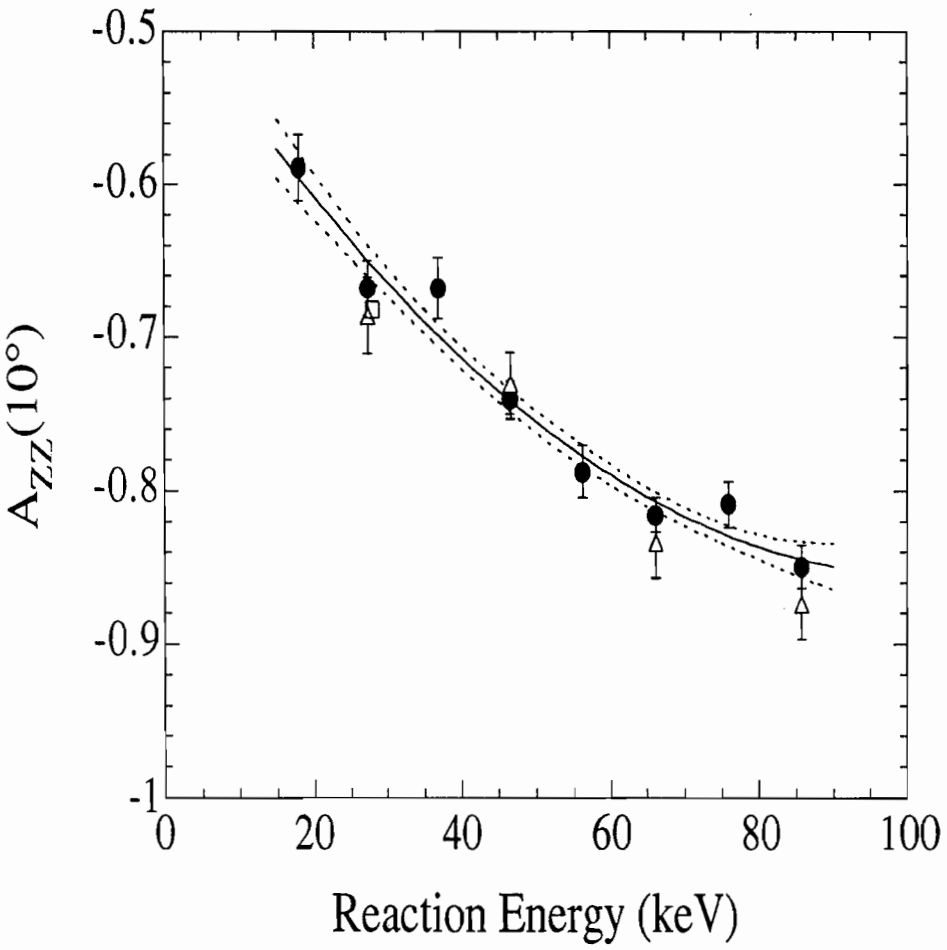


Figure 4-3 Energy dependence of $A_{ZZ}(10°)$ as determined from Legendre polynomial fits (solid circles). The second-order polynomial fit to these values is indicated by the solid line, and the dashed lines indicate the uncertainty of the fit. The actual data at 10° from [Tag92] is shown (open triangles), as is the result from a fit a 28 keV given in [Bec92] (open square). This last point was not used in the fit and is given for comparison. (Figure 3 in [Fle92].)

Specifically, the polynomial which results from linear least-squares fitting is giving by

$$A_{zz} = -0.4729 - 7.469\times10^{-3}E_R + 3.64\times10^{-5}E_R^2 \qquad (4.7)$$

where $E_R$ is the reaction energy measured in keV. The $\chi^2$ value for this fit is 6.4 with 5 degrees of freedom. The coefficients and the error terms for this fit were calculated using the matrix method for least squares fitting described, for example, in [Bar89]. The uncertainty of this energy fit (including correlated error terms, section 4.3.1) is given by

$$\begin{aligned}(\Delta A_{zz})^2 = {} & 1.376\times10^{-3} - 1.033\times10^{-4}E_R + 2.975\times10^{-6}E_R^2 \\ & - 3.737\times10^{-8}E_R^3 + 1.721\times10^{-10}E_R^4\end{aligned} \qquad (4.8)$$

and the dashed lines on figure 4.3 indicate these errors. For comparison, the actual measured data at 10° [Tag92] are also shown on the figure, as is the result for 10° from the Legendre expansion at 28 keV given in [Sch92]. There is satisfactory agreement with the point from [Sch92], which was not included in our fitting.

The reaction energies reported in Table 4.1 can now be used to compute the monitor analyzing powers for data. The results are shown in Table 4.4. With one exception (the 6/22/91 batch), the monitor analyzing powers calculated assuming targets which are 50% thicker or thinner are within one standard deviation from the value computed for the assumed reaction energy. Therefore, variations of the target thicknesses as large as 50% do not affect the polarization determination for the runs. The overall reaction energy and monitor analyzing power for each observable at each of the four deuteron energies were determined from the results from Table 4.4, with the results weighted to reflect the amount of data collected with any given batch of targets. The results are displayed in Table 4.5.

Table 4.4 Monitor analyzing powers for the data. All energies are in keV

| Batch | TAP | $E_{entrance}$ | $E_R$ | $A_{zz}(10°,E_R)$ | $A_{zz}(10°,E_R)$ 50% thicker | $A_{zz}(10°,E_R)$ 50% thinner |
|---|---|---|---|---|---|---|
| 02/24/91 | Azz80 | 80 | 75 | -0.828±.007 | -0.823±.007 | -0.832±.007 |
| 06/22/91 | Azz60 | 60 | 55 | -0.773 | -0.765 | -0.781 |
| 07/04/91 | Azz60 | 60 | 58 | -0.783 | -0.780 | -0.786 |
| 07/25/91 | Ayy40 | 40 | 38 | -0.705 | -0.701 | -0.709 |
| 07/29/91 | Azz40 | 40 | 39 | -0.707 | -0.704 | -0.710 |
| 10/10/91 | Ayy80 | 80 | 76 | -0.830 | -0.826 | -0.833 |
| | Ayy60 | 60 | 56 | -0.774 | -0.772 | -0.783 |
| 10/30/91 | Ayy80 | 80 | 76 | -0.829 | -0.842 | -0.833 |
| | Ayy60 | 60 | 56 | -0.776 | -0.771 | -0.783 |
| 11/01/91 | Ayy60 | 60 | 58 | -0.782 | -0.778 | -0.786 |
| | Ayy40 | 40 | 38 | -0.704 | -0.700 | -0.708 |
| 01/20/92 | Ayy40 | 40 | 38 | -0.706 | -0.703 | -0.709 |
| 06/09/92 | Azz25 | 25 | 21 | -0.613±.014 | -0.613±.014 | -0.618±.014 |
| | Ayy25 | 25 | 21 | -0.613 | -0.613 | -0.618 |
| 06/25/92 | Azz25 | 25 | 21 | -0.613 | -0.613 | -0.618 |
| | Azz25 | 25 | 21 | -0.613 | -0.613 | -0.618 |

Table 4.5 The reaction energies and monitor analyzing powers for the observables.

| Observable | $E_d$ (keV) | $E_R$(keV) | $A_{zz}$ |
|---|---|---|---|
| $A_{zz}$ | 80 | 75 | -0.828±.007 |
| | 60 | 55 | -0.773±.007 |
| | 40 | 39 | -0.707±.007 |
| | 25 | 21 | -0.613±.014 |
| $A_{yy}$ | 80 | 76 | -0.829±.007 |
| | 60 | 56 | -0.777±.007 |
| | 40 | 38 | -0.705±.007 |
| | 25 | 21 | -0.613±.014 |

### 4.3. Tensor analyzing power data reduction

With the polarimeter calibration given by eqs. (4.7) and (4.8), the calculation of the analyzing powers from the spectra proceeds as described in section 3.1. Using the XSYS data acquisition and analysis system [Gou81], the counts in each of the three peaks for the three states for each chamber and monitor detector were gated and extracted. For some cases, the helium-3 peaks were very low in the spectrum and the background at very low energy interfered with the proper extraction of these counts. In these cases, the helium-3 peaks were rejected. In other cases, a small background component was subtracted from the peak of interest. A system of FORTRAN and command codes, written by the author, was used for data reduction.

At a given angle, many runs were collected. The appropriate tensor analyzing power, $A_{zz}$ or $A_{yy}$, and its error were calculated for each run for the protons, tritons, and helium-3 nuclei, and the results were combined into a weighted mean and the error

on the mean. The $A_{zz}$ and $A_{yy}$ results were further combined so that the combination $A_{xx}$-$A_{yy}$ could be reported. This is further described in section 4.3.2.

### 4.3.1. Error propagation and correlation coefficients

In section 3.1 the expressions for the tensor analyzing powers and polarizations were developed. For the $\beta = 0°$ measurement, the expressions were

$$P_{zz}^{(p)} = \frac{S-4}{2A_{zz}^{mon}} \tag{3.5}$$

$$A_{zz}(\theta) = \frac{2(R-1)}{\left(P_{zz}^{(2)} - RP_{zz}^{(3)}\right)} \tag{3.7}$$

and for $\beta = 90°$ ,

$$P_{zz}^{(p)} = \frac{4-S}{A_{zz}^{mon}} \tag{3.8}$$

$$A_{yy}(\theta) = \frac{2(R-1)}{\left(P_{zz}^{(2)} - RP_{zz}^{(3)}\right)} \tag{3.9}$$

In these expressions the quantity S was defined as

$$S = l + r + u + d = \left\{4 + 2P_{zz}^{(p)}A_{zz}^{mon}\right\}, \tag{3.4}$$

where the lower case letters referred to the ratios of the polarized to unpolarized counts for the monitor detectors. Similarly, the ratio R was defined as

$$R = \frac{S_2}{S_3} = \frac{l_2 + r_2}{l_3 + r_3} = \frac{\left\{2 + P_{zz}^{(2)}A_{zz}(\theta)\right\}}{\left\{2 + P_{zz}^{(3)}A_{zz}(\theta)\right\}} \tag{3.6}$$

for the left-right detector pair in the chamber .

To determine the statistical error on any function of several variables, the common procedure is to define the standard deviation on the function $f = f(a,b)$ by

$$\sigma_f{}^2 = \left(\frac{\partial f}{\partial a}\right)^2 \sigma_a{}^2 + \left(\frac{\partial f}{\partial b}\right)^2 \sigma_b{}^2 \tag{4.9}$$

thereby ignoring the correlated error terms. The reason often given for following this procedure is that the variables are assumed to be independent. In general, however, the appropriate expression for the error is

$$\sigma_f{}^2 = \left(\frac{\partial f}{\partial a}\right)^2 \sigma_a{}^2 + \left(\frac{\partial f}{\partial b}\right)^2 \sigma_b{}^2 + 2\rho(a,b)\sigma_a{}^2\sigma_b{}^2 \tag{4.10}$$

where the ρ(a,b) is the correlation coefficient between variables a and b and the σ values are their standard deviations.

The expression (4.10) results in a natural way, as can be easily seen. If small deviations for the variables a and b are denoted by δa and δb, then the deviation for any function of a and b is

$$\delta f(a,b) = \left(\frac{\partial f}{\partial a}\right)\delta a + \left(\frac{\partial f}{\partial b}\right)\delta b \tag{4.11}$$

The square of this quantity is written:

$$[\delta f(a,b)]^2 = \left(\frac{\partial f}{\partial a}\right)^2 \delta a^2 + \left(\frac{\partial f}{\partial b}\right)^2 \delta b^2 + 2\left(\frac{\partial f}{\partial a}\right)\left(\frac{\partial f}{\partial b}\right)\delta a\delta b \tag{4.12}$$

This expression holds for a single measurement. After taking the average of many measurements, we estimate

$$\sigma_f{}^2 = \left(\frac{\partial f}{\partial a}\right)^2 \sigma_a{}^2 + \left(\frac{\partial f}{\partial b}\right)^2 \sigma_b{}^2 + 2\left(\frac{\partial f}{\partial a}\right)\left(\frac{\partial f}{\partial b}\right)\rho(a,b)\sigma_a{}^2\sigma_b{}^2 \tag{4.13}$$

In (4.13) the standard deviation $\sigma_a^2$ is the statistical estimator for $(\delta a)^2$ and similarly for b. The estimator for $\rho(a,b)$ is given by

$$\rho(a,b) = \frac{\sum_i (a_i - \bar{a})(b_i - \bar{b})}{\left\{\sum_j (a_j - \bar{a})^2 \sum_k (b_k - \bar{b})^2\right\}^{\frac{1}{2}}} \tag{4.14}$$

where $\bar{a}$ and $\bar{b}$ are the mean values of a and b. The magnitude of $\rho$ is bounded by unity, but $\rho$ may be of either sign. Therefore, if two variables are indeed independent, calculation of (4.14) should indicate so explicitly (assuming that a suitably large number of measurements has been performed) by yielding a vanishing $\rho(a,b)$.

To illustrate the increased complexity induced by this procedure, the appropriate expression for the error on the variable S in (3.4) is then

$$\begin{aligned}
\Delta S^2 = {} & l^2\left(\frac{\Delta L_p}{L_p}\right)^2 + r^2\left(\frac{\Delta R_p}{R_p}\right)^2 + u^2\left(\frac{\Delta U_p}{U_p}\right)^2 + d^2\left(\frac{\Delta D_p}{D_p}\right)^2 \\
& + l^2\left(\frac{\Delta L_u}{L_u}\right)^2 + r^2\left(\frac{\Delta R_u}{R_u}\right)^2 + u^2\left(\frac{\Delta U_u}{U_u}\right)^2 + d^2\left(\frac{\Delta D_u}{D_u}\right)^2 \\
& + 2\rho(L_u, R_u)\left[\frac{-l\Delta L_u}{L_u}\right]\left[\frac{-r\Delta R_u}{R_u}\right] + \text{ 5 similar terms} \\
& + 2\rho(L_p, R_p)\left[\frac{\Delta L_p}{L_u}\right]\left[\frac{\Delta R_p}{R_u}\right] + \text{ 5 similar terms} \\
& - 2\rho(L_p, L_u)\left[\frac{\Delta L_p}{L_u}\right]\left[\frac{-l\Delta L_u}{L_u}\right] + \text{ 3 similar terms} \\
& - 2\rho(L_p, R_u)\left[\frac{\Delta L_p}{L_u}\right]\left[\frac{-r\Delta R_u}{R_u}\right] + \text{ 5 similar terms} \\
& - 2\rho(R_p, L_u)\left[\frac{\Delta R_p}{R_u}\right]\left[\frac{-l\Delta L_u}{L_u}\right] + \text{ 5 similar terms}
\end{aligned} \tag{4.15}$$

At first glance, including so many terms may appear to be disastrous, indicating that if the correlation coefficients are non-vanishing, the error in S may be large. However, closer inspection reveals that many of the terms are negative, and the net result might be smaller than that which ignores the correlated terms. A similar error expression exists for R:

$$
\begin{aligned}
\Delta R^2 = {} & R^2\left\{\frac{l_2^{\,2}}{S_2^{\,2}}\left(\frac{\Delta L_2}{L_2}\right)^2+\frac{r_2^{\,2}}{S_2^{\,2}}\left(\frac{\Delta R_2}{R_2}\right)^2+\frac{l_3^{\,2}}{S_3^{\,2}}\left(\frac{\Delta L_3}{L_3}\right)^2+\frac{r_3^{\,2}}{S_3^{\,2}}\left(\frac{\Delta R_3}{R_3}\right)^2\right\} \\
& + R^2\left\{\left[\frac{l_3}{S_3}-\frac{l_2}{S_2}\right]^2\left(\frac{\Delta L_u}{L_u}\right)^2+\left[\frac{r_3}{S_3}-\frac{r_2}{S_2}\right]^2\left(\frac{\Delta R_u}{R_u}\right)^2\right\} \\
& + 2R^2\rho(L_2,L_u)\frac{l_2}{S_2}\left(\frac{\Delta L_2}{L_2}\right)\left(\frac{\Delta L_u}{L_u}\right)\left[\frac{l_3}{S_3}-\frac{l_2}{S_2}\right] + \text{ similar term for right} \\
& - 2R^2\rho(L_3,L_u)\frac{l_3}{S_3}\left(\frac{\Delta L_3}{L_3}\right)\left(\frac{\Delta L_u}{L_u}\right)\left[\frac{l_3}{S_3}-\frac{l_2}{S_2}\right] - \text{ similar term for right} \\
& - 2R^2\rho(L_2,L_3)\frac{l_2}{S_2}\frac{l_3}{S_3}\left(\frac{\Delta L_2}{L_2}\right)\left(\frac{\Delta L_3}{L_3}\right) - \text{ similar term for right} \\
& + 2R^2\rho(L_1,R_2)\frac{r_2}{S_2}\left[\frac{l_3}{S_3}-\frac{l_2}{S_2}\right]\left(\frac{\Delta R_2}{R_2}\right)\left(\frac{\Delta L_u}{L_u}\right) + \text{ term with R,L switched} \\
& - 2R^2\rho(L_1,R_3)\frac{r_3}{S_3}\left[\frac{l_3}{S_3}-\frac{l_2}{S_2}\right]\left(\frac{\Delta R_3}{R_3}\right)\left(\frac{\Delta L_u}{L_u}\right) - \text{ term with R,L switched} \\
& - 2R^2\rho(L_2,R_3)\frac{r_3}{S_3}\frac{l_2}{S_2}\left(\frac{\Delta R_3}{R_3}\right)\left(\frac{\Delta L_2}{L_2}\right) + \text{ term with R,L switched} \\
& + 2R^2\rho(L_1,R_1)\left[\frac{l_3}{S_3}-\frac{l_2}{S_2}\right]\left[\frac{r_3}{S_3}-\frac{r_2}{S_2}\right]\left(\frac{\Delta L_u}{L_u}\right)\left(\frac{\Delta R_u}{R_u}\right) \\
& + 2R^2\rho(L_2,R_2)\frac{l_2}{S_2}\frac{r_2}{S_2}\left(\frac{\Delta L_2}{L_2}\right)\left(\frac{\Delta R_2}{R_2}\right) \\
& + 2R^2\rho(L_3,R_3)\frac{l_3}{S_3}\frac{r_3}{S_3}\left(\frac{\Delta L_3}{L_3}\right)\left(\frac{\Delta R_3}{R_3}\right)
\end{aligned}
\tag{4.16}
$$

The importance of including the correlation coefficients in our error analysis is indicated by the empirical fact that, for our data, values of r are as large as ±0.8 because we take *ratios* of observables arising from a common source. If r is arbitrarily set to zero, the statistical errors are overestimated by a factor of 2 over the present values.

In practice, we estimated the correlation coefficients according to (4.14) at each angle, using the set of runs measured for that angle as part of the data analysis. The error expressions for $\beta = 0°$ are

$$\left(\Delta P_{zz}\right)^2 = \left(\frac{\Delta S}{2A_{zz}^{mon}}\right)^2 + \left(\frac{P_{zz}}{A_{zz}^{mon}}\right)^2 \left(\Delta A_{zz}^{mon}\right)^2 \tag{4.17}$$

$$\left(\Delta A_{zz}\right)^2 = \left(\frac{A_{zz}}{R-1}\right)^2 (\Delta R)^2 + \left[\frac{A_{zz}}{P_{zz}^{(2)} - RP_{zz}^{(3)}}\right]^2 \left[\left(\Delta P_{zz}^{(2)}\right)^2 + \left(R\Delta P_{zz}^{(3)}\right)^2\right] \tag{4.18}$$

and for $\beta = 90°$ ,

$$\left(\Delta P_{zz}\right)^2 = \left(\frac{\Delta S}{A_{zz}^{mon}}\right)^2 + \left(\frac{P_{zz}}{A_{zz}^{mon}}\right)^2 \left(\Delta A_{zz}^{mon}\right)^2 \tag{4.19}$$

$$\left(\Delta A_{yy}\right)^2 = \left(\frac{A_{yy}}{R-1}\right)^2 (\Delta R)^2 + \left[\frac{A_{yy}}{P_{zz}^{(2)} - RP_{zz}^{(3)}}\right]^2 \left[\left(\Delta P_{zz}^{(2)}\right)^2 + \left(R\Delta P_{zz}^{(3)}\right)^2\right] \tag{4.20}$$

***A digression on correlation coefficients***

During data collection, it is usually impossible to collect the same integrated beam current in every run and for every state. It is inappropriate to calculate correlation coefficients by summing up raw counts in detectors from different runs taken with different integrated beam currents, deadtime corrections, and target thicknesses. Furthermore, our data reduction formalism was developed to eliminate the effects of such variations. The small case variables, l, r, u, and d, which appear in the polarization and analyzing power expressions are the deadtime corrected counts divided by the integrated beam current, the target thickness and the unpolarized cross section.

In estimating the correlation coefficients, the BCI, the deadtime, and the target thicknesses have all been factored out. The target thickness effect was taken into account by dividing the detector counts by the sum of the unpolarized counts in the monitor.

In addition, since some runs have better statistics than other runs, much effort was expended in trying to develop a weighted correlation coefficient, similar to a weighted mean. In the end, this effort was abandoned and the unweighted expression (4.14) was employed. This is not a major defect in our data reduction, because most of our runs where collected with approximately the same statistics; however, the problem merits some consideration and is not dealt with in statistics books we consulted.

At first glance it appears that there is a sensible and obvious way to define a weighted correlation coefficient, given the usual definition of the weighted mean. Consider a quantity x which has been measured N times, and each measurement, $x_i$, has some statistical error given by $\Delta x_i$. The weighted mean of these measurements is, for weights inversely proportional to the errors squared,

$$\bar{x} = \sum_i \frac{x_i}{(\Delta x_i)^2} \Big/ \sum_j \frac{1}{(\Delta x_j)^2}. \tag{4.21}$$

This can be rewritten as

$$\bar{x} = \frac{1}{N}\sum_i \left\{ \frac{x_i}{(\Delta x_i)^2} N \Big/ \sum_j \frac{1}{(\Delta x_j)^2} \right\} = \frac{1}{N}\sum_i x_i' \tag{4.22}$$

Equation (4.22) is simply the usual (unweighted) mean of a new variable $x_i'$:

$$x_i' = \frac{N\ x_i}{(\Delta x_i)^2} \Big/ \sum_j \frac{1}{(\Delta x_j)^2} \tag{4.23}$$

Therefore, it seems perfectly reasonable to define the new weighted correlation coefficient of (x, y) as the usual correlation coefficient of (x', y'). So far, everything

looks reasonable. For our experiments the probability for detecting a particle in a small time $\Delta t$ is $\mu\Delta t$, where $\mu$ is independent of time. The probability distribution which results for such a case is the Poisson distribution [Boa83]. Now, suppose that the variables (x, y) are governed by Poisson statistics, as in our counting experiments. Then, the standard deviation on measurement $x_i$ is estimated by $\sqrt{x_i}$ and the new variable $x_i'$ is

$$x_i' = \frac{N\ x_i}{\left(\sqrt{x_i}\right)^2} \Big/ \sum_j \frac{1}{\left(\sqrt{x_i}\right)^2} = \frac{N}{\sum_i \frac{1}{x_i}} = \text{constant} \tag{4.24}$$

Every term in the weighted mean sum is identical and equal to the mean itself! The correlation coefficient (4.14) then becomes undefined. The "obvious" candidate for the weighted correlation coefficient is found to be fundamentally flawed, at least for Poisson statistics which is of such importance in physics.

### 4.3.2. ($A_{xx}$-$A_{yy}$) from $A_{zz}$ and $A_{yy}$

It was simplest to introduce the data reduction formalism in terms of measuring $A_{yy}$ for $\beta = 90°$. However, the combination ($A_{xx}$-$A_{yy}$) is more often quoted, since it is proportional to the spherical tensor analyzing power $T_{22}$ and it is conveniently and simply expanded in terms of Legendre functions. Therefore, to report our results, $A_{yy}$ and $A_{zz}$ are combined. Since,

$$A_{xx} + A_{yy} + A_{zz} = 0 \tag{4.25}$$

then

$$\left(A_{xx} - A_{yy}\right) = -2A_{yy} - A_{zz} \tag{4.26}$$

and the error is given by

$$\Delta\left(A_{xx} - A_{yy}\right)^2 = 4\left(\Delta A_{yy}\right)^2 - \left(\Delta A_{zz}\right)^2 \tag{4.27}$$

To combine $A_{yy}$ and $A_{zz}$ they must both be evaluated at the same angle. For experimental reasons and because of poor planning, however, at some energies the $A_{yy}$

data were taken at angles several degrees away from the corresponding $A_{zz}$ measurements. To overcome this problem at angles for which there were $A_{yy}$ data but no $A_{zz}$ data, the $A_{zz}$ angular distributions were fit using a Legendre polynomial expansion, and the results were used in (4.26) and (4.27). The Legendre fitting code (LEGFIT) produces correlation coefficients for the correlations between expansion coefficients and these were included in the calculation of the errors on the results.

### 4.4 Other sources of error

Proper orientation of the spin axis of the beam by correct configuration of the Wien filter is very important for polarization measurements. This is especially true for the present work, since our polarimeter does not monitor the $\beta$ and $\phi$ for the beam, so that any errors in alignment go undetected. The question naturally arises, then: How sensitive are the measurements to misalignments of the polar and azimuthal angles?

#### *Spin axis misalignment*

The expression for the number of counts in a given detector is given in Appendix A as (A.8). If one computes the Taylor expansion of the trigonometric functions about $\beta$ and $\phi$ and inserts into (A.8) the result is, through terms linear in the angle changes $\Delta\beta$ and $\Delta\phi$,

$$\begin{aligned} I_0(\theta,\phi) = I_0(\theta)\Big\{1 &+ \frac{3}{2}P_z A_y[\sin\beta + \Delta\beta\cos\beta][\cos\phi - \Delta\phi\sin\phi] \\ &- P_{zz}A_{xz}[\sin\beta + \Delta\beta\cos\beta][\cos\beta - \Delta\beta\sin\beta][\sin\phi + \Delta\phi\cos\phi] \\ &- \frac{1}{4}P_{zz}(A_{xx} - A_{yy})[\sin^2\beta + 2\Delta\beta\cos\beta\sin\beta][\cos 2\phi - 2\Delta\phi\sin 2\phi] \\ &+ \frac{1}{4}P_{zz}A_{zz}\left[3(\cos^2\beta - 2\Delta\beta\cos\beta\sin\beta) - 1\right]\Big\} \end{aligned} \tag{4.28}$$

Now, consider $\beta = 0°$ and detectors at $\phi = 0°$, 180°, 270°, and 90°:

$$
\begin{aligned}
L_p &= I_L(\theta)\left\{1+\frac{3}{2}P_z^{(p)}A_y(\theta)\Delta\beta - P_{zz}^{(p)}A_{xz}(\theta)\Delta\beta + \frac{1}{2}P_{zz}^{(p)}A_{zz}(\theta)\right\} \\
R_p &= I_R(\theta)\left\{1-\frac{3}{2}P_z^{(p)}A_y(\theta)\Delta\beta + P_{zz}^{(p)}A_{xz}(\theta)\Delta\beta + \frac{1}{2}P_{zz}^{(p)}A_{zz}(\theta)\right\} \\
U_p &= I_U(\theta)\left\{1+\frac{3}{2}P_z^{(p)}A_y(\theta)\Delta\beta\Delta\phi + P_{zz}^{(p)}A_{xz}(\theta)\Delta\beta + \frac{1}{2}P_{zz}^{(p)}A_{zz}(\theta)\right\} \\
D_p &= I_D(\theta)\left\{1-\frac{3}{2}P_z^{(p)}A_y(\theta)\Delta\beta\Delta\phi - P_{zz}^{(p)}A_{xz}(\theta)\Delta\beta + \frac{1}{2}P_{zz}^{(p)}A_{zz}(\theta)\right\}
\end{aligned}
\tag{4.29}
$$

In this case the sums l + r and u + d are both free of first-order errors in $\beta$ and $\phi$, so the sum S (3.4) and the ratio R (3.6) will both be free of such errors, as will the observables constructed from them, $P_{zz}$ and $A_{zz}$. For $\beta_0 = 90°$, the detector count expressions are

$$
\begin{aligned}
L_p &= I_L(\theta)\left\{1+\frac{3}{2}P_z^{(p)}A_y(\theta) + P_{zz}^{(p)}A_{xz}(\theta)\Delta\beta\Delta\phi - \frac{1}{2}P_{zz}^{(p)}A_{yy}(\theta)\right\} \\
R_p &= I_R(\theta)\left\{1-\frac{3}{2}P_z^{(p)}A_y(\theta) - P_{zz}^{(p)}A_{xz}(\theta)\Delta\beta\Delta\phi - \frac{1}{2}P_{zz}^{(p)}A_{yy}(\theta)\right\} \\
U_p &= I_U(\theta)\left\{1+\frac{3}{2}P_z^{(p)}A_y(\theta)\Delta\phi - P_{zz}^{(p)}A_{xz}(\theta)\Delta\beta - \frac{1}{2}P_{zz}^{(p)}A_{xx}(\theta)\right\} \\
D_p &= I_D(\theta)\left\{1+\frac{3}{2}P_z^{(p)}A_y(\theta)\Delta\phi + P_{zz}^{(p)}A_{xz}(\theta)\Delta\beta - \frac{1}{2}P_{zz}^{(p)}A_{xx}(\theta)\right\}
\end{aligned}
\tag{4.30}
$$

so that, again, $P_{zz}$ and $A_{yy}$ are free of first-order errors. Therefore, the present measurements are free of first-order spin alignment errors.

It is instructive to consider the case of measuring $A_{xz}$. The optimal value of $\beta$ for this case is 45° with the spin axis in the scattering plane. To isolate $A_{xz}$ only one polarized state and one unpolarized state are needed. If there are no alignment errors, the chamber detector counts (which are "up" and "down" detectors in this configuration) are combined as

$$
D = u - d = \frac{1}{2}P_{zz}A_{xz} \tag{4.31}
$$

and if the $A_{xx}$ of the monitor is known, the monitor counts can be combined to yield:

$$D^{mon} = (l+r)-(u+d) = -P_{zz}A_{xx} \tag{4.32}$$

The general first-order expressions for the detector counts for the $A_{xz}$ measurement are

$$\begin{aligned}
L_p &= I_L\left\{1+\frac{3}{2\sqrt{2}}P_z^{(p)}A_y(1+\Delta\beta)-\frac{1}{2}P_{zz}^{(p)}A_{xz}(\Delta\phi-\Delta\phi\Delta\beta)\right. \\
&\qquad \left.-\frac{1}{4}P_{zz}^{(p)}\left(A_{xx}-A_{yy}\right)\left(\frac{1}{2}+\Delta\beta\right)+\frac{1}{4}P_{zz}^{(p)}A_{zz}\left(\frac{1}{2}-3\Delta\beta\right)\right\} \\
R_p &= I_R\left\{1-\frac{3}{2\sqrt{2}}P_z^{(p)}A_y(1+\Delta\beta)+\frac{1}{2}P_{zz}^{(p)}A_{xz}(\Delta\phi-\Delta\phi\Delta\beta)\right. \\
&\qquad \left.-\frac{1}{4}P_{zz}^{(p)}\left(A_{xx}-A_{yy}\right)\left(\frac{1}{2}+\Delta\beta\right)+\frac{1}{4}P_{zz}^{(p)}A_{zz}\left(\frac{1}{2}-3\Delta\beta\right)\right\} \\
U_p &= I_U\left\{1+\frac{3}{2\sqrt{2}}P_z^{(p)}A_y(\Delta\phi+\Delta\phi\Delta\beta)+\frac{1}{2}P_{zz}^{(p)}A_{xz}(1-\Delta\beta)\right. \\
&\qquad \left.+\frac{1}{4}P_{zz}^{(p)}\left(A_{xx}-A_{yy}\right)\left(\frac{1}{2}+\Delta\beta\right)-\frac{1}{4}P_{zz}^{(p)}A_{zz}\left(\frac{1}{2}-3\Delta\beta\right)\right\} \\
D_p &= I_D\left\{1-\frac{3}{2\sqrt{2}}P_z^{(p)}A_y(\Delta\phi+\Delta\phi\Delta\beta)-\frac{1}{2}P_{zz}^{(p)}A_{xz}(1-\Delta\beta)\right. \\
&\qquad \left.+\frac{1}{4}P_{zz}^{(p)}\left(A_{xx}-A_{yy}\right)\left(\frac{1}{2}+\Delta\beta\right)-\frac{1}{4}P_{zz}^{(p)}A_{zz}\left(\frac{1}{2}-3\Delta\beta\right)\right\}
\end{aligned} \tag{4.33}$$

so that both the tensor polarization and the $A_{xz}$ are sensitive, in general, to first order errors in $\beta$ and $\phi$. For example, if $A_{xx} \approx A_{yy}$ for the monitor, as is true for our 10° D(d,p)$^3$H polarimeter, even if $\Delta\phi = 0$, and $\Delta\beta = 1°$, the beam polarization measurement would be off by 11%! This error vanishes if the monitor analyzing powers satisfy $A_{xx} \approx -2\,A_{yy}$ (this is the case for D(d,p)$^3$H near 90°), and it can be reduced by using a two-detector monitor with counts combined as in (4.31). The determination of $A_{xz}$ using our data reduction method requires careful thought and precise knowledge of the angles $\beta$ and $\phi$ as determined from the Wien filter calibration.

## V. Results and comparison with previous data: Judges

Our precise tensor analyzing power data are presented below and compared with other recent data.

### 5.1 $A_{zz}$ and $(A_{xx}-A_{yy})$ for $D(d,p)^3H$ and $D(d,n)^3He$

The angular distributions for the tensor analyzing powers $A_{zz}$ and $(A_{xx}-A_{yy})$ are presented in graphical form in Figures 5-1 to 5-4 along with the results of Legendre function expansions of these data. For both decay branches, as the reaction energy increases the value of $A_{zz}$ near 180° becomes less negative, while that near 0° becomes more negative. The observable $(A_{xx}-A_{yy})$ near 90° becomes less negative with increasing energy. The Legendre coefficients were obtained by simultaneously fitting each of our tensor analyzing power distributions and the unpolarized cross section data from [Bro90]:

$$\sigma_0(\theta) = \sum_{L=0,2,4} A_L P_L(\cos\theta) \tag{5.1}$$

$$A_{zz}(\theta) = \frac{1}{\sigma_0(\theta)} \sum_{L=0}^{L_{max}} C_L P_L(\cos\theta) \tag{5.2}$$

$$A_{xx}(\theta) - A_{yy}(\theta) = \frac{1}{\sigma_0(\theta)} \sum_{L=2}^{L_{max}} E_L P_L^2(\cos\theta) \tag{5.3}$$

In (5.3) $P_L^2(\cos\theta)$ is the associated Legendre function. The expansion coefficients for the Legendre fits are given in Tables 5.1 - 5.4.

The highest order Legendre function (with $L=L_{max}$) included in the fit for each of the three observables was set the same for all energies, so that at the lowest energies

there are expansion coefficients which are consistent with zero. The maximum L available in the weighted fitting code was $L_{max} = 4$. To test whether this $L_{max}$ was large enough to adequately describe the data, unweighted linear regression was performed on our 80-keV $A_{zz}$ data using *Mathematica* with $L_{max}$ increased from 3 to 8. The actual minimum value of $\chi^2$ per degree of freedom occurred for $L_{max} = 5$, but the difference from $L_{max} = 4$ was only 2%, and so the existing code was used.

As an aside, according to Yang's Theorem [Yan48], ignoring spins, the $L_{max}$ in the expansion (5.1) is less than or equal to *twice* the maximum L-value for a scattering amplitude. Schematically,

$$\sigma_0(\theta) = \left| \sum_{\ell=0}^{\ell_{max}} \alpha_\ell P_\ell(\cos\theta) \right|^2 = \sum_{\ell,\ell'} \alpha_\ell \alpha^*_{\ell'} P_\ell(\cos\theta) P_{\ell'}(\cos\theta) = \sum_{L=0}^{L_{max}} A_L P_L(\cos\theta) \qquad (5.4)$$

where

$$A_L \propto \alpha_\ell \alpha^*_{\ell'} \; C^2(\ell \ell' L, 000) \qquad (5.5)$$

and the triangle rule on the Clebsch-Gordan coefficient gives $L \le \ell + \ell' \le 2\ell_{max}$.

Even though the fits appear to give a good representation of the data, the values of $\chi^2$ per degree of freedom for these fits are poor at the higher energies, particularly for the $D(d,n)^3He$ reaction. Assuming a reasonable algorithm for producing the best fit, a large $\chi^2$ value can result from underestimation of the standard deviations of the data, abnormally large contributions from several points which are far from the fit ("outliers"), or a combination of these two causes. To investigate our situation, the data from the 80 keV $A_{zz}$ measurements were re-examined in several different ways. First, the contribution of each data point to the total $\chi^2$ was calculated for each of the three charged-particle groups. In each case, there were several points that were more than three standard deviations away from the fitted value. The spectra for all the runs used in the determination of these outliers were checked for poorly selected gates or poorly determined backgrounds which might produce systematic errors. With some modifications to the particle gates and background gates the spectra were summed and

the data reduction performed again. This did not improve considerably the $\chi^2$ values which resulted for the three particle groups, because in general the analyzing powers which resulted were within one standard deviation of the original values. The $\chi^2$ value with the outliers actually removed from the data was also calculated for the three charged-particle groups. The values of $\chi^2$ per degree of freedom which resulted were reduced to about 2.5. However, data cannot be discarded without some compelling reason, and so the outliers are retained in the present data set.

We could think of only a few sources of error which were not included in the error estimation, such as the beam current integration (BCI) error. Since our data depend only on relative BCI determinations, and the manufacturer of our integrator claims that the reproducibility of the device is 0.001% [Bro00], such errors are safely neglected. As a final test, the data reduction was performed with the correlation coefficients set to zero. Because the standard deviations increase by removing the correlations, the resulting $\chi^2$ values were less that 60% of the original values, with values for $\chi^2$ per degree of freedom which were less than two.

This brings to mind the question of whether it is appropriate to include correlated errors in the error estimations for our data (see section 4.3.1). The decision to include them is dictated by the empirical evidence for nonvanishing correlation coefficients. The correlations are calculated for detector responses for the different states, corrected for differences in dead time, BCI, and target thickness. For each run, the correction for the target thickness is performed by dividing the detector responses by the sum of the monitor counts in the unpolarized state, corrected for dead time and BCI. This procedure should remove differences between runs which might mimic correlations which are not there. Even so, positive and negative correlations between counts persist with values larger than $\pm 0.5$, and such correlations cannot be ignored in the error estimation.

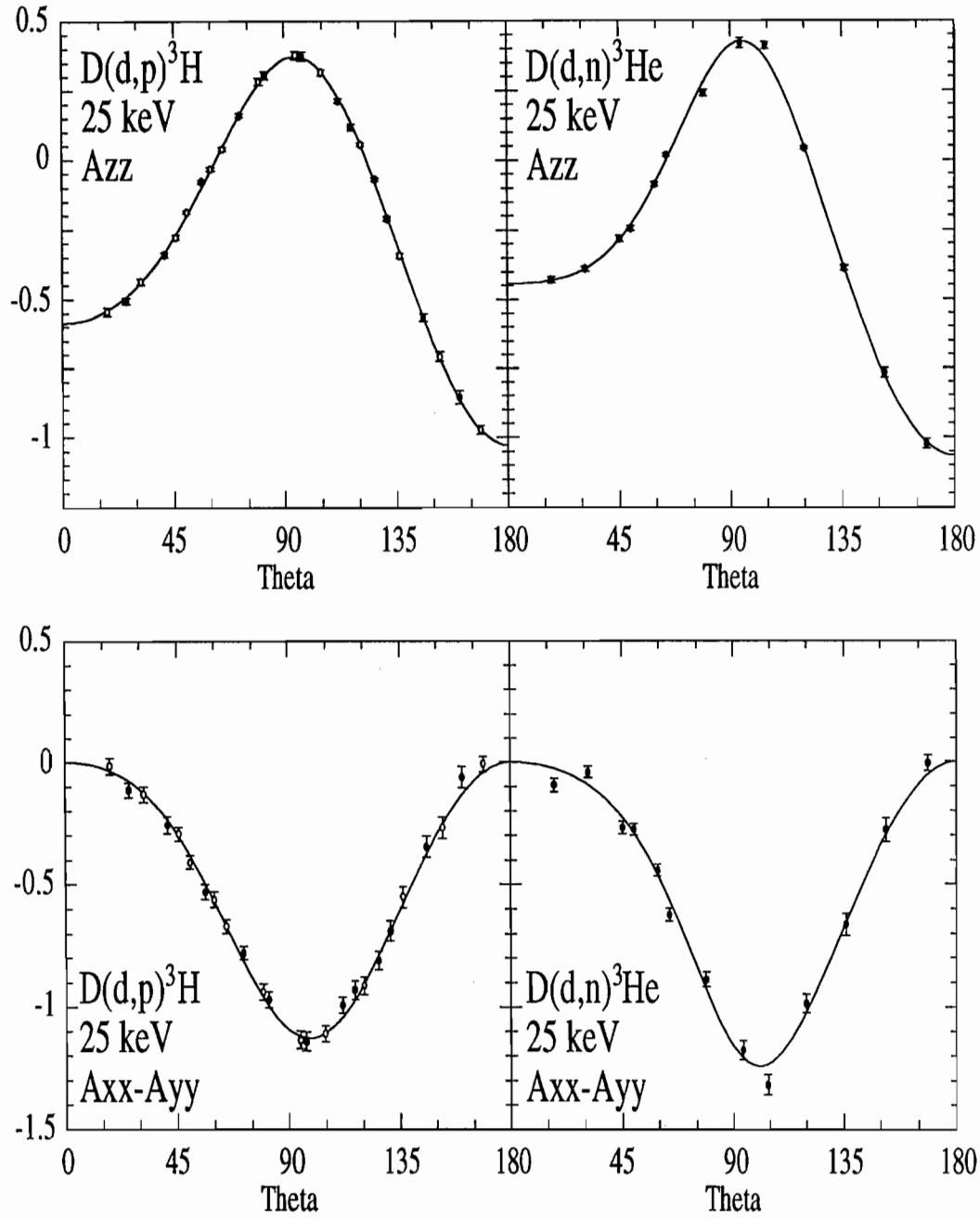


Figure 5-1. Our determinations of $A_{zz}$ and $A_{xx}$-$A_{yy}$ for D(d,p)$^3$H and D(d,n)$^3$He at $E_d$ = 25 keV ($E_R$ = 20.9 keV). The solid lines are the results of Legendre function fits.

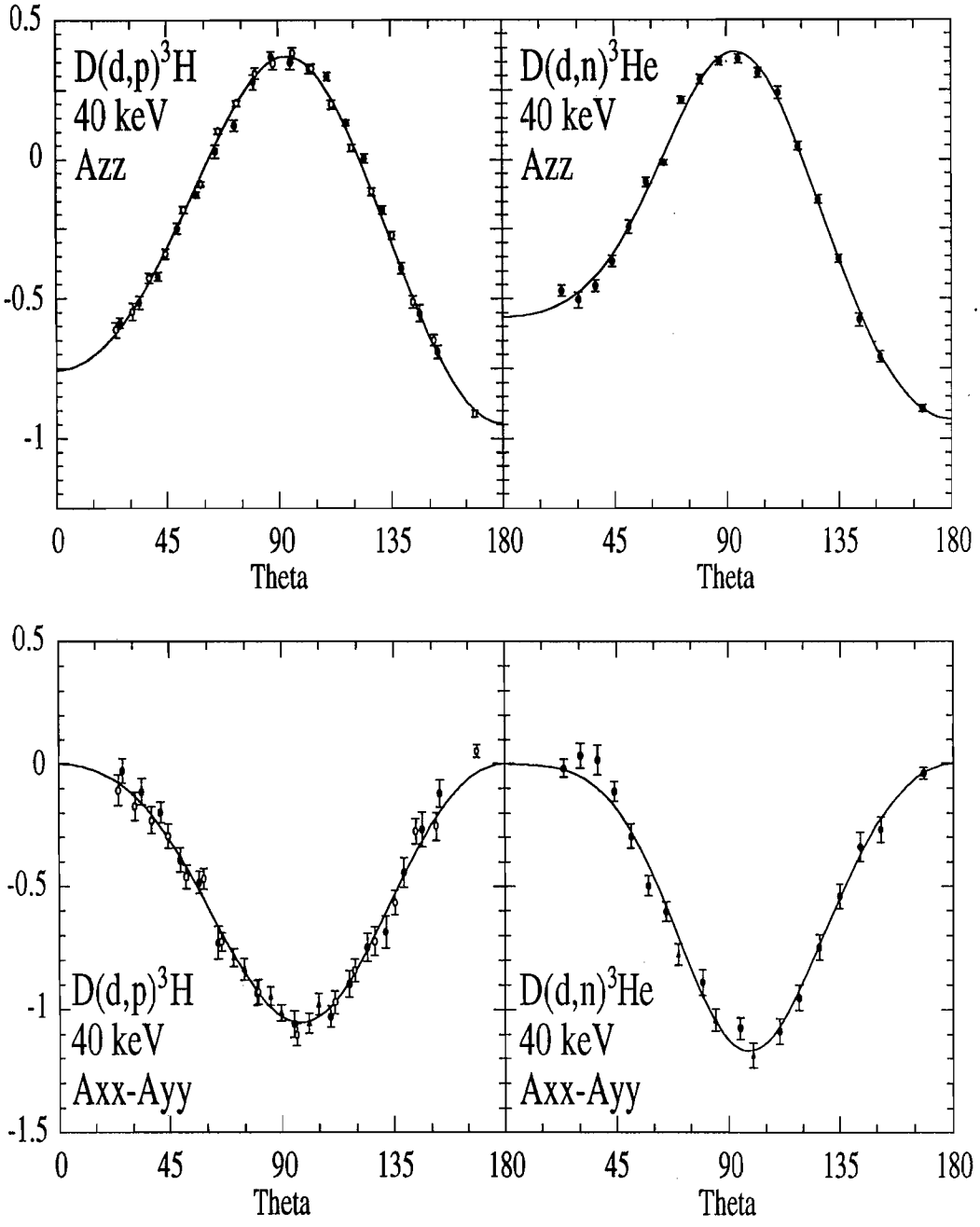


Figure 5-2. Our determinations of $A_{zz}$ and $A_{xx}$-$A_{yy}$ for D(d,p)$^3$H and D(d,n)$^3$He at $E_d$ = 40 keV ($E_R$ = 38.7 keV for $A_{zz}$ and 38.4 keV for $A_{xx}$-$A_{yy}$ ). The solid lines are the results of Legendre function fits.

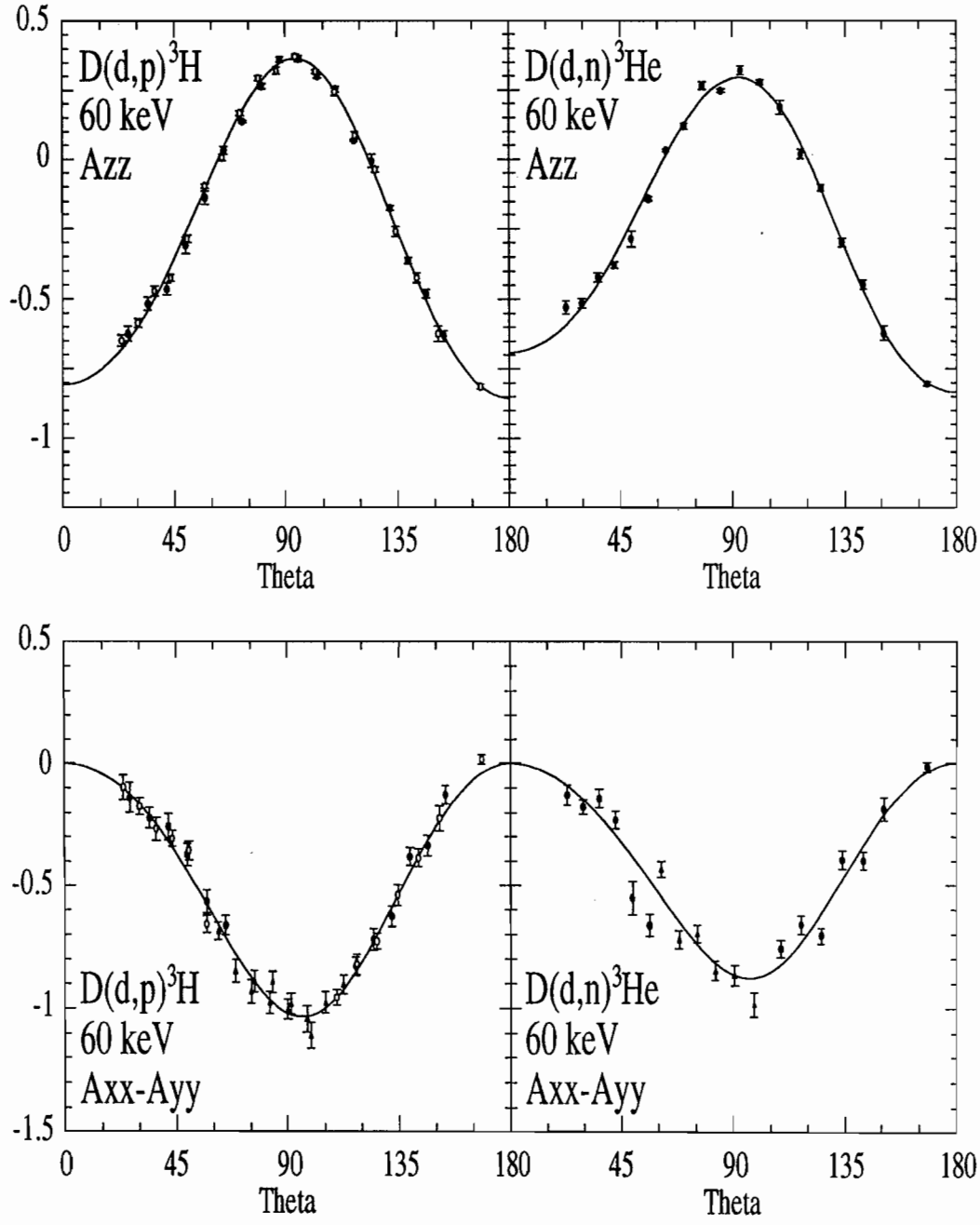


Figure 5-3. Our determinations of $A_{zz}$ and $A_{xx}$-$A_{yy}$ for D(d,p)$^3$H and D(d,n)$^3$He at $E_d$ = 60 keV ($E_R$ = 55.0 keV $A_{zz}$ and 56.2 keV for$A_{xx}$-$A_{yy}$ ). The solid lines are the results of Legendre function fits.

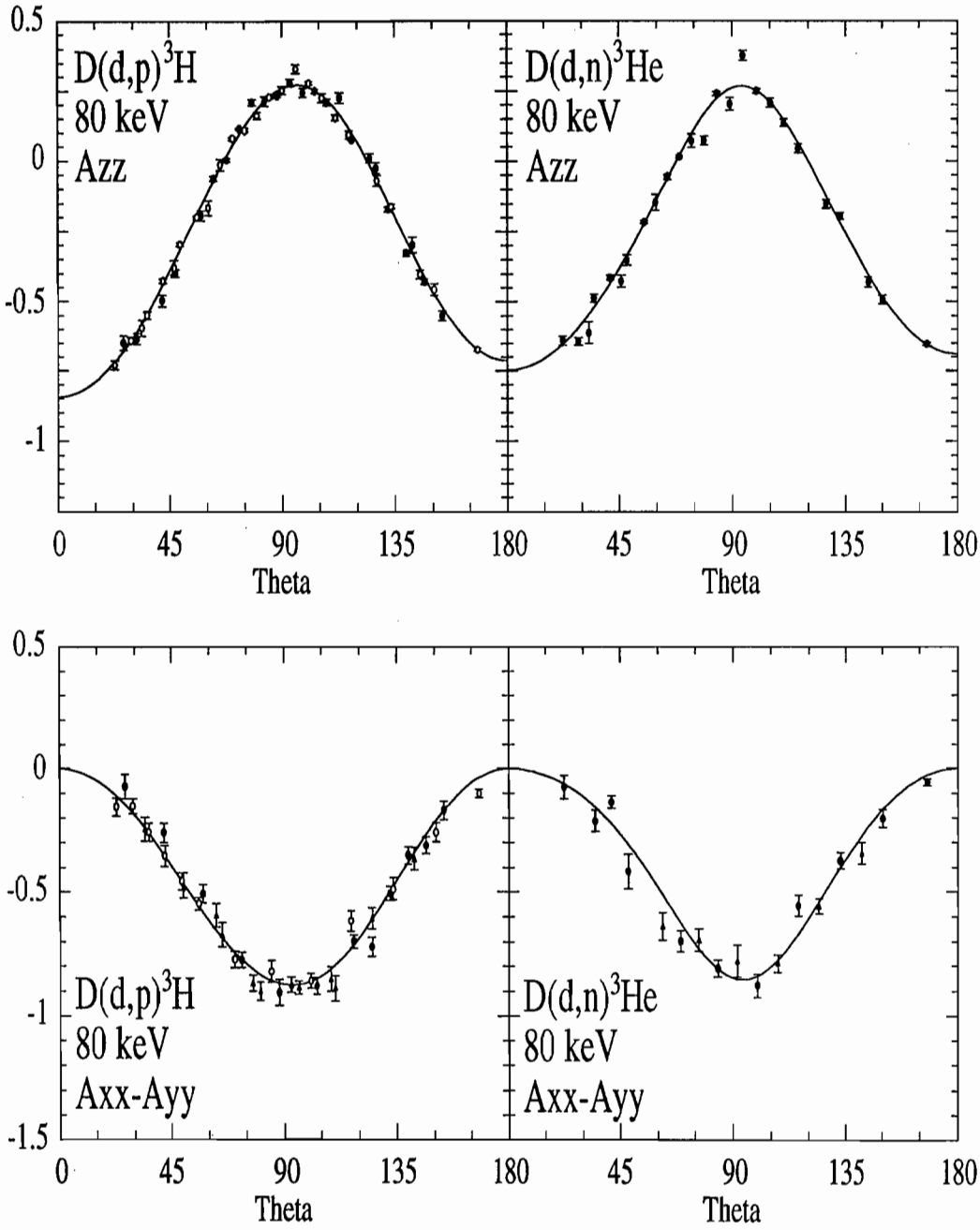


Figure 5-4. Our determinations of $A_{zz}$ and $A_{xx}$-$A_{yy}$ for D(d,p)$^3$H and D(d,n)$^3$He at $E_d$ = 80 keV ($E_R$ = 75.1 keV $A_{zz}$ and 75.7 keV for$A_{xx}$-$A_{yy}$ ). The solid lines are the results of Legendre function fits.

Table 5.1. Legendre polynomial expansion coefficients for the triton data for $A_{zz}$ and $D(d,p)^3H$. Reaction energies in the laboratory frame, $E_R$, are in keV.

| $E_R$ | 20.9 | 38.7 | 55.0 | 75.1 |
|---|---|---|---|---|
| $A_0$ | 0.0214±.0006 | 0.2100±.0017 | 0.524±.0035 | 0.866±0.0048 |
| $A_2$ | 0.0023±.0012 | 0.0438±.0044 | 0.124±.0088 | 0.256±0.0121 |
| $A_4$ | -0.00043±.0006 | 0.00055±.0045 | 0.00851±.0094 | 0.0212±0.012 |
| $C_0$ | -0.0017±.00021 | -0.0231±.0011 | -0.0597±.0021 | -0.127±0.0025 |
| $C_1$ | 0.0012±.00014 | 0.0020±.0017 | -0.0264±.0033 | -0.118±0.0039 |
| $C_2$ | -0.0176±.00059 | -0.188±.0032 | -0.468±.0063 | -0.693±0.0074 |
| $C_3$ | 0.00387±.00020 | 0.0218±.0024 | 0.0417±.0042 | 0.043±0.0052 |
| $C_4$ | 0.00056±.00057 | -0.0054±.0035 | -0.019±.0062 | -0.071±0.0076 |
| $\frac{\chi^2}{d.f.}$ | 0.83 | 2.0 | 3.1 | 4.0 |

Table 5.2. Legendre polynomial expansion coefficients for the triton data for $A_{xx}$-$A_{yy}$ and $D(d,p)^3H$. Reaction energies in the laboratory frame, $E_R$, are in keV.

| $E_R$ | 20.9 | 38.4 | 56.2 | 75.7 |
|---|---|---|---|---|
| $A_0$ | 0.0215±.00059 | 0.211±.0017 | 0.524±.0035 | 0.868±.0048 |
| $A_2$ | 0.00159±.0015 | 0.0474±.0044 | 0.126±.0089 | 0.257±.012 |
| $A_4$ | -0.00018±.0014 | 0.0103±.0052 | 0.0105±.0105 | 0.0309±.014 |
| $E_2$ | -0.0145±.00057 | -0.129±.0024 | -0.320±.0054 | -0.460±.0075 |
| $E_3$ | 0.0013±.00011 | 0.00935±.0011 | 0.0168±.0022 | 0.0103±.0034 |
| $E_4$ | 0.000215±.0001 | 0.00085±.00079 | -0.00164±.0016 | -0.0094±.0025 |
| $\frac{\chi^2}{d.f.}$ | 0.48 | 1.3 | 1.7 | 2.4 |

Table 5.3. Legendre polynomial expansion coefficients for $A_{zz}$ and D(d,n)$^3$He. Reaction energies in the laboratory frame, $E_R$, are in keV.

| $E_R$ | 20.9 | 38.7 | 55.0 | 75.1 |
|---|---|---|---|---|
| $A_0$ | 0.0217±.0009 | 0.213±.0024 | 0.525±.0054 | 0.902±0.0068 |
| $A_2$ | 0.0070±.0014 | 0.0657±.0063 | 0.238±.0148 | 0.384±0.019 |
| $A_4$ | -0.00037±.0006 | 0.00209±.0055 | 0.0471±.0124 | -0.0151±0.017 |
| $C_0$ | -0.0025±.00024 | -0.0284±.0013 | -0.0893±.0029 | -0.159±0.0036 |
| $C_1$ | 0.0028±.00022 | 0.0140±.0018 | 0.0165±.0038 | -0.081±0.0051 |
| $C_2$ | -0.0195±.00086 | -0.189±.0040 | -0.490±.0088 | -0.715±0.011 |
| $C_3$ | 0.00604±.00031 | 0.0373±.0026 | 0.0441±.0049 | 0.043±0.0060 |
| $C_4$ | 0.00065±.00065 | -0.0073±.0042 | -0.063±.0079 | -0.041±0.011 |
| $\frac{\chi^2}{d.f.}$ | 3.7 | 3.4 | 7.0 | 6.1 |

Table 5.4. Legendre polynomial expansion coefficients for $A_{xx}$-$A_{yy}$ and D(d,n)$^3$He. Reaction energies in the laboratory frame, $E_R$, are in keV.

| $E_R$ | 20.9 | 38.4 | 56.2 | 75.7 |
|---|---|---|---|---|
| $A_0$ | 0.0217±.00087 | 0.212±.0025 | 0.551±.0055 | 0.906±.0069 |
| $A_2$ | 0.00683±.0020 | 0.0651±.0065 | 0.228±.015 | 0.387±.019 |
| $A_4$ | -0.00124±.00152 | -0.0017±.0069 | 0.0088±.015 | 0.011±.019 |
| $E_2$ | -0.0139±.00077 | -0.128±.0029 | -0.271±.0055 | -0.409±.0088 |
| $E_3$ | 0.00205±.00014 | 0.0156±.0012 | 0.0149±.0022 | 0.0192±.0042 |
| $E_4$ | -0.00007±.00012 | 0.0025±.00085 | -0.0068±.0017 | -0.0019±.0028 |
| $\frac{\chi^2}{d.f.}$ | 2.4 | 1.5 | 4.4 | 2.8 |

### 5.1.1 $D(d,p)^3H$ vs $D(d,n)^3He$

In [Bro90] the authors note that in their energy range (20 to 117 keV) the angular anisotropy in their differential cross section measurements is larger for the $D(d,n)^3He$ reaction than for the $D(d,p)^3H$. They also note that the integrated cross sections are larger for $D(d,n)^3He$ than for $D(d,p)^3H$.

To compare the two reactions at each energy using our data, the angular distributions of the Legendre function expansions with coefficients from Tables 5.1-5.4 are plotted for each observable (Figure 5-5). It is easier to see differences between the reactions if the Legendre function fits, rather than the data themselves, are plotted. (Note that the scales are different for the two tensor analyzing powers.) There are slight differences between the two reactions at forward angles for $A_{zz}$ and near 90° for $A_{xx}$-$A_{yy}$. For the $A_{zz}$ distributions at the lowest energies, the angle asymmetry between 0° and 180° is larger for $D(d,n)^3He$ than for $D(d,p)^3H$. As the energy decreases, the minima in the $A_{xx}$-$A_{yy}$ distributions shift to angles larger than 90°. As discussed in section 1.3.2, such angle asymmetries are evidence of the presence of entrance quintet S-states. In general, however, the analyzing powers for the two reactions are remarkably similar. The degree of similarity is striking when compared to the differences in the unpolarized differential cross sections from the fits to the data given in [Bro90] (Figure 5.6). These show that, in general, the P-waves and D-waves exert more influence on the $D(d,n)^3He$ branch than on the $D(d,p)^3H$ branch, as indicated by the higher 0°-to-90° asymmetry for this branch.

Obviously, the interaction in the region beyond the range of the nuclear force is quite different for the $D(d,p)^3H$ reaction, which emits two charged particles, and the $D(d,n)^3He$ reaction. The long-range Coulomb repulsion certainly alters the observables, especially at forward angles. An additional mechanism proposed to explain the differences between the two reactions for cross section data is isospin mixing by internal Coulomb interactions [Ser72]. An R-matrix treatment has indicated

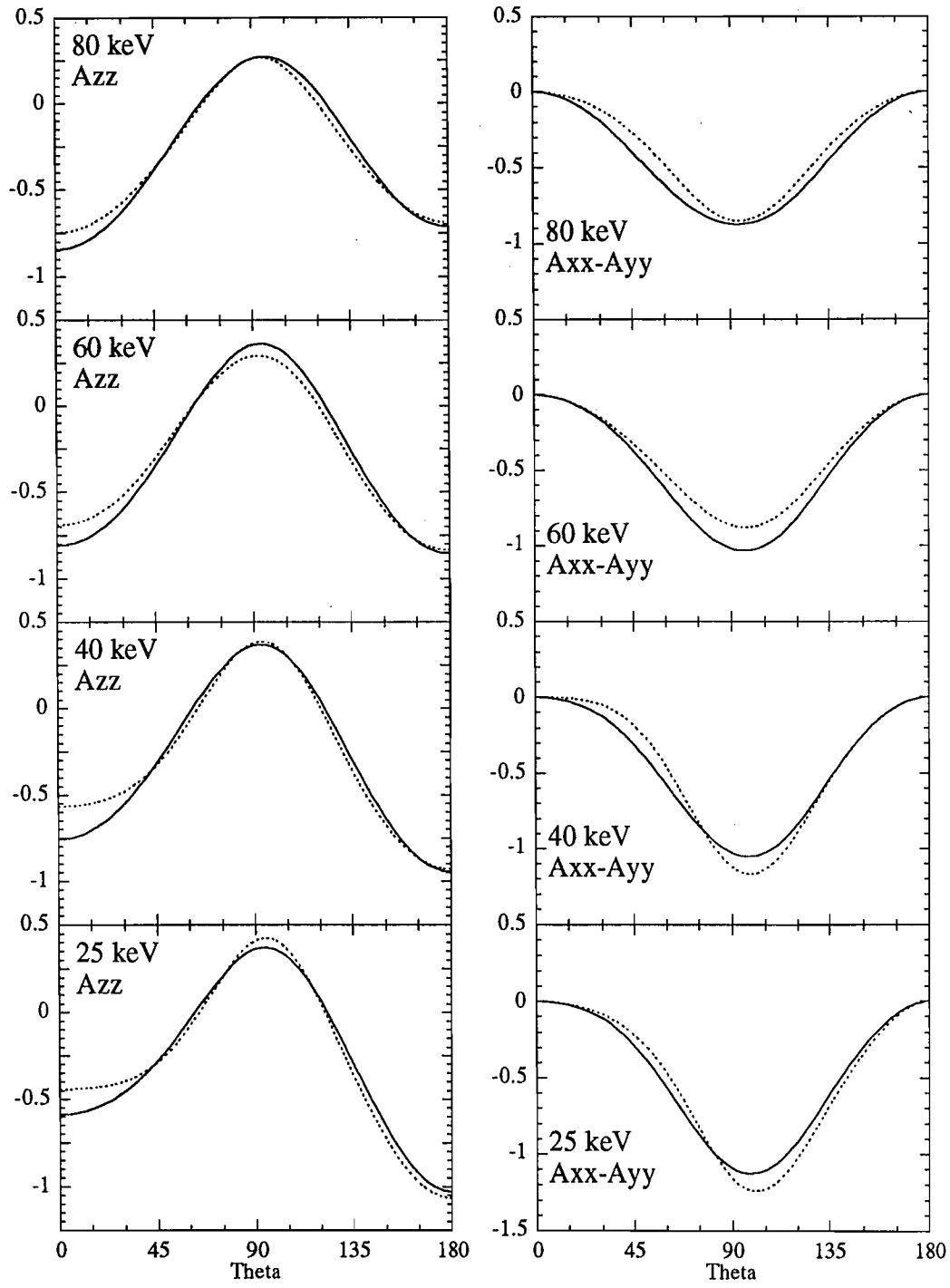


Figure 5-5. Comparisons of the Legendre function fits to the $A_{zz}$ and $A_{xx}$-$A_{yy}$ distributions for D(d,p)$^3$H (solid lines) and D(d,n)$^3$He (dotted lines).

that very small isospin-mixing amplitudes are sufficient to produce the (d,p)-(d,n) differences ([Hal80], as described in section 6.1).

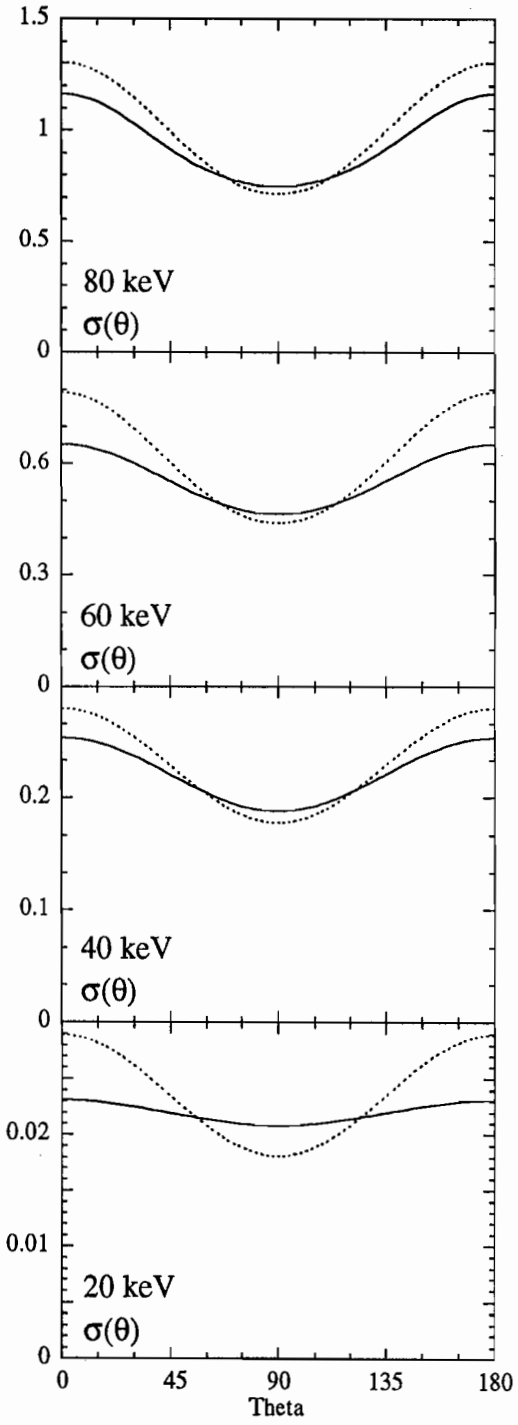


Figure 5-6. Comparisons of the Legendre polynomial fits to the differential cross section distributions for $D(d,p)^3H$ (solid lines) and $D(d,n)^3He$ (dotted lines) from the data of [Bro90].

## 5.2. Comparison with data from other laboratories

Tagishi et al. [Tag92] measured a complete set of analyzing powers at 30, 50, 70, and 90 keV for the $D(d,p)^3H$ reaction only. Their $T_{20}$ distributions span an angular range in the laboratory of 0° to about 177° with measurements every 10°, and the $T_{22}$ data cover a range of 0° to 160° by 10° steps. For comparison, protons and tritons are collected every 7.5° from 10° to 152.5° for our 40, 60, and 80 keV measurements. Our 25-keV measurements covered 10° to 160° in 15° increments.

Our data are compared in Figure 5.7 with the Legendre fits from [Tag92] (converted to Cartesian tensors) for D(d,p)$^3$H. The plots show our results bracketed by the [Tag92] fits at the nearest higher and lower energies using solid and dashed lines, respectively. Our polarimeter was calibrated using their data at 10°, and consistency at forward angles is not surprising. It is satisfying that the agreement extends throughout the angular range for most of the observables. The energies listed on the plots are the bombarding energies, and since the targets in [Tag92] were generally of the same thickness as our targets, such a comparison of the two data sets is reasonable. For $A_{xx}$-$A_{yy}$ at $E_d$ = 25 keV, however, the 30 keV fit to the data of [Tag92] lie below the 25 keV data, which is *not* expected.

The angular distributions of $A_{zz}$ and $A_{xx}$-$A_{yy}$ at 28 keV from the Köln group [Bec92] cover 24° to 160° for D(d,n)$^3$He in about 13° steps. Their D(d,p)$^3$H angular distributions range from 18° to 160° with about twice as many data points, resulting from including the proton and triton groups. The Köln group also measured $A_y$ and $A_{xz}$.

To compare with the data of [Bec92], our 25-keV ($E_R$ = 21 keV) data are plotted in Figure 5.8 along with the fits to the [Bec92] data ($E_R$ = 28 keV) for both reactions. The biggest differences in the two data sets occur in the $A_{xx}$-$A_{yy}$ distributions. Whereas the data from [Bec92] indicate a smaller magnitude for the (d,n) branch relative to the (d,p) branch near 90°, our data show the two branches to be very similar, with (d,n) slightly larger. Quantitatively, from the Legendre function fits of [Bec92] the ratio of $[A_{xx}(90°)\text{-}A_{yy}(90°)]_{(d,n)}$ to $[A_{xx}(90°)\text{-}A_{yy}(90°)]_{(d,p)}$ is about 0.76. For our data this ratio is 1.06, and we see similar results at 40 keV. It is difficult to explain this discrepancy, particularly since in both experiments the two branches were collected simultaneously, so that any normalization error cannot account for these results.

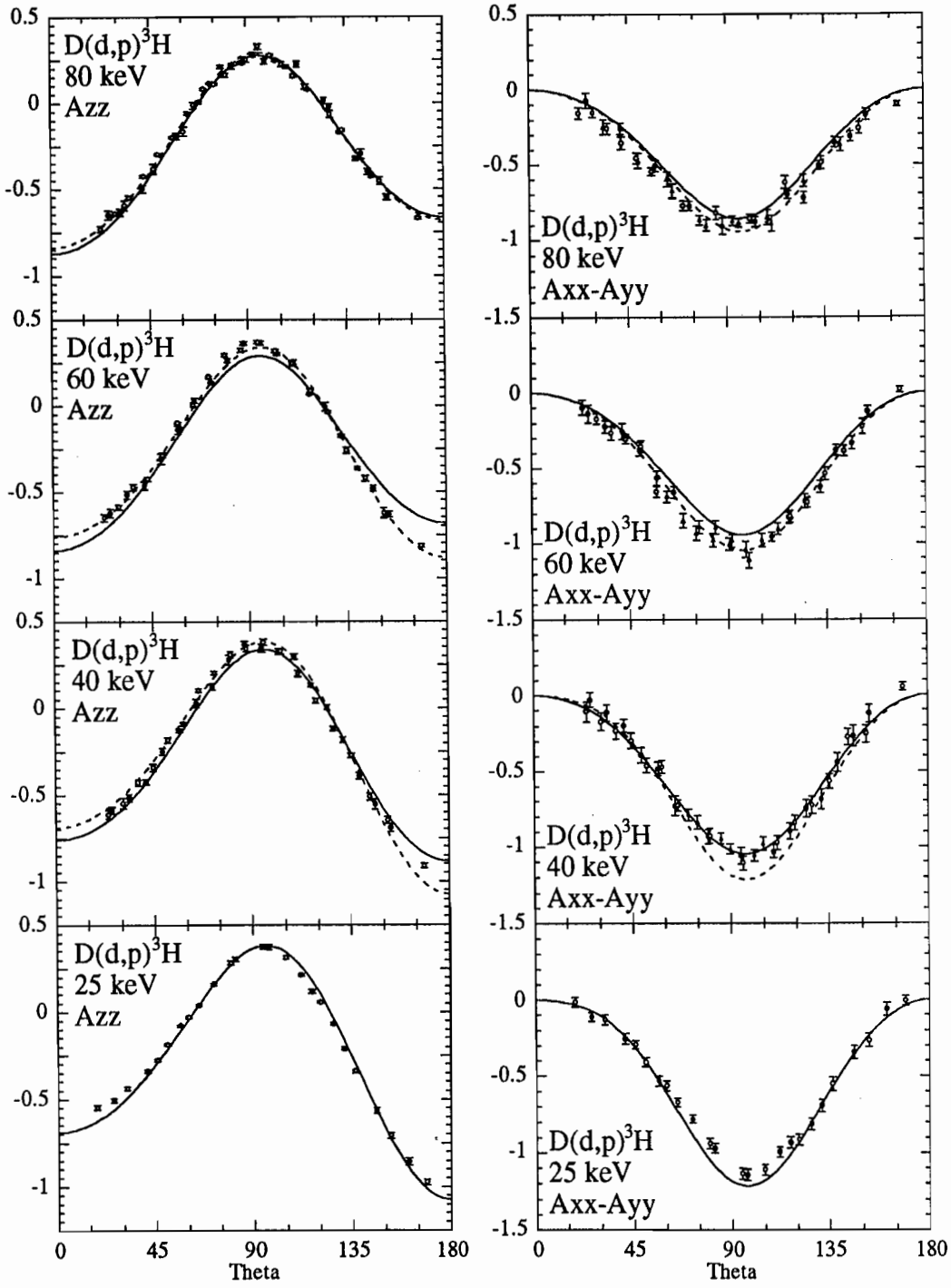


Figure 5-7. Our $A_{zz}$ and $A_{xx}$-$A_{yy}$ distributions are compared to the Legendre function fits to the data of [Tag92]. For the 40, 60, and 80 keV graphs, the solid lines are the fits to data from [Tag92] for bombarding energies 10 keV higher than ours and the dashed lines are the fits to data from [Tag92] for bomarding energies 10 keV lower than ours. For the 25 keV plots, the solid lines are the fits to data from [Tag92] at $E_d$ = 30 keV.

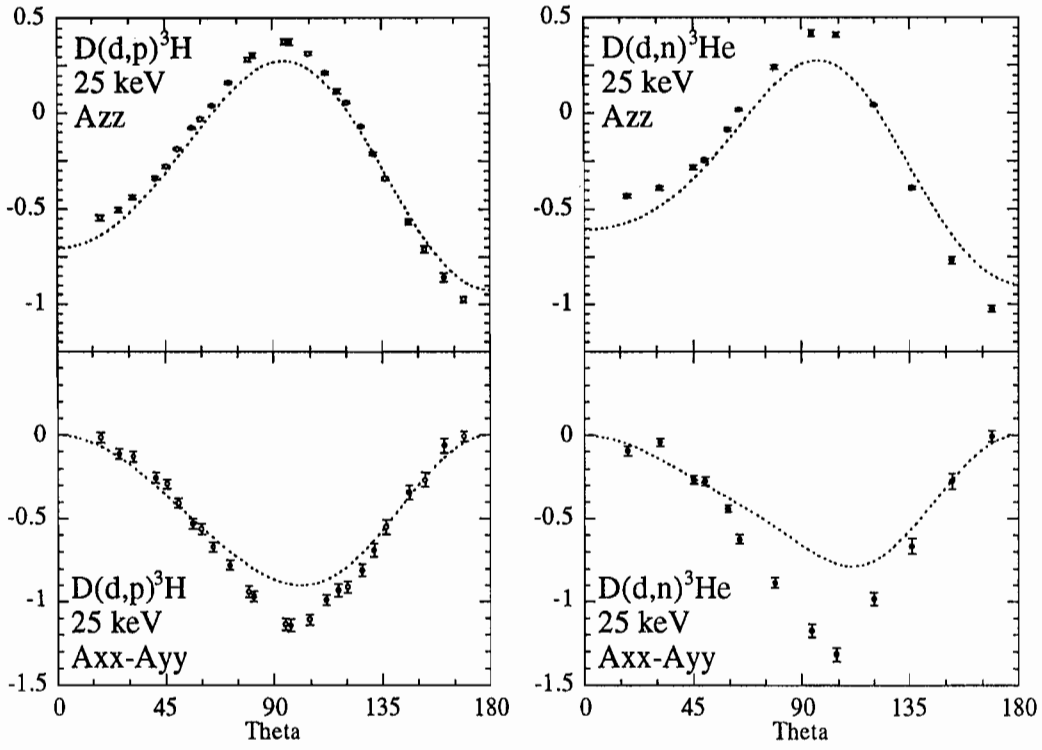


Figure 5-8. Our $A_{zz}$ and $A_{xx}$-$A_{yy}$ distributions at 25 keV ($E_R$ = 20.9 keV) are compared to the Legendre function fits from [Bec92] at $E_R$ = 28 keV (dashed lines).

In section 6.1 a very good agreement is obtained between our data and a global R-matrix prediction which does not include either our data or the data of [Bec92] or [Tag92] (figures 6-3 through 6-6). For the analyzing powers, the R-matrix analysis indicates little difference between the two reactions. This is also true of the original transition matrix element fit from the Köln group [Lem90], which also did not include our data or the data of [Bec92] or [Tag92]. The fit of [Lem90] indicated a slightly *larger* magnitude for $A_{xx}$-$A_{yy}$ at 90° than the R-matrix for both reactions. The data of [Bec92] were included in their new version of the matrix element fit. With these data included, the magnitude of the $A_{xx}$-$A_{yy}$ value calculated at 90° by the matrix element fit

became *smaller* than that predicted by the R-matrix, but not as small as the Legendre function fit to the data shown in figure 5.8. Of the four analyzing power distributions shown for each reaction in [Bec92], the $A_{xx}$-$A_{yy}$ plots have the largest discrepancies between the data and the transition matrix element fits which include them.

## VI. Theoretical Analyses: Revelations

Various analysis methods can be applied to these data. We now summarize these analysis methods.

In a *dynamical* approach, such as that of the resonating group model, the fits between the data and calculations are used to evaluate the potentials and wavefunctions included in the model. Any discrepancies are an indication that the model requires refinement.

In a *reaction parametrization* approach, parameters of some type are varied to obtain the best fit to the data for the reaction of interest and, hopefully, some deeper understanding. For example, a Legendre function expansion provides an indication of the partial waves which contribute in a reaction. In the invariant amplitude method of Tanifuji [Tan92], the transition matrix elements are parametrized in terms of angle-dependent invariant amplitudes, which are further parametrized in terms of coefficients of Legendre function expansions and overall normalizations. These are then varied to give the best fit to the data. Using such an approach to fit the data of [Tag92], Tanifuji concluded that the main contributions to the analyzing powers came from S-wave to S-wave transitions, P-wave to P-wave transitions, and S-wave to D-wave transitions [Tan92]. In the Köln transition matrix element analysis [Lem90] the energy dependence of the transition matrix elements is assumed to be entirely due to the entrance channel penetrability. The absolute values and phases of the energy independent parts of the matrix elements are varied to fit the data for the $D(d,p)^3H$ and $D(d,n)^3He$ reactions below 500 keV. The main conclusion of [Lem90] is that, for both reactions, the transitions from quintet S-states are of the same order of magnitude

as transitions from singlet S-states, and, therefore, these reactions would not be suppressed in a polarized fusion reactor (see section 1.2.2). In parametrizations of this type, specific questions may be addressed and predictions of unmeasured observables may be made *only* for the *reaction under study*.

We chose to analyze our data using the multichannel R-matrix approach from resonance theory, which is a *global parametrization* method. The R-matrix parameters are varied to obtain simultaneously the best fit to all available data for *all possible* two-body channels of a given composite nucleus. Information on the level scheme for the composite nucleus can be extracted, as well as information on the reaction, using the R-matrix analysis. A transition matrix element fit is a small subset of the R-matrix parametrization. In terms of computational complexity, we estimate that the LANL R-matrix analysis of the A = 4 system requires several orders of magnitude more computing time than a Legendre fit to one of the decay branches at low energies.

The R-matrix parametrization of few-nucleon systems has been an ongoing project in the Nuclear Theory and Applications Group (T-2) of the Theoretical Division of Los Alamos National Laboratory (LANL) since the early 1970's. The analysis of the four-nucleon $^4$He system includes data on $^3$H(p,p)$^3$H, $^3$H(p,n)$^3$He (and its inverse reaction), $^3$He(n,n)$^3$He, D(d,p)$^3$H, D(d,n)$^3$He, and D(d,d)D. Observables include total and differential cross sections, vector and tensor analyzing powers, and polarization-transfer coefficients. Parameters of the R-matrix which yield the best fit to existing data are selected and can be used to predict other, unmeasured observables. This parametrization has been used to establish the present energy level scheme for $^4$He [Til92].

## 6.1 Summary of the R-matrix formalism

The R-matrix approach, first discussed in [Kap38], has been reviewed in [Wig47, Lan58]. A Bloch operator approach has been given in [Hal80], as presented below.

In figure 6-1, two particles in the entrance channel are described by bound state ("internal") wavefunctions $\phi_1$ and $\phi_2$. They approach each other with the separation denoted by the coordinate $r_c$. In the exterior region $r_c > a_c$, where $a_c$ is the channel radius, the nucleons are assumed to be in pairs of clusters. In the interior region, ($r_c < a_c$), the short-range nuclear forces act, and the nucleons may be redistributed into two new clusters. The R-matrix formalism is used to relate the exterior region to the interior region.

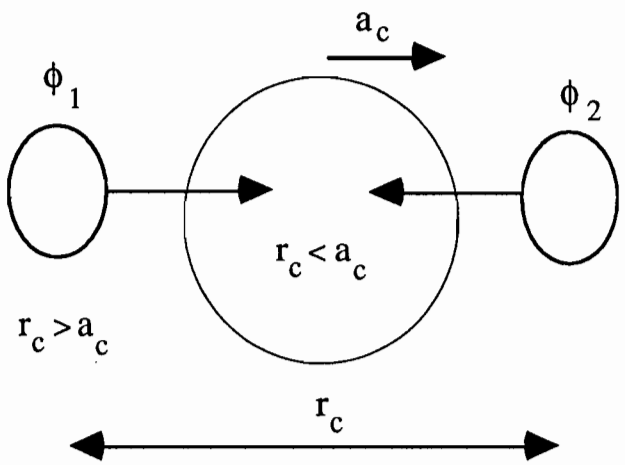


Figure 6-1. The entrance channel for an interaction of two particles, defining the interior and exterior regions.

To understand how the R-matrix parameters relate to the collision matrix and observables, such as cross sections, it is instructive to consider the simple and familiar problem of S-wave scattering from an arbitrary potential well of radius $r = a_c = a$ [Vog59]. In this case there is one entrance and one exit channel, so that the R-matrix reduces to an R-number. The radial part of the Schrödinger equation in this case is

$$-\frac{\hbar^2}{2m}\frac{d^2\psi}{dr^2}+V(r)\psi=E\psi \tag{6.1}$$

Instead of solving this problem, which includes positive energy solutions and virtual states, we apply boundary value conditions to determine the stationary states, inside $r \leq a$:

$$-\frac{\hbar^2}{2m}\frac{d^2X_\lambda}{dr^2}+V(r)X_\lambda=EX_\lambda \tag{6.2}$$

The boundary condition is

$$\left(\frac{dX_\lambda}{dr}+bX_\lambda\right)_{r=a}=0, \tag{6.3}$$

where b is a boundary condition of arbitrary value. Since these eigenfunctions form a complete set, the desired wave function, $\psi$, can be expanded in terms of them:

$$\psi=\sum_\lambda A_\lambda X_\lambda\ , \qquad A_\lambda=\int_0^a X_\lambda\psi\,dr \tag{6.4}$$

If (6.1) is multiplied by $X_\lambda$ and (6.2) by $\psi$, the difference taken, and the result integrated from r = 0 to r = a, the result is

$$\frac{\hbar^2}{2m}\left(\psi\frac{dX_\lambda}{dr}-X_\lambda\frac{d\psi}{dr}\right)_{r=a}=(E-E_\lambda)\int_0^a\psi X_\lambda\,dr=(E-E_\lambda)A_\lambda \tag{6.5}$$

Solving for A and substituting into (6.4), we obtain

$$\psi(r)=\frac{\hbar^2}{2m}\sum_\lambda\frac{X_\lambda(r)X_\lambda(a)}{(E-E_\lambda)}\left\{\frac{d\psi(a)}{dr}+b\psi(a)\right\}=G(r,a)\left\{\frac{d\psi(a)}{dr}+b\psi(a)\right\} \tag{6.6}$$

The interpretation of this result is that if the wavefunction and its radial derivative are both known at r = a, then the wavefunction is known for all r ≤ a. The R-number can now be defined via the energy Green's function:

$$R = G(a,a) = \frac{\hbar^2}{2ma}\sum_{\lambda}\frac{X_\lambda(a)X_\lambda(a)}{(E-E_\lambda)} = \sum_{\lambda}\frac{\gamma_\lambda{}^2}{(E-E_\lambda)} \tag{6.7}$$

where $\gamma_\lambda$ is the reduced width or amplitude. The logarithmic derivative at r = a is:

$$\frac{1}{\psi(a)}\frac{d\psi(a)}{dr} = (1-bR)/R \tag{6.8}$$

according to the boundary condition.

The logarithmic derivatives of the interior and exterior wavefunctions must match at the boundary r = a. In the exterior region, there is zero potential and the wavefunction can be written as the sum of incoming and outgoing plane waves:

$$\psi_{ext} = I - UO = \frac{1}{\sqrt{4\pi v}}e^{-ikr} - U\frac{1}{\sqrt{4\pi v}}e^{ikr} \tag{6.9}$$

Here U is the collision number, the one-channel precursor to the collision matrix of scattering theory and v is the relative velocity of the fragments. By taking the logarithmic derivative of this wavefunction at the boundary and setting it equal to (6.8), the collision number is obtained in terms of the R number and boundary condition number

$$U = e^{-2ika}\frac{1-bR+ikaR}{1-bR-ikaR} \tag{6.10}$$

Observables of interest, such as the cross section, can be determined from U. In a fitting program, R can be varied to give the best fit to the scattering observables.

The more realistic, and much more complicated situation involves $L \geq 0$ scattering of charged particles with spin and reactions, which result in the quantum numbers changing between the entrance and exit channels. The R-number becomes generalized to an R-matrix. It is in this situation that the R-matrix prescription shows its utility. Again, the specifically nuclear interaction is assumed to vanish outside the region $r_c > a_c$ and the R-matrix is used to give the value of the logarithmic derivative at the boundary, so that the interaction potentials in the internal region do not need to be known. In this development it is helpful to introduce the boundary conditions for the eigenfunctions by using a boundary value Bloch operator (see, for example, [Hal80]). In the exterior region, the wavefunction is described by Coulomb functions, and the R-matrix is related to the nuclear transition matrix.

The Hamiltonian for the system in the internal region is $H_{in}$. The Schrödinger equation inside the channel surface is

$$(H_{in} - E)\psi = 0 \tag{6.11}$$

A Bloch operator, $L_B$, acting on $\psi$ can be added to both sides:

$$(H_{in} + L_B - E)\psi = L_B\psi \tag{6.12}$$

so that

$$\psi = (H_{in} + L_B - E)^{-1} L_B\psi \tag{6.13}$$

In (6.13) if $L_B$ is chosen to be an operator which projects onto the channel surface, then the wavefunction inside the reaction surface will be completely determined if its projection onto the surface is known. In addition, judicious choice of $L_B$ will make $(H_{in}+L_B-E)^{-1}$ Hermitian. That choice is [Hal80]

$$L_B = \sum_c |c\rangle\langle c|\left(\frac{\partial}{\partial r_c} r_c - B_c\right) \tag{6.14}$$

where

$$|c\rangle = \left(\frac{\hbar^2}{2m_c a_c}\right)^{1/2} \frac{\delta(r_c - a_c)}{a_c} \left\{ \left[\phi_1 \otimes \phi_2\right]_{s,\mu} \otimes i^l Y_{lm}(\hat{r}_c) \right\}_{JM}$$
$$= \left(\frac{\hbar^2}{2m_c a_c}\right)^{1/2} \frac{\delta(r_c - a_c)}{a_c} Y_c(\hat{r}_c) \tag{6.15}$$

is the channel surface function, and the set of $B_c$ are real, energy-independent boundary condition numbers which may otherwise be arbitrary.

The operator $L_B$ is a projection operator, and the delta function ensures that the projection is confined to the channel surface $r_c = a_c$. Any wavefunction operated on by $L_B$ will be expanded in terms of the channel eigenfunctions $Y_c(\hat{r}_c)$ at $r_c = a_c$. To see that this choice of $L_B$ makes $(H_{in}+L_B-E)^{-1}$ and its inverse Hermitian, consider Green's theorem in one dimension applied to well-behaved functions u(r) and v(r):

$$\int_0^a dr \left( u\frac{\partial^2 v}{\partial r^2} - v\frac{\partial^2 u}{\partial r^2} \right) = \left[ u\frac{\partial v}{\partial r} - v\frac{\partial u}{\partial r} \right]_{r=a} \tag{6.16}$$

This may be manipulated in order to show that

$$\int_0^a dr \; u\left(\frac{\partial^2}{\partial r^2} - \delta(r-a)\frac{\partial}{\partial r}\right)v = \int_0^a dr \; v\left(\frac{\partial^2}{\partial r^2} - \delta(r-a)\frac{\partial}{\partial r}\right)u \tag{6.17}$$

which shows that $\left(\frac{\partial^2}{\partial r^2} - \delta(r-a)\frac{\partial}{\partial r}\right)$ is Hermitian and complex conjugates are not involved. It is the kinetic energy term in the Hamiltonian which prevents it from being Hermitian, but the addition of the Bloch operator transforms $(H_{in}-E)$ into an operator which is Hermitian, as is its inverse, the Greens operator $G_B$, given by

$$G_B = \left(H_{in} + L_B - E\right)^{-1} \tag{6.18}$$

Then (6.13) becomes

$$\psi = G_B L_B \psi \tag{6.19}$$

and the wavefunction projected onto a channel surface function gives

$$\langle c'|\psi\rangle = \sum_c \langle c'|G_B|c\rangle\langle c|\left(\frac{\partial}{\partial r_c}r_c - B_c\right)|\psi\rangle \tag{6.20}$$

The eigenfunctions and eigenvalues which satisfy

$$\left(H_{in} + L_B - E_\lambda\right)|\lambda\rangle = 0 \tag{6.21}$$

can be used to express the the Green's function operator

$$G_B = \sum_\lambda \frac{|\lambda\rangle\langle\lambda|}{E_\lambda - E} \tag{6.22}$$

The set of numbers $\langle c'|G_B|c\rangle$ are defined to be the elements of the R-matrix:

$$R^B_{c'c} \equiv \langle c'|G_B|c\rangle = \sum_\lambda \frac{\langle c'|\lambda\rangle\langle\lambda|c\rangle}{E_\lambda - E} = \sum_\lambda \frac{\gamma_{\lambda c'}\ \gamma^T_{\lambda c}}{E_\lambda - E} \tag{6.23}$$

where the $\gamma_{\lambda c}$ are called *reduced-width amplitudes* for level $\lambda$ and channel c. The utility of such an identification is that the elements of the R-matrix are related to the nuclear transition matrix, as discussed below.

For $r_c = a_c$, the wavefunctions are products of channel eigenfunctions $Y_c(\hat{r}_c)$ and Coulomb functions. For the case with an entrance channel c and an exit channel c', the appropriate scattering solutions involve the nuclear transition amplitudes $T^N_{c'c}$ and the regular ($F_c$) and ($H_c^+$) outgoing-wave solutions:

$$\langle c'|\psi\rangle = F_{c'}(a_c)\delta_{c'c} + H^{(+)}_{c'}(a_c)T^N_{c'c} \tag{6.24}$$

The relation between the nuclear transition matrix elements and those for the nuclear scattering matrix is

$$S^N_{c'c} = \delta_{c'c} + 2iT^N_{c'c} \tag{6.25}$$

and any observable can be calculated if the $S^N$ or $T^N$ matrix is known.

A relationship similar to (6.20) is valid for the wavefunction outside the channel radius, except with a set of boundary condition numbers $L_c$. These are chosen to be the

logarithmic derivative of the outgoing wave evaluated at the boundary. The real and imaginary parts of $L_c$ are the shift and the penetrability, respectively:

$$L_c = \left[ \frac{\partial H_c^{(+)} r_c}{\partial r_c} \Big/ H_c^{(+)} \right]_{r_c = a_c} = S_c + iP_c \tag{6.26}$$

In matrix notation, with $\langle c | \psi \rangle = \Psi_c$ , (6.20) at r=$a_c$ with the known outer-region wavefunction becomes

$$\begin{aligned}
\Psi &= \mathbf{R_L}[\Psi' - \mathbf{L}\Psi] \\
\mathbf{F} + \mathbf{H}^{(+)}\mathbf{T}^{\mathbf{N}} &= \mathbf{R_L}\left[\mathbf{F}' + \mathbf{H}^{(+)'}\mathbf{T}^{\mathbf{N}} - \mathbf{L}\left(\mathbf{F} + \mathbf{H}^{(+)}\mathbf{T}^{\mathbf{N}}\right)\right] \\
&= \mathbf{R_L}\left[\mathbf{F}' - \mathbf{L}\mathbf{F}\right] \\
&= \mathbf{R_L}\left[\mathbf{F}' - \mathbf{H}^{(+)'}\left(\mathbf{H}^{(+)}\right)^{-1}\mathbf{F}\right] \\
&= \mathbf{R_L}\left(\mathbf{H}^{(+)}\right)^{-1}\left[\mathbf{F}'\mathbf{H}^{(+)} - \mathbf{H}^{(+)'}\mathbf{F}\right]
\end{aligned} \tag{6.27}$$

The second step of which follows since $\mathbf{H}^{(+)'} - \mathbf{L}\mathbf{H}^{(+)} = 0$ by definition. Since the Wronskian of $\left(\mathbf{F}, \mathbf{H}^{(+)}\right)$ is unity, we have

$$\mathbf{T}^{\mathbf{N}} = \left(\mathbf{H}^{(+)}\right)^{-1}\mathbf{R_L}\left(\mathbf{H}^{(+)}\right)^{-1} - \left(\mathbf{H}^{(+)}\right)^{-1}\mathbf{F} \tag{6.28}$$

This shows the relationship between the R-matrix and the $T^N$-matrix.

The R-matrix has the same poles as the $T^N$-matrix, and the $T^N$-matrix can be used to calculate the scattering observables. With this connection to the observables, the R-matrix parameters, the $E_\lambda$, the $\gamma_{\lambda c}$, and the $a_c$, are varied to fit the available data.

## 6.2 The LANL R-matrix analysis

The actual LANL charge-independent R-matrix analysis procedure for the A=4 has been described in [Hal80] and [Hal91]. In general, all published data for a given system are entered into an input file, and then the LANL code EDA (Energy-Dependent Analysis) is used to adjust R-matrix parameters such as the reduced-width amplitudes

$\gamma_{\lambda c}$ and the energy levels $E_\lambda$ in (6.23) so as to obtain the best fit to the data, as determined by the minimization of a $\chi^2$ function.

The reduced-width amplitudes and the energy levels have definite isospin, T. For the four-nucleon problem T is usually restricted to 0 or 1. The T=1 channels are p-$^3$He and n-$^3$H.

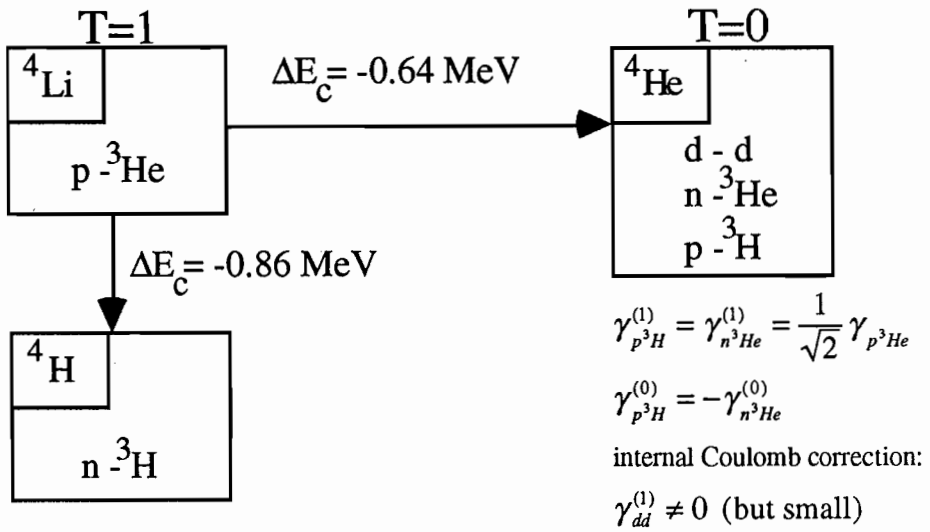


Figure 6-2 Schematic of the charge-independent, four nucleon R-matrix analysis [Hal91].

The scheme for the LANL charge-independent A=4 analysis is shown in Figure 6-2 (Figure 1 in [Hal91]). The model assumption is that $H_{in}$ has only a small charge dependence. The p-$^3$He data below 20 MeV are used to determine the T=1 parameters, with a channel radius of 4.9 fm and partial waves to L=3. To check the T=1 results, a Coulomb energy shift of -0.86 MeV is applied to the $E_\lambda$, then the R-matrix parameters are used to calculate the n-$^3$H total cross section and S-wave scattering lengths. The energy shifted parameters from p-$^3$He are found to satisfactorily reproduce the data for n-$^3$H [Hal90].

To determine the R-matrix parameters for the $^4$He system, the p-$^3$He results are permitted a slight energy shift and are then used for the T=1 part of the $^4$He system,

significantly reducing the number of parameters which need to be fit. The T=1 energy shifts and the T=0 R-matrix parameters are allowed to vary in the $^4$He fit. Data on d-d, p-$^3$H, and n-$^3$He corresponding to $^4$He excitations up to 29 MeV are included in the analysis; the d-d channel radius is set to 7 fm, and 4.9 fm is used for the p-$^3$H, and n-$^3$He channel radii, just as in the p-$^3$He case. The highest partial wave allowed in any of the channels is L = 3, because permitting higher order partial waves significantly increases the number of parameters to be fit and the data are well-represented with this set of partial waves. Note that $L \leq 3$ in a scattering amplitude implies $L \leq 2\times3 = 6$ in an observable, as discussed in section 5.1.

This approach has been useful in characterizing the differences between the D(d,p)$^3$H and D(d,n)$^3$He cross sections at very low energies – including the larger 0° to 90° asymmetry for D(d,n)$^3$He compared to D(d,p)$^3$H and the larger D(d,n)$^3$He total cross section. The fit to the D(d,p)$^3$H and D(d,n)$^3$He observables is improved by introducing isospin-1 d-d amplitudes in triplet P-waves, which should vanish if isospin is strictly conserved. Although the T=1 amplitudes give widths that are as small as 0.1% of the T=0 widths, their effects are sufficient to influence the calculations [Hal91]. Such small amplitudes are consistent with those expected from internal Coulomb mixing (as suggested in [Ser72]), although this analysis merely indicates the size of the T=1 amplitude, and not its origin.

In October 1992, Hale and I reanalyzed the $^4$He system by including our analyzing power data. The R-matrix parameters determined *prior* to the inclusion of our data in the fit were used to *predict* our analyzing powers. Our data were included in a new R-matrix fit using EDA on a CRAY X-MP computer at LANL. These were the first D(d,p)$^3$H and D(d,n)$^3$He tensor analyzing powers measured below $E_d$ = 150 keV admitted into the fit. The minimization was permitted to continue until the $\chi^2$ function did not change appreciably with each subsequent iteration, although the absolute

minimum $\chi^2$ may not have been found. In this sense, the fit is preliminary; it provides a good indication of how our data affect the parametrization.

The fits which include our data and predictions made without our data are shown in Figures 6-3 to 6-6. The predictions represent the data fairly well, except at the most forward and most backward angles. This is not surprising, considering that they lack low energy tensor analyzing power data. In terms of Legendre expansions, the unpolarized cross section for a reaction with identical particles in the entrance channel is represented by a linear combination of $P_k(\cos\theta)$ with even-k terms only. Including $A_{zz}$ and $(A_{xx}-A_{yy})$ data requires the addition of odd-k $P_k(\cos\theta)$ and $P_k^2(\cos\theta)$ linear combinations, both of which are very sensitive to forward and backward angles. The fit including our data corrects these discrepancies for the most part. Keeping in mind that this is a preliminary analysis, the addition of our data also seems to improve the fit to the data of [Bro90] slightly.

One feature of this parametrization is that the fits to the data seem to be quite sensitive to small changes in the R-matrix parameters [Hal92]. However, including our data in the fit shifts some of the parameters; for example, the amplitude corresponding to the interesting entrance channel quintet S state becomes about 10% larger. As described in [Til92], the quintet S transitions at the d+d threshold (at an excitation energy of 23.848 MeV) result from the very broad ($\Gamma_d$ = 8.21 MeV) quintet-S level in $^4$He at 27.42 MeV.

Future plans for the LANL R-matrix project call for other recent data (including other low energy analyzing power data) to be included in the fit and for longer searches to be initiated [Hal92]. The R-matrix parameters can be used to characterize the energy levels in $^4$He, as is done in [Til92].

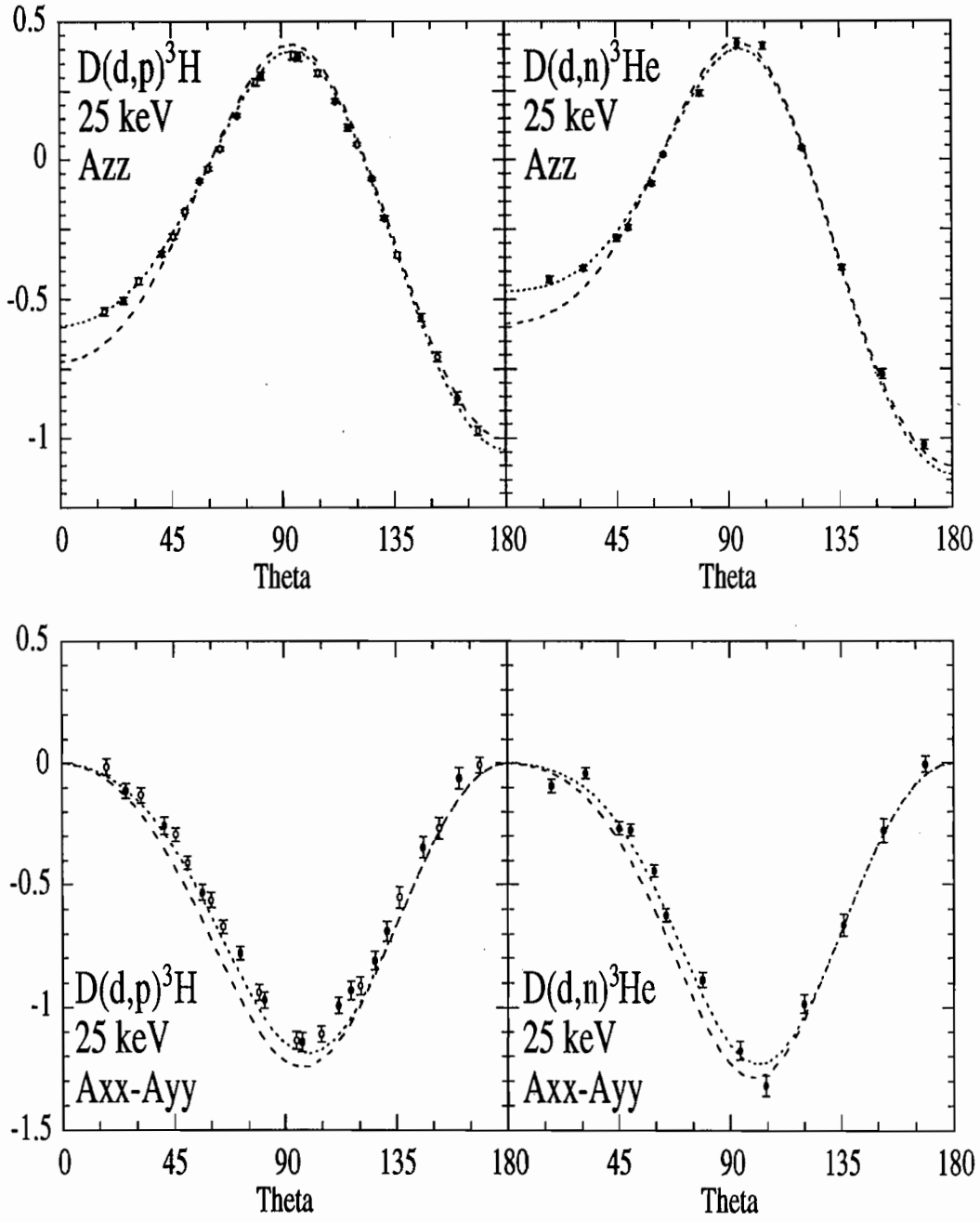


Figure 6-3. Our data for $A_{zz}$ and $A_{xx}$-$A_{yy}$ for $D(d,p)^3H$ and $D(d,n)^3He$ at $E_d$ = 25 keV ($E_R$ = 20.9 keV). The dashed lines are the R-matrix predictions made without our data included. The dotted lines are the R-matrix fits which include our data.

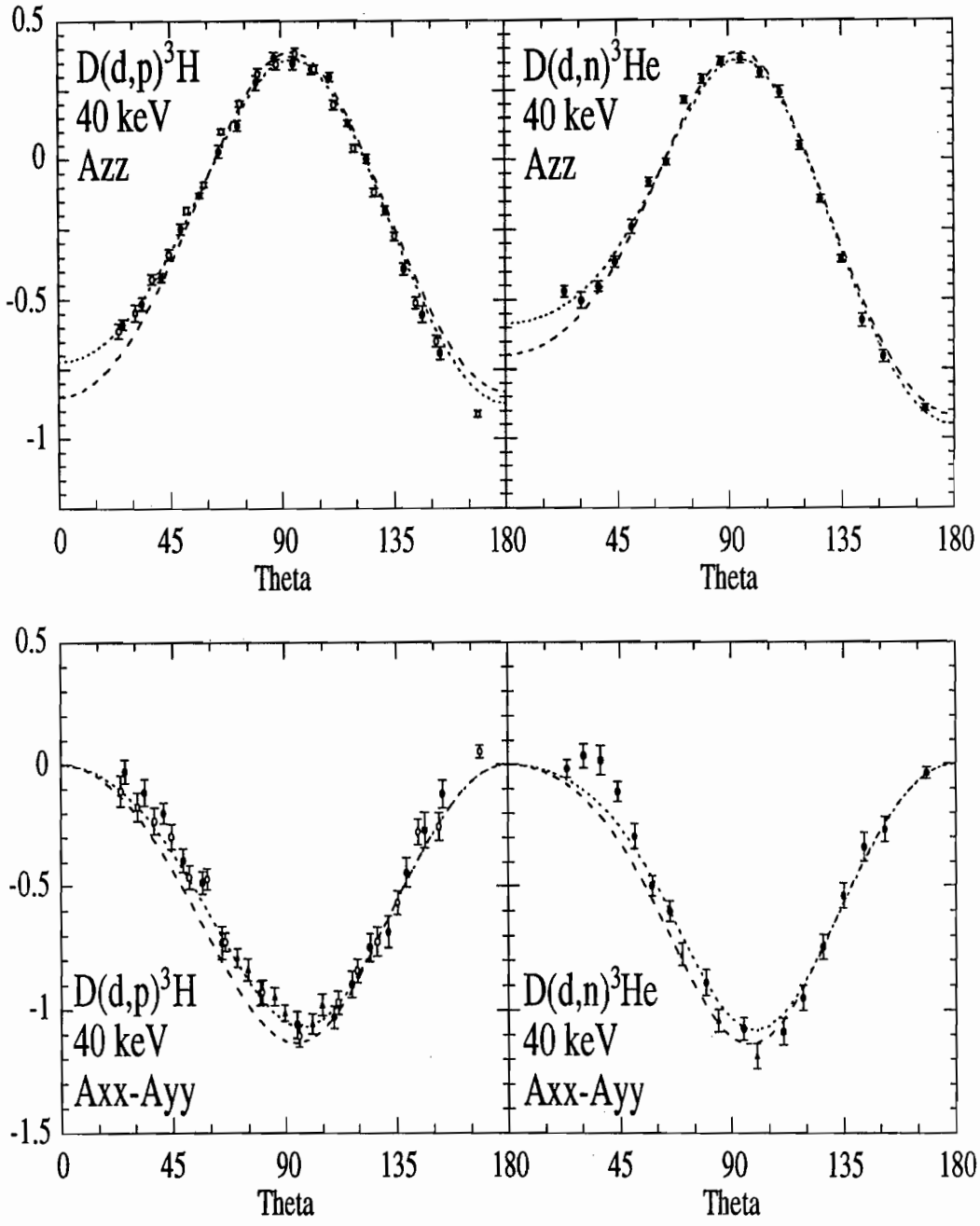


Figure 6-4. Our data for $A_{zz}$ and $A_{xx}$-$A_{yy}$ for $D(d,p)^3H$ and $D(d,n)^3He$ at $E_d$ = 40 keV ($E_R$ = 38.7 keV for $A_{zz}$ and 38.4 keV for $A_{xx}$-$A_{yy}$ ). The dashed lines are the R-matrix predictions made without our data included. The dotted lines are the R-matrix fits which include our data.

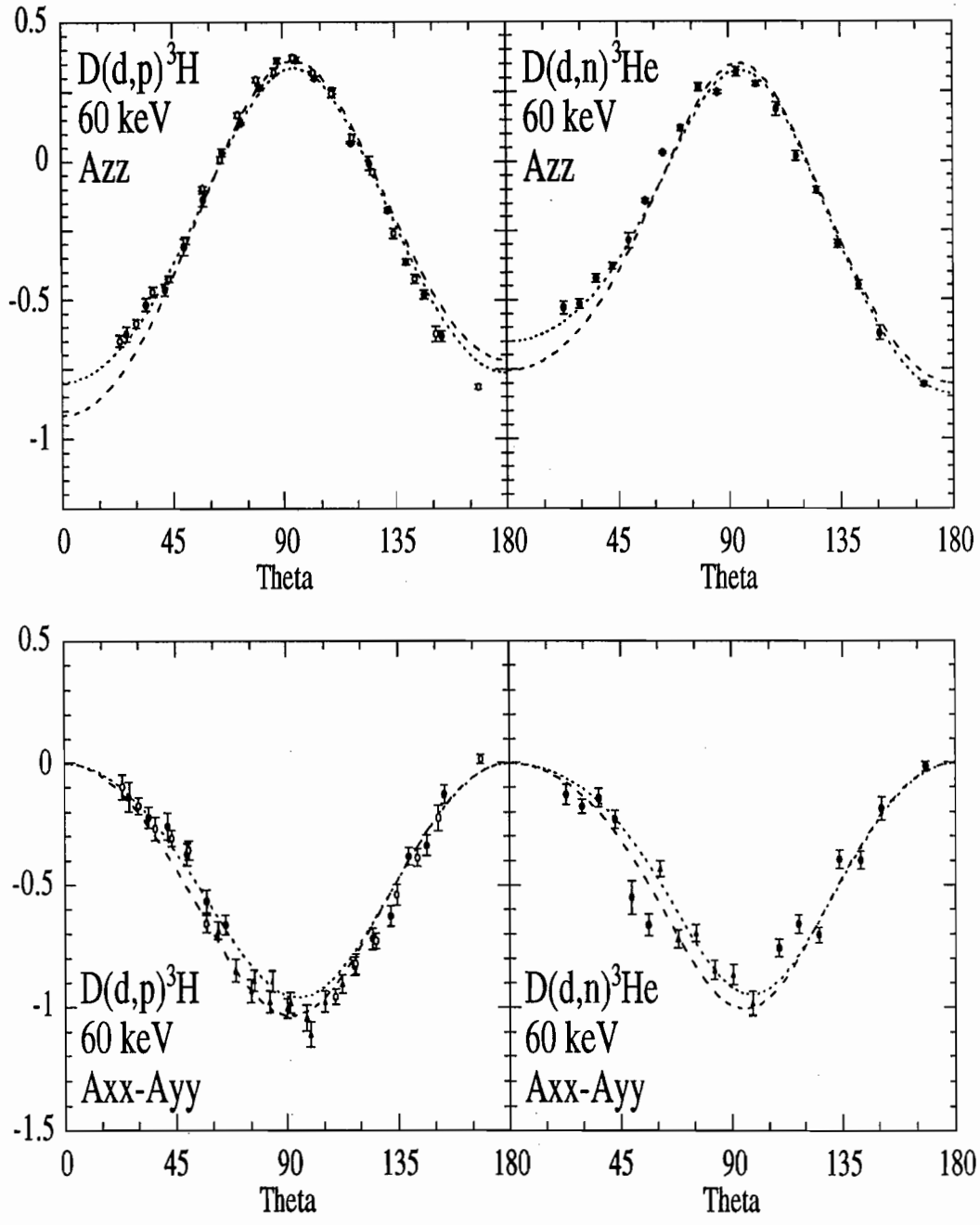


Figure 6-5. Our data for $A_{zz}$ and $A_{xx}$-$A_{yy}$ for $D(d,p)^3H$ and $D(d,n)^3He$ at $E_d$ = 60 keV ($E_R$ = 55.0 keV $A_{zz}$ and 56.2 keV for$A_{xx}$-$A_{yy}$ ). The dashed lines are the R-matrix predictions made without our data included. The dotted lines are the R-matrix fits which include our data.

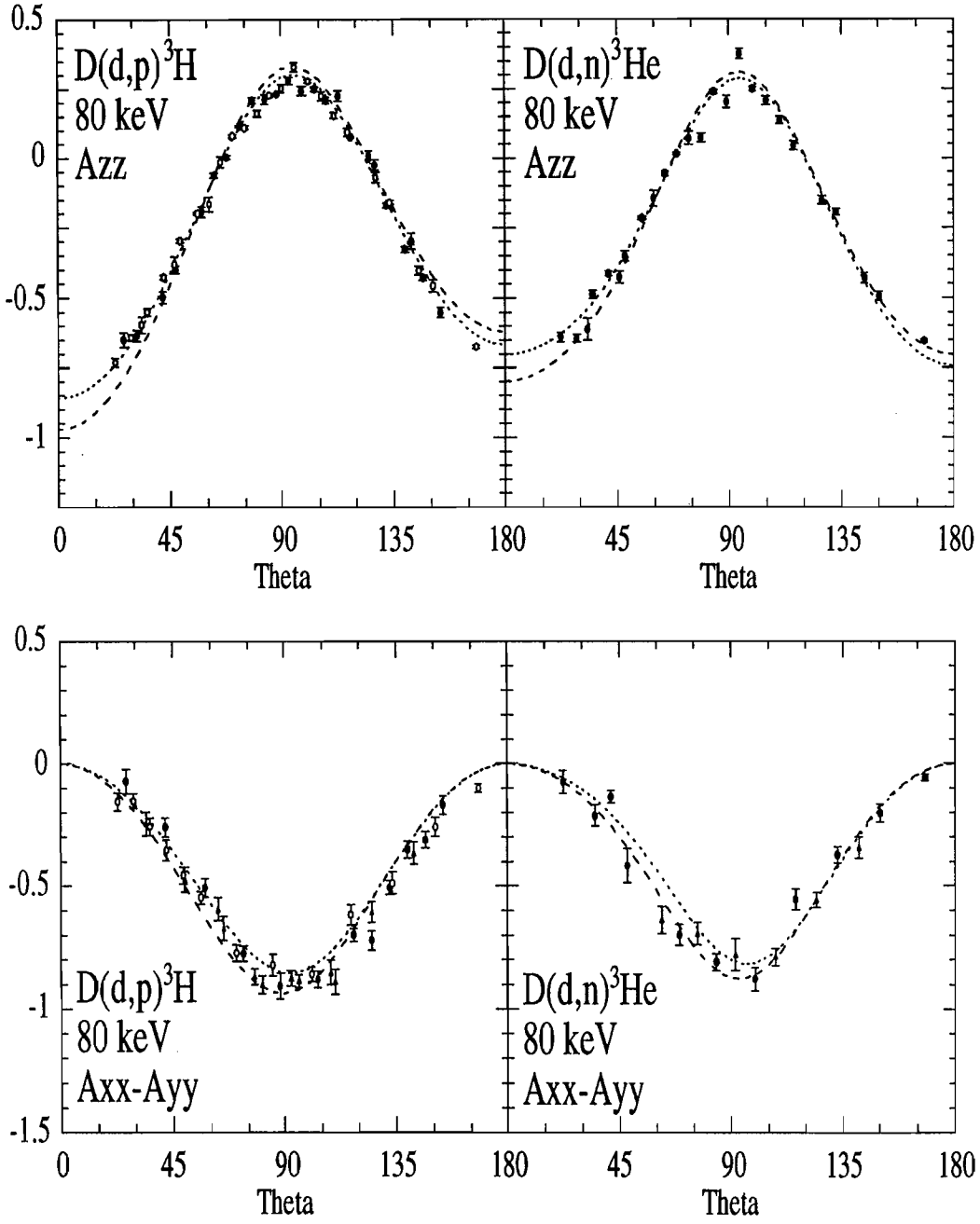


Figure 6-6. Our data for $A_{zz}$ and $A_{xx}$-$A_{yy}$ for $D(d,p)^3H$ and $D(d,n)^3He$ at $E_d$ = 80 keV ($E_R$ = 75.1 keV $A_{zz}$ and 75.7 keV for$A_{xx}$-$A_{yy}$ ). The dashed lines are the R-matrix predictions made without our data included. The dotted lines are the R-matrix fits which include our data.

# VII. Summary and Conclusions: Exodus

We summarize the accomplishments of this research and discuss future work.

## 7.1 Concluding Scientific Postscript

We have completed precision measurements of the angular distributions of $A_{zz}$ and $A_{xx}$-$A_{yy}$ for the $D(d,p)^3H$ and $D(d,n)^3He$ reactions at very low laboratory-frame energies ($25 \leq E_d \leq 80$ keV). The data are among the lowest energy analyzing powers ever measured. These two charge symmetry reactions have very similar analyzing powers with a smooth energy dependence within this energy range. Our data for $D(d,p)^3H$ show good agreement with other recent measurements on this reaction [Tag92], although there are some discrepancies with the data of [Bec92] which cannot be attributed to normalization errors.

In the course of this investigation novel target-making techniques were developed to make the experiments possible. To minimize the effects of target degradation, we developed a data collection method using rapid spin-state changing. In addition, a polarimeter, based on the $D(d,p)^3H$ reaction at 10°, was designed and calibrated using the data of [Tag92]. This polarimeter is useful for monitoring the tensor polarization of low energy beams.

Our data are consistent with the conclusions from R-matrix analyses and resonating group model calculations [Hof86] that entrance quintet S-states are important to the reaction mechanisms which govern the fusion reactions $D(d,p)^3H$ and $D(d,n)^3He$. This conclusion conflicts with the idea that polarizing the fuel in a plasma

fusion reactor would suppress the neutron yield [Kul82], and our finding agrees with the results of other researchers [Sch92].

We have compared our data with the analyzing powers predicted by an R-matrix analysis which did not include our data or other recent low energy analyzing power data, and good agreement was found. Our tensor analyzing powers were then included in an R-matrix analysis that we performed in collaboration with Hale at LANL. These measurements contribute to an improved understanding of the $^4$He system through their effects on the R-matrix parameters.

## 7.2 Suggestions for future work

Perhaps the guiding principle of graduate education in physics is that experience is the best teacher. Even it this dictum is not true, a healthy dose of experience does give one the required arrogance to offer unsolicited advice.

With measurements on tensor analyzing powers for D(d,p)$^3$H performed by groups in three different countries, and simultaneous D(d,p)$^3$H and D(d,n)$^3$He measurements by two of these groups at energies below 90 keV, the experimental situation seems well covered, despite the discrepancies between our data and the data of [Bec92]. Considerable effort would be required to go to even lower energies, because of the rapidly decreasing cross section. Furthermore, there is little reason to make further measurements on these reactions without more compelling theoretical or experimental motivation. Measurements of polarization transfer and polarization correlation data have not been made at very low energies, but experiments to obtain these data involve double scattering and are very difficult and time-consuming.

Experimental motivation for measuring the analyzing powers at higher or lower energies might arise if the D(d,p)$^3$H reaction is needed for polarimetry, since this reaction provides both vector and tensor sensitivity for deuteron beams at low energies. For experimental situations where knowledge of the tensor polarization is sufficient, the

$^3$He(d,p)$^4$He reaction provides higher yields at the upper end of our energy range and at energies available from our miniTandem accelerator [Bla92], and the analyzing powers for this reaction are fairly well estimated from the $J^\pi = 3/2^+$ resonance properties. (See, however, [McI67, Gar74].)

The four-nucleon system is beginning to be accessible to realistic nuclear structure calculations, as reported, for example, in [Fon89]. For the A = 4 system, computer limitations currently prevent the complete treatment that has been given to the bound states of the three-nucleon system. Our low-energy data should prove useful in the theoretical understanding of the system at very low energies.

We have some concern that the expressions for the observables in terms of the transition matrix elements as given in [Ady69] are incomplete. We have begun an analysis using the symbolic manipulation program *Mathematica* to compute the multiple sums of bilinear combinations of matrix elements which form the Legendre expansion coefficients for the unpolarized and polarized cross sections. *Mathematica* provides exact values for the Clebsch-Gordan and Racah coefficients needed for this manipulation. Although this work is not yet completed, the initial results for the unpolarized cross sections indicate that Ad'yasevich may have neglected matrix element combinations which he thought were small [Ady69]. It may prove instructive to complete this procedure and to see how the results obtained compare with the expressions used in the Köln matrix element fit.

## Appendix A: A Practical Primer for Polarization

The nuclear potential contains terms which depend upon the spin of the interacting particles. Therefore, the nuclear cross section for a reaction with the reactants in a specially prepared spin state may be different than that for reactants with all spin magnetic substates equally populated. The study of such experimental situations is facilitated by knowledge of some common definitions and conventions, as described below.

### A.1 Polarization of a beam of deuterons

The word "polarized" is an adjective which modifies the word "beam". Although we may colloquially refer to "a polarized deuteron", the concept of polarization actually only makes sense for an *ensemble* of particles.

A particle with some non-zero spin S has (2S+1) magnetic substates, relative to some chosen spin axis. In an *unpolarized* beam, each of the (2S+1) substates is equally populated. For an unpolarized beam of deuterons (spin-1 particles), one-third of the particles are in each of the magnetic substates (labelled m = -1, 0, +1). For a *polarized* beam, the substates are unequally populated.

The beam is polarized in the polarized ion source, and such sources have solenoidal magnetic fields parallel to the source axis that establish the axis about which the spins precess. Usually, the spin axis is parallel to the predominant momentum direction in the source. A beam of polarized nuclei is produced by first polarizing an ensemble of atoms, and then removing the electrons. The nuclear magnetic states can be populated unequally if transitions occur which move atoms

from one state to another, as discussed in section 2.1.1. After leaving the source, the beam enters the Wien filter region, where there are crossed magnetic and electric fields which rotate the spins so they are oriented in the proper direction once the beam reaches the target, after traversing bending magnets and lenses.

The polarization of the beam must be characterized. Formally, $\{(2S+1)^2 - 1\}$ parameters are required to completely describe an ensemble of spin-S particles, since the density matrix for a system with (2S+1) magnetic substates is a $(2S+1) \times (2S+1)$ Hermitean matrix with its trace normalized to unity [Sim74]. This implies that for protons, three parameters, and for deuterons, eight independent parameters are required to completely specify the beam polarization. For an arbitrary Cartesian coordinate system and an arbitrary ensemble of spin-1 particles, $P_x$, $P_y$, and $P_z$ are the vector polarization components and $P_{xx}$, $P_{yy}$, $P_{zz}$, $P_{xy}$, $P_{yz}$, and $P_{zx}$ are the tensor polarization components with

$$P_{XX} + P_{YY} + P_{ZZ} = 0. \tag{A.1}$$

These are the eight (nine numbers minus one constraint) independent parameters.

The *vector polarization* $P_i$ is related to the expectation value for the spin component in the $i^{th}$ direction for the ensemble of particles, so for spin S = 1/2 or 1,:

$$P_i = (1 + \delta_{S,\frac{1}{2}})\langle S_i \rangle, \quad i = x, y, z \tag{A.2}$$

Likewise, the *tensor polarization* components are

$$P_{ij} = \frac{3}{2}\left\langle S_i S_j + S_j S_i \right\rangle - 2\delta_{ij} \tag{A.3}$$

In practice, fewer than eight parameters are required to characterize a polarized beam. For a deuteron beam created in an ion source with cylindrical symmetry, two parameters, the vector polarization $P_Z$ and the tensor polarization $P_{ZZ}$ are needed. The upper-case Z axis appearing in the subscripts represents the spin axis. If $N_+$, $N_0$, and $N_-$ represent the fraction of deuterons in the +1, 0, and -1 magnetic substates, respectively, then, for the vector polarization,

$$\text{let } |\Psi\rangle = \sum_m a_m |m\rangle,$$

$$S_z|\Psi\rangle = \sum_m a_m m|m\rangle$$

$$P_z = \langle\Psi|S_z|\Psi\rangle = \sum_m a_m a_m^* m\langle m'|m\rangle = \sum_m (a_m)^2 m = N_+ - N_-$$

Similarly, for the tensor polarization,

$$\left(S_z\right)^2|\Psi\rangle = \sum_m a_m m^2|m\rangle$$

$$\langle\Psi|\left(S_z\right)^2|\Psi\rangle = \sum_m (a_m)^2 m^2 = N_+ + N_- = 1 - N_0, \textit{ since } N_+ + N_- + N_0 = 1$$

$$P_{zz} = \langle\Psi|3\left(S_z\right)^2 - 2\delta_{zz}|\Psi\rangle = 3(1-N_0) - 2 = 1 - 3N_0$$

Therefore,

$$\begin{aligned} P_Z &= N_+ - N_- \\ P_{ZZ} &= 1 - 3N_0 \end{aligned} \qquad \text{(A.4)}$$

The $P_Z$ ranges from -1 to +1, and the $P_{ZZ}$ varies from -2 to +1. For this cylindrical ion source geometry, $P_{XX} = P_{YY} = -1/2\ P_{ZZ}$, and all other components vanish. Therefore, for an ensemble created in our ion source, only two components, $P_Z$ and $P_{ZZ}$, and the direction of the spin axis need to be specified.

The orientation of the spin axis is described via the coordinate system defined by the Madison Convention. The coordinate system chosen for the Madison Convention [Mad70] is shown in figure A-1. The z-axis is selected to be in the direction of the momentum of the incident particles. The y-axis points in the direction of $\mathbf{k_{in}} \times \mathbf{k_{out}}$ and the x-axis is chosen to form a right-handed coordinate system. The angle $\beta$ is the angle between the z-axis and the spin axis **s**, and $\phi$ is measured from the x-axis to $\mathbf{s} \times \mathbf{k_{in}}$. Alternatively, $\phi$ is the angle from the y-axis to the projection of **s** in the x-y plane.

The y-axis is defined according to the outgoing momentum vector, and this has some notable consequences. Consider a horizontal scattering chamber with detectors placed on the left and right sides (Left and right are defined with respect to the incoming beam direction. Note that, in optics, the reverse convention is used). Suppose a reaction occurs with a polarized beam with a vertical spin axis and the reactant particle scatters to the left detector. The vector $\mathbf{k_{in}} \times \mathbf{k_{out}}$ then points vertically upwards, parallel to the spin axis. Likewise, $\mathbf{s} \times \mathbf{k_{in}}$ points to the left, parallel to the x-axis. Therefore, for a reaction which scatters a particle to the left with a vertical spin axis the angle $\phi$ is 0°. If the reactant scatters to the right, $\mathbf{k_{in}} \times$

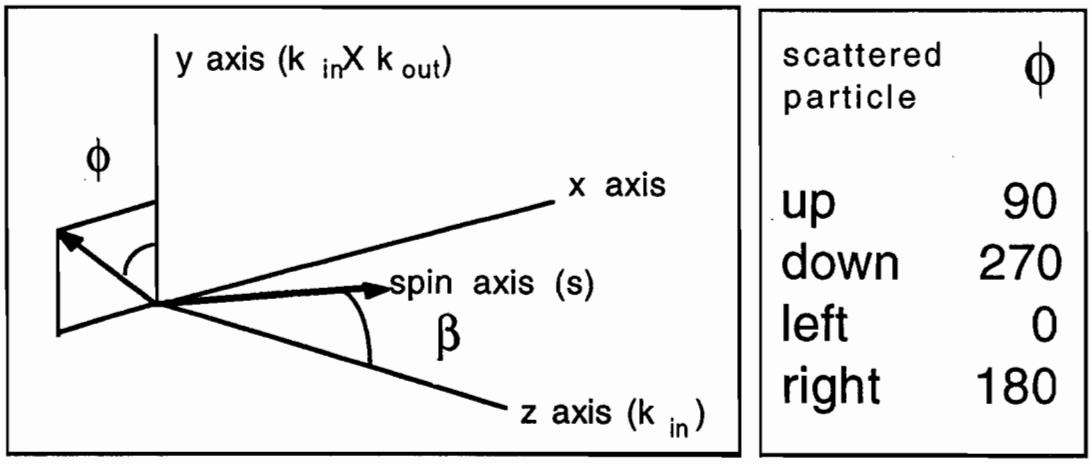


Figure A-1: The Madison Convention coordinate system [Mad70].

$\mathbf{k_{out}}$ points downwards and $\phi = 180°$. "Up" and "down" thus correspond to $\phi = 270°$ and $\phi = 90°$ respectively. If the spin axis points along **z**, then $\beta = 0°$ and $\phi$ is undefined since $\mathbf{s} \times \mathbf{k_{in}}$ is zero. In practice, for a system with conserved parity, this is not a problem because the expression for the response of an arbitrary detector is independent of $\phi$ in this case [see (A.9) below].

All the polarization components are rotated from the source frame into the new frame by the following relations [Ohl73]:

$$
\begin{aligned}
P_x &= -P_Z \sin(\beta)\sin(\phi) & P_{xy} &= -\tfrac{3}{2} P_{ZZ} \sin(\beta)\cos(\phi)\sin(\phi) \\
P_y &= +P_Z \sin(\beta)\cos(\phi) & P_{yz} &= +\tfrac{3}{2} P_{ZZ} \sin(\beta)\cos(\phi)\cos(\phi) \\
P_z &= +P_Z \cos(\beta) & P_{xz} &= -\tfrac{3}{2} P_{ZZ} \sin(\beta)\cos(\phi)\sin(\phi) \\
& & P_{xx} &= +\tfrac{1}{2} P_{ZZ}\left[3\sin^2(\beta)\sin^2(\phi) - 1\right] \\
& & P_{yy} &= +\tfrac{1}{2} P_{ZZ}\left[3\sin^2(\beta)\sin^2(\phi) - 1\right] \\
& & P_{zz} &= +\tfrac{1}{2} P_{ZZ}\left[3\cos^2(\beta) - 1\right]
\end{aligned}
\qquad \text{(A.5)}
$$

### A.2 Analyzing powers for reactions involving polarized deuterons

Since the nuclear interaction depends in part on the spin states of the interacting nucleons, the cross section for nuclear interations will show a spin dependence. For an unpolarized beam, the number of counts collected in a detector is given by:

$$I_0(\theta,\phi) = N_b n_t \varepsilon \Delta\Omega \frac{\partial\sigma}{\partial\theta} \qquad \text{(A.6)}$$

which is read as

(number of counts in a solid angle $\Delta\Omega$ near $\theta$, $\phi$ ) =

( number of incident beam particles)

× (number of target atoms intercepted)

× (efficiency for detection) × ( solid angle of detector)

× ( probability that the reaction will scatter to the $\theta$, $\phi$ direction).

The number of counts deposited in a detector by a reaction involving a polarized beam of spin-1 particles is, assuming parity conservation, [Ohl73]:

$$I_0(\theta,\phi) = I_0(\theta)\left\{1+\frac{3}{2}P_y A_y(\theta)+\frac{2}{3}P_{xz}A_{xz}(\theta) + \frac{1}{3}P_{xx}A_{xx}(\theta)+\frac{1}{3}P_{yy}A_{yy}(\theta)+\frac{1}{3}P_{zz}A_{zz}(\theta)\right\} \tag{A.7}$$

The A's are the Cartesian *analyzing powers* for the reaction. Note that only a few of the polarization components appear in this expression. Because of parity conservation, the only vector component that appears is $P_y$. The tensor components which are missing from this expression are also eliminated because of parity. (We note, in honor of our colleagues at TUNL, that parity violation can be measured by determining some of these "vanishing" terms.) Like the trace condition on the polarization tensors, the second-rank analyzing power tensors satisfy the relation:

$$A_{xx}(\theta)+A_{yy}(\theta)+A_{zz}(\theta)=0 \tag{A.8}$$

This beautifully symmetric expression for the polarized cross section is usually written in a less pleasing, though more useful, way, by substituting the relations (A.5):

$$I_0(\theta,\phi) = I_0(\theta)\left\{1+\frac{3}{2}P_z A_y(\theta)\sin\beta\cos\phi - P_{zz}A_{xz}(\theta)\sin\beta\cos\beta\sin\phi - \frac{1}{4}P_{zz}\left(A_{xx}(\theta)-A_{yy}(\theta)\right)\sin^2\beta\cos 2\phi + \frac{1}{4}P_{zz}A_{zz}(\theta)\left[3\cos^2\beta-1\right]\right\} \tag{A.9}$$

Here the vector and tensor polarizations are written with lower case subscripts, and it is understood that they are defined in the "ion source" coordinate system. The expressions for the number of counts in the left, right, up and down detectors (figure 1-1) in a polarization state (p) are

$$
\begin{aligned}
L_p &= I_L(\theta)\left\{1+\tfrac{3}{2}P_z^{(p)}A_y(\theta)\sin\beta+\tfrac{1}{2}P_{zz}^{(p)}\left[A_{yy}(\theta)\sin^2\beta+A_{zz}(\theta)\cos^2\beta\right]\right\} \\
R_p &= I_R(\theta)\left\{1-\tfrac{3}{2}P_z^{(p)}A_y(\theta)\sin\beta+\tfrac{1}{2}P_{zz}^{(p)}\left[A_{yy}(\theta)\sin^2\beta+A_{zz}(\theta)\cos^2\beta\right]\right\} \\
U_p &= I_U(\theta)\left\{1+P_{zz}^{(p)}A_{xz}(\theta)\sin\beta\cos\beta+\tfrac{1}{2}P_{zz}^{(p)}\left[A_{xx}(\theta)\sin^2\beta+A_{zz}(\theta)\cos^2\beta\right]\right\} \\
D_p &= I_D(\theta)\left\{1-P_{zz}^{(p)}A_{xz}(\theta)\sin\beta\cos\beta+\tfrac{1}{2}P_{zz}^{(p)}\left[A_{xx}(\theta)\sin^2\beta+A_{zz}(\theta)\cos^2\beta\right]\right\}
\end{aligned}
\qquad \text{(A.10)}
$$

Recall from the example above that the "up" direction is defined by the Madison Convention and the experimenter's setting of the Wien filter; it may or may not point away from the center of the earth.

The question remains, "What *is* an analyzing power?" Whereas the polarization components contain information about the ensemble of spin states coming into a reaction, the analyzing powers describe how the cross section of a reaction responds to the incoming polarization. Consider the equation for the left detector. If the incoming beam has a vanishing $P_{zz}$ and $\beta$ is 90° then this equation becomes very simple. Solving for $A_y$ yields:

$$
A_y(\theta)=\frac{\frac{2}{3}\left(\frac{L_p(\theta)}{I_L(\theta)}-1\right)}{P_z} \qquad \text{(A.11)}
$$

In this case the vector analyzing power is inversely proportional to the vector polarization and is proportional to the difference between the ratio of polarized to unpolarized counts and unity.

If we isolate the tensor analyzing powers by selecting a beam with $P_{ZZ} = +1$ and $P_Z = 0$, and rotate the polarization axis to be parallel to the incident momentum ($\beta = 0°$), then the responses of all detectors (L, R, U, D) reduce to the same form, and we find that $A_{ZZ}$ is equal to twice the difference between the polarized and unpolarized cross sections, divided by the unpolarized cross section. This schematic, operational definition was introduced by Haeberli ( see [Hae74] and [Ton80]), and such a visualization can be made for each of the analyzing powers. The analyzing powers are normalized so that they have the following ranges:

$$\begin{aligned} -1 &\le A_y(\theta) \le +1 \\ -2 &\le A_{xx}(\theta) \le +1 \\ -2 &\le A_{yy}(\theta) \le +1 \\ -2 &\le A_{zz}(\theta) \le +1 \\ -\tfrac{3}{2} &\le A_{xz}(\theta) \le +\tfrac{3}{2} \\ -3 &\le \left(A_{xx}(\theta) - A_{yy}(\theta)\right) \le +3 \end{aligned} \qquad \text{(A.12)}$$

As a final note, the analyzing powers can also be defined in a spherical coordinate system, and it is common to encounter this definition in the literature. The relations between the observables in Cartesian and spherical coordinates are [Mad70]:

| *Polarizations*: | *Analyzing powers*: | | |
|---|---|---|---|
| $t_{11} = \frac{\sqrt{3}}{2} P_z$ | $iT_{11} = \frac{\sqrt{3}}{2} A_y$ | $T_{21} = -\frac{1}{\sqrt{3}} A_{xz}$ | (A.13) |
| $t_{20} = \frac{1}{\sqrt{2}} P_{zz}$ | $T_{20} = \frac{1}{\sqrt{2}} A_{zz}$ | $T_{22} = \frac{1}{2\sqrt{3}} \left(A_{xx} - A_{yy}\right)$ | |

## Appendix B: Data Tables

The analyzing powers $A_{zz}$ and $(A_{xx}-A_{yy})$ for the $D(d,p)^3H$ and $D(d,n)^3He$ reactions are listed below. The reaction energy, $E_R$, is defined in section 4.1.

| $D(d,p)^3H$ at $E_R$ = 21 keV | | |
|---|---|---|
| θ (CM) | $A_{zz}$ | $\Delta A_{zz}$ |
| 25.78 | -0.507 | 0.012 |
| 41.18 | -0.339 | 0.009 |
| 56.51 | -0.076 | 0.005 |
| 71.73 | 0.161 | 0.007 |
| 81.81 | 0.305 | 0.014 |
| 96.83 | 0.374 | 0.015 |
| 111.73 | 0.213 | 0.008 |
| 116.67 | 0.118 | 0.011 |
| 126.51 | -0.068 | 0.005 |
| 131.41 | -0.209 | 0.008 |
| 146.06 | -0.565 | 0.015 |
| 160.63 | -0.856 | 0.022 |
| 169.04 | -0.973 | 0.015 |
| 152.67 | -0.708 | 0.017 |
| 136.46 | -0.340 | 0.009 |
| 120.48 | 0.056 | 0.005 |
| 104.82 | 0.315 | 0.010 |
| 94.57 | 0.377 | 0.014 |
| 79.50 | 0.283 | 0.013 |
| 64.82 | 0.041 | 0.005 |
| 60.00 | -0.032 | 0.007 |

| (continued) | | |
|---|---|---|
| θ (CM) | $A_{zz}$ | $\Delta A_{zz}$ |
| 50.48 | -0.186 | 0.006 |
| 45.78 | -0.277 | 0.008 |
| 31.84 | -0.437 | 0.011 |
| 18.12 | -0.546 | 0.014 |

| $D(d,n)^3He$ at $E_R$ = 21 keV | | |
|---|---|---|
| θ (CM) | $A_{zz}$ | $\Delta A_{zz}$ |
| 168.94 | -1.023 | 0.016 |
| 152.41 | -0.768 | 0.018 |
| 136.07 | -0.388 | 0.009 |
| 119.98 | 0.043 | 0.004 |
| 104.24 | 0.410 | 0.013 |
| 93.97 | 0.420 | 0.019 |
| 78.90 | 0.241 | 0.011 |
| 64.24 | 0.018 | 0.006 |
| 59.45 | -0.086 | 0.008 |
| 49.98 | -0.244 | 0.008 |
| 45.31 | -0.281 | 0.011 |
| 31.49 | -0.389 | 0.010 |
| 17.91 | -0.430 | 0.011 |

| $D(d,p)^3H$ at $E_R$ = 21 keV | | |
|---|---|---|
| θ (CM) | $(A_{xx}-A_{yy})$ | $\Delta(A_{xx}-A_{yy})$ |
| 25.78 | -0.113 | 0.030 |
| 41.18 | -0.255 | 0.036 |
| 56.51 | -0.530 | 0.032 |
| 71.73 | -0.779 | 0.028 |
| 81.81 | -0.969 | 0.032 |
| 96.83 | -1.141 | 0.038 |
| 111.73 | -0.992 | 0.033 |
| 116.67 | -0.930 | 0.038 |
| 126.51 | -0.810 | 0.038 |
| 131.41 | -0.689 | 0.041 |
| 146.06 | -0.344 | 0.044 |
| 160.63 | -0.062 | 0.044 |
| 169.04 | -0.007 | 0.031 |
| 152.67 | -0.267 | 0.044 |
| 136.46 | -0.550 | 0.044 |
| 120.48 | -0.912 | 0.036 |
| 104.82 | -1.108 | 0.034 |
| 94.57 | -1.135 | 0.036 |
| 79.50 | -0.939 | 0.034 |
| 64.82 | -0.671 | 0.028 |
| 60.00 | -0.562 | 0.031 |
| 50.48 | -0.409 | 0.027 |
| 45.78 | -0.292 | 0.029 |
| 31.84 | -0.131 | 0.032 |
| 18.12 | -0.015 | 0.033 |

| $D(d,n)^3He$ at $E_R$ = 21 keV | | |
|---|---|---|
| θ (CM) | $(A_{xx}-A_{yy})$ | $\Delta(A_{xx}-A_{yy})$ |
| 168.94 | -0.005 | 0.033 |
| 152.41 | -0.278 | 0.048 |
| 136.07 | -0.664 | 0.044 |
| 119.98 | -0.985 | 0.039 |
| 104.24 | -1.318 | 0.041 |
| 93.97 | -1.175 | 0.038 |
| 78.90 | -0.888 | 0.030 |
| 64.24 | -0.624 | 0.027 |
| 59.45 | -0.442 | 0.024 |
| 49.98 | -0.275 | 0.024 |
| 45.31 | -0.268 | 0.026 |
| 31.49 | -0.042 | 0.023 |
| 17.91 | -0.094 | 0.028 |

| D(d,p)$^3$H at $E_R$ = 38 keV | | |
|---|---|---|
| θ (CM) | $A_{zz}$ | $\Delta A_{zz}$ |
| 25.98 | -0.589 | 0.018 |
| 33.75 | -0.515 | 0.023 |
| 41.50 | -0.421 | 0.015 |
| 49.22 | -0.248 | 0.020 |
| 56.91 | -0.128 | 0.010 |
| 64.56 | 0.029 | 0.023 |
| 72.19 | 0.123 | 0.019 |
| 79.77 | 0.279 | 0.026 |
| 87.32 | 0.366 | 0.021 |
| 94.83 | 0.348 | 0.023 |
| 102.29 | 0.326 | 0.018 |
| 109.72 | 0.298 | 0.015 |
| 117.11 | 0.132 | 0.011 |
| 124.46 | 0.003 | 0.015 |
| 131.78 | -0.182 | 0.015 |
| 139.07 | -0.391 | 0.021 |
| 146.33 | -0.553 | 0.030 |
| 153.57 | -0.691 | 0.024 |
| 168.79 | -0.911 | 0.012 |
| 152.06 | -0.648 | 0.019 |
| 143.76 | -0.511 | 0.023 |
| 135.52 | -0.273 | 0.014 |
| 127.36 | -0.116 | 0.014 |
| 119.29 | 0.042 | 0.013 |
| 111.31 | 0.198 | 0.017 |
| 103.44 | 0.327 | 0.015 |
| 95.69 | 0.382 | 0.019 |
| 88.05 | 0.344 | 0.018 |
| 80.53 | 0.309 | 0.019 |

| (continued) | | |
|---|---|---|
| θ (CM) | $A_{zz}$ | $\Delta A_{zz}$ |
| 73.13 | 0.203 | 0.010 |
| 65.84 | 0.102 | 0.009 |
| 58.68 | -0.089 | 0.009 |
| 51.62 | -0.182 | 0.014 |
| 44.66 | -0.340 | 0.019 |
| 37.79 | -0.428 | 0.018 |
| 31.00 | -0.548 | 0.029 |
| 24.28 | -0.613 | 0.027 |

| D(d,n)$^3$He at $E_R$ = 38 keV | | |
|---|---|---|
| θ (CM) | $A_{zz}$ | $\Delta A_{zz}$ |
| 168.66 | -0.894 | 0.012 |
| 151.73 | -0.706 | 0.021 |
| 143.35 | -0.576 | 0.023 |
| 135.03 | -0.356 | 0.013 |
| 126.79 | -0.144 | 0.014 |
| 118.66 | 0.048 | 0.015 |
| 110.63 | 0.241 | 0.021 |
| 102.72 | 0.311 | 0.017 |
| 94.94 | 0.361 | 0.017 |
| 87.28 | 0.352 | 0.015 |
| 79.76 | 0.288 | 0.017 |
| 72.37 | 0.214 | 0.012 |
| 65.11 | -0.010 | 0.010 |
| 57.98 | -0.081 | 0.017 |
| 50.97 | -0.242 | 0.025 |
| 44.07 | -0.366 | 0.020 |
| 37.27 | -0.454 | 0.020 |
| 30.56 | -0.504 | 0.029 |
| 23.93 | -0.472 | 0.020 |

| $D(d,p)^3H$ at $E_R$ = 39 keV | | |
|---|---|---|
| θ (CM) | $(A_{xx}-A_{yy})$ | $\Delta(A_{xx}-A_{yy})$ |
| 25.98 | -0.028 | 0.049 |
| 33.75 | -0.113 | 0.054 |
| 41.50 | -0.199 | 0.044 |
| 49.22 | -0.392 | 0.050 |
| 56.91 | -0.483 | 0.046 |
| 64.56 | -0.729 | 0.066 |
| 79.77 | -0.932 | 0.049 |
| 94.83 | -1.058 | 0.055 |
| 109.72 | -1.029 | 0.044 |
| 117.11 | -0.895 | 0.053 |
| 124.46 | -0.747 | 0.057 |
| 131.78 | -0.685 | 0.065 |
| 139.07 | -0.442 | 0.061 |
| 146.33 | -0.268 | 0.071 |
| 153.57 | -0.121 | 0.057 |
| 168.79 | 0.053 | 0.026 |
| 152.06 | -0.254 | 0.057 |
| 143.76 | -0.275 | 0.053 |
| 135.52 | -0.566 | 0.049 |
| 127.36 | -0.723 | 0.058 |
| 119.29 | -0.841 | 0.047 |
| 111.31 | -0.970 | 0.047 |
| 95.69 | -1.104 | 0.046 |
| 80.53 | -0.927 | 0.049 |
| 65.84 | -0.725 | 0.037 |
| 58.68 | -0.469 | 0.043 |
| 51.62 | -0.461 | 0.047 |
| 44.66 | -0.295 | 0.050 |
| 37.79 | -0.230 | 0.054 |
| 31.00 | -0.173 | 0.058 |
| 24.28 | -0.107 | 0.063 |

| (continued) | | |
|---|---|---|
| θ (CM) | $(A_{xx}-A_{yy})$ | $\Delta(A_{xx}-A_{yy})$ |
| 74.72 | -0.837 | 0.044 |
| 89.83 | -1.012 | 0.034 |
| 104.77 | -0.977 | 0.044 |
| 100.84 | -1.054 | 0.041 |
| 85.53 | -0.945 | 0.036 |
| 70.69 | -0.787 | 0.037 |

| $D(d,n)^3He$ at $E_R$ = 39 keV | | |
|---|---|---|
| θ (CM) | $(A_{xx}-A_{yy})$ | $\Delta(A_{xx}-A_{yy})$ |
| 168.66 | -0.038 | 0.024 |
| 151.73 | -0.268 | 0.052 |
| 143.35 | -0.339 | 0.059 |
| 135.03 | -0.540 | 0.051 |
| 126.79 | -0.746 | 0.050 |
| 118.66 | -0.952 | 0.051 |
| 110.63 | -1.088 | 0.054 |
| 94.94 | -1.076 | 0.044 |
| 79.76 | -0.890 | 0.051 |
| 65.11 | -0.602 | 0.041 |
| 57.98 | -0.498 | 0.041 |
| 50.97 | -0.295 | 0.051 |
| 44.07 | -0.112 | 0.040 |
| 37.27 | 0.016 | 0.061 |
| 30.56 | 0.034 | 0.050 |
| 23.93 | -0.017 | 0.037 |
| 100.11 | -1.186 | 0.050 |
| 84.76 | -1.042 | 0.046 |
| 69.94 | -0.776 | 0.044 |

| D(d,p)$^3$H at $E_R$ = 55 keV | | |
|---|---|---|
| θ (CM) | $A_{zz}$ | $\Delta A_{zz}$ |
| 26.20 | -0.624 | 0.026 |
| 34.03 | -0.517 | 0.023 |
| 41.83 | -0.464 | 0.022 |
| 49.60 | -0.309 | 0.030 |
| 57.33 | -0.138 | 0.023 |
| 65.03 | 0.032 | 0.015 |
| 72.68 | 0.136 | 0.005 |
| 80.28 | 0.265 | 0.009 |
| 87.84 | 0.361 | 0.010 |
| 95.34 | 0.364 | 0.011 |
| 102.80 | 0.301 | 0.007 |
| 110.22 | 0.255 | 0.012 |
| 117.58 | 0.067 | 0.004 |
| 124.90 | -0.007 | 0.024 |
| 132.18 | -0.175 | 0.009 |
| 139.42 | -0.363 | 0.010 |
| 146.63 | -0.480 | 0.016 |
| 153.81 | -0.632 | 0.018 |
| 168.52 | -0.815 | 0.008 |
| 151.40 | -0.623 | 0.029 |
| 142.92 | -0.424 | 0.017 |
| 134.52 | -0.259 | 0.018 |
| 126.21 | -0.038 | 0.009 |
| 118.01 | 0.086 | 0.013 |
| 109.92 | 0.243 | 0.014 |
| 101.97 | 0.318 | 0.007 |
| 94.16 | 0.371 | 0.009 |
| 86.48 | 0.321 | 0.012 |
| 78.96 | 0.294 | 0.008 |
| 71.58 | 0.167 | 0.007 |

| (continued) | | |
|---|---|---|
| θ (CM) | $A_{zz}$ | $\Delta A_{zz}$ |
| 64.35 | 0.006 | 0.011 |
| 57.26 | -0.098 | 0.006 |
| 50.30 | -0.286 | 0.014 |
| 43.46 | -0.425 | 0.012 |
| 36.74 | -0.472 | 0.018 |
| 30.11 | -0.587 | 0.015 |
| 23.56 | -0.650 | 0.021 |

| D(d,n)$^3$He at $E_R$ = 55 keV | | |
|---|---|---|
| θ (CM) | $A_{zz}$ | $\Delta A_{zz}$ |
| 168.36 | -0.804 | 0.008 |
| 151.00 | -0.622 | 0.026 |
| 142.42 | -0.448 | 0.017 |
| 133.92 | -0.297 | 0.014 |
| 125.52 | -0.105 | 0.011 |
| 117.24 | 0.019 | 0.016 |
| 109.09 | 0.187 | 0.024 |
| 101.09 | 0.277 | 0.008 |
| 93.24 | 0.321 | 0.016 |
| 85.55 | 0.247 | 0.006 |
| 78.02 | 0.265 | 0.014 |
| 70.65 | 0.118 | 0.011 |
| 63.45 | 0.031 | 0.003 |
| 56.41 | -0.142 | 0.007 |
| 49.51 | -0.285 | 0.028 |
| 42.74 | -0.378 | 0.012 |
| 36.10 | -0.423 | 0.015 |
| 29.57 | -0.514 | 0.016 |
| 23.13 | -0.530 | 0.024 |

| $D(d,p)^3H$ at $E_R$ = 56 keV | | |
|---|---|---|
| θ (CM) | $(A_{xx}-A_{yy})$ | $\Delta(A_{xx}-A_{yy})$ |
| 26.20 | -0.139 | 0.060 |
| 34.03 | -0.223 | 0.042 |
| 41.83 | -0.257 | 0.054 |
| 49.60 | -0.374 | 0.047 |
| 57.33 | -0.566 | 0.046 |
| 65.03 | -0.663 | 0.040 |
| 117.58 | -0.829 | 0.038 |
| 124.90 | -0.720 | 0.045 |
| 132.18 | -0.627 | 0.041 |
| 139.42 | -0.382 | 0.037 |
| 146.63 | -0.336 | 0.042 |
| 153.81 | -0.127 | 0.038 |
| 168.52 | 0.017 | 0.019 |
| 151.40 | -0.224 | 0.052 |
| 142.92 | -0.387 | 0.036 |
| 134.52 | -0.539 | 0.044 |
| 126.21 | -0.728 | 0.032 |
| 118.01 | -0.822 | 0.041 |
| 109.92 | -0.955 | 0.032 |
| 57.26 | -0.658 | 0.034 |
| 50.30 | -0.355 | 0.039 |
| 43.46 | -0.306 | 0.032 |
| 36.74 | -0.266 | 0.047 |
| 30.11 | -0.174 | 0.034 |
| 23.56 | -0.097 | 0.051 |

| (continued) | | |
|---|---|---|
| θ (CM) | $(A_{xx}-A_{yy})$ | $\Delta(A_{xx}-A_{yy})$ |
| 75.22 | -0.931 | 0.047 |
| 82.80 | -0.977 | 0.045 |
| 90.34 | -1.004 | 0.040 |
| 97.84 | -1.042 | 0.053 |
| 105.28 | -0.976 | 0.044 |
| 112.68 | -0.902 | 0.037 |
| 99.35 | -1.110 | 0.052 |
| 91.58 | -0.982 | 0.043 |
| 83.96 | -0.892 | 0.043 |
| 76.48 | -0.891 | 0.043 |
| 69.16 | -0.849 | 0.046 |
| 61.97 | -0.687 | 0.037 |
| $D(d,n)^3He$ at $E_R$ = 56 keV | | |
| θ (CM) | $(A_{xx}-A_{yy})$ | $\Delta(A_{xx}-A_{yy})$ |
| 168.36 | -0.014 | 0.019 |
| 151.00 | -0.185 | 0.047 |
| 142.42 | -0.398 | 0.035 |
| 133.92 | -0.394 | 0.037 |
| 125.52 | -0.704 | 0.032 |
| 117.24 | -0.660 | 0.039 |
| 109.09 | -0.758 | 0.034 |
| 56.41 | -0.663 | 0.045 |
| 49.51 | -0.551 | 0.068 |
| 42.74 | -0.230 | 0.036 |
| 36.10 | -0.144 | 0.038 |
| 29.57 | -0.177 | 0.029 |
| 23.13 | -0.128 | 0.041 |
| 98.45 | -0.982 | 0.049 |
| 90.65 | -0.866 | 0.042 |
| 83.02 | -0.847 | 0.039 |
| 75.55 | -0.697 | 0.034 |
| 68.24 | -0.720 | 0.036 |
| 61.09 | -0.432 | 0.032 |

| $D(d,p)^3H$ at $E_R$ = 75 keV | | |
|---|---|---|
| θ (CM) | $A_{zz}$ | $\Delta A_{zz}$ |
| 26.39 | -0.651 | 0.026 |
| 31.64 | -0.635 | 0.020 |
| 42.11 | -0.499 | 0.021 |
| 47.32 | -0.399 | 0.014 |
| 57.69 | -0.194 | 0.019 |
| 62.84 | -0.062 | 0.008 |
| 67.98 | 0.004 | 0.007 |
| 73.09 | 0.114 | 0.003 |
| 78.17 | 0.209 | 0.010 |
| 83.23 | 0.213 | 0.016 |
| 88.27 | 0.232 | 0.005 |
| 93.28 | 0.279 | 0.013 |
| 98.27 | 0.243 | 0.016 |
| 103.23 | 0.250 | 0.007 |
| 108.17 | 0.209 | 0.011 |
| 113.09 | 0.226 | 0.020 |
| 117.98 | 0.077 | 0.003 |
| 125.27 | 0.011 | 0.017 |
| 127.69 | -0.024 | 0.019 |
| 132.52 | -0.169 | 0.008 |
| 139.72 | -0.326 | 0.011 |
| 142.11 | -0.298 | 0.027 |
| 146.88 | -0.428 | 0.009 |
| 154.02 | -0.552 | 0.018 |

| | | (continued) |
|---|---|---|
| θ (CM) | $A_{zz}$ | $\Delta A_{zz}$ |
| 168.29 | -0.674 | 0.006 |
| 150.85 | -0.456 | 0.022 |
| 145.08 | -0.402 | 0.017 |
| 133.67 | -0.159 | 0.007 |
| 128.04 | -0.068 | 0.019 |
| 116.93 | 0.095 | 0.014 |
| 111.46 | 0.155 | 0.010 |
| 106.06 | 0.224 | 0.016 |
| 100.73 | 0.277 | 0.006 |
| 95.47 | 0.328 | 0.017 |
| 90.28 | 0.252 | 0.014 |
| 85.17 | 0.227 | 0.005 |
| 80.13 | 0.162 | 0.012 |
| 75.17 | 0.110 | 0.007 |
| 70.28 | 0.081 | 0.005 |
| 65.47 | -0.013 | 0.019 |
| 60.73 | -0.166 | 0.026 |
| 56.06 | -0.199 | 0.004 |
| 49.19 | -0.297 | 0.007 |
| 46.93 | -0.380 | 0.026 |
| 42.45 | -0.427 | 0.007 |
| 35.85 | -0.552 | 0.013 |
| 33.67 | -0.597 | 0.029 |
| 29.36 | -0.642 | 0.010 |
| 22.96 | -0.732 | 0.016 |

| D(d,n)$^3$He at $E_R$ = 75 keV | | |
|---|---|---|
| θ (CM) | $A_{zz}$ | $\Delta A_{zz}$ |
| 168.11 | -0.654 | 0.006 |
| 150.39 | -0.495 | 0.016 |
| 144.55 | -0.429 | 0.018 |
| 132.98 | -0.194 | 0.012 |
| 127.27 | -0.151 | 0.017 |
| 116.04 | 0.046 | 0.016 |
| 110.52 | 0.137 | 0.014 |
| 105.08 | 0.207 | 0.016 |
| 99.71 | 0.249 | 0.007 |
| 94.42 | 0.376 | 0.018 |
| 89.21 | 0.203 | 0.022 |
| 84.08 | 0.240 | 0.007 |
| 79.04 | 0.074 | 0.017 |
| 74.08 | 0.073 | 0.025 |
| 69.21 | 0.018 | 0.004 |
| 64.42 | -0.054 | 0.007 |
| 59.71 | -0.144 | 0.029 |
| 55.08 | -0.216 | 0.005 |
| 48.27 | -0.351 | 0.019 |
| 46.04 | -0.426 | 0.021 |
| 41.63 | -0.414 | 0.008 |
| 35.12 | -0.488 | 0.014 |
| 32.98 | -0.612 | 0.039 |
| 28.74 | -0.644 | 0.013 |
| 22.46 | -0.641 | 0.017 |

| D(d,n)$^3$He at $E_R$ = 76 keV | | |
|---|---|---|
| θ (CM) | $(A_{xx}-A_{yy})$ | $\Delta(A_{xx}-A_{yy})$ |
| 168.11 | -0.057 | 0.015 |
| 150.39 | -0.202 | 0.038 |
| 132.98 | -0.372 | 0.033 |
| 116.04 | -0.555 | 0.044 |
| 99.71 | -0.877 | 0.049 |
| 84.08 | -0.807 | 0.034 |
| 69.21 | -0.699 | 0.043 |
| 48.27 | -0.417 | 0.070 |
| 41.63 | -0.135 | 0.026 |
| 35.12 | -0.213 | 0.044 |
| 22.46 | -0.074 | 0.047 |
| 141.64 | -0.343 | 0.042 |
| 124.44 | -0.557 | 0.031 |
| 107.79 | -0.787 | 0.036 |
| 91.80 | -0.779 | 0.065 |
| 76.55 | -0.693 | 0.046 |
| 62.05 | -0.638 | 0.055 |

| D(d,p)$^3$H at $E_R$ = 76 keV | | |
|---|---|---|
| θ (CM) | $(A_{xx}-A_{yy})$ | $\Delta(A_{xx}-A_{yy})$ |
| 26.39 | -0.072 | 0.050 |
| 42.11 | -0.260 | 0.038 |
| 57.69 | -0.506 | 0.039 |
| 73.09 | -0.775 | 0.031 |
| 88.27 | -0.906 | 0.053 |
| 103.23 | -0.879 | 0.035 |
| 117.98 | -0.699 | 0.026 |
| 125.27 | -0.721 | 0.037 |
| 132.52 | -0.505 | 0.028 |
| 139.72 | -0.351 | 0.034 |
| 146.88 | -0.311 | 0.034 |
| 154.02 | -0.169 | 0.037 |
| 168.29 | -0.100 | 0.018 |
| 150.85 | -0.258 | 0.039 |
| 133.67 | -0.488 | 0.044 |
| 116.93 | -0.616 | 0.041 |
| 100.73 | -0.858 | 0.030 |
| 85.17 | -0.821 | 0.045 |
| 70.28 | -0.772 | 0.034 |
| 56.06 | -0.547 | 0.026 |
| 49.19 | -0.457 | 0.035 |
| 42.45 | -0.354 | 0.042 |
| 35.85 | -0.257 | 0.038 |
| 29.36 | -0.152 | 0.030 |
| 22.96 | -0.156 | 0.036 |

| (continued) | | |
|---|---|---|
| θ (CM) | $(A_{xx}-A_{yy})$ | $\Delta(A_{xx}-A_{yy})$ |
| 34.26 | -0.246 | 0.049 |
| 49.92 | -0.473 | 0.050 |
| 65.41 | -0.673 | 0.047 |
| 80.71 | -0.900 | 0.035 |
| 95.78 | -0.886 | 0.026 |
| 110.63 | -0.888 | 0.051 |
| 142.21 | -0.366 | 0.046 |
| 125.24 | -0.606 | 0.041 |
| 108.75 | -0.852 | 0.049 |
| 92.86 | -0.874 | 0.032 |
| 77.64 | -0.868 | 0.032 |
| 63.09 | -0.594 | 0.047 |

## References


[Abu88] S. Abu-Kamar, M. Igarashi, R.C. Johnson, and J.A. Tostevin, J. Phys. G: Nucl. Phys. 14 (1988) L1.

[Ady69] B.P. Ad'yasevich and D.E. Fomenko, Sov. J. Nucl. Phys. 9 (1969) 167.

[Ady81] B.P. Ad'yasevich, V.G. Antonenko, and D.E. Fomenko, Sov. J. Nucl. Phys. 33 (1981) 313.

[And77] H.H. Anderson and J.F. Ziegler, *Hydrogen Stopping Powers and Ranges in All Elements* (Pergamon Press, New York, 1977).

[Ass87] H.J. Assenbaum, K. Langanke, and C. Rolfs, Z. Phys. A327 (1987) 461.

[Bar89] R.J. Barlow, *Statistics: A Guide to the Use of Statistical Methods in the Physical Sciences* (Wiley, New York, 1989).

[Bec92] B. Becker, R. Randermann, B. Polke, S. Lemaître, R. Reckenfelderbäumer, P. Niessen, G. Rauprich, L. Sydow, and H. Paetz gen. Schieck, Few-Body Systems 13 (1992) 19.

[Bla92] T.C. Black, B.E. Hendrix, E.R. Crosson, K.A. Fletcher, H.J. Karwowski, and E.J. Ludwig, submitted for publication to Nucl. Instr. Meth., 1992.

[Boa83] M. Boas, *Mathematical Methods in the Physical Sciences* (Wiley, New York, 1983) p.728.

[Bro00] Brookhaven Instruments Corporation, Instruction manual for Model 1000 Current Integrator.

[Bro90] R.E. Brown, N. Jarmie, Phys. Rev. C41 (1990) 1391.

[Cec85] F.E. Cecil, R.J. Peterson, and P.D. Kunz, Nucl. Phys. A441 (1985) 477.

[Cle93] T.B. Clegg, W.M. Hooke, E.R. Crosson, A.W. Lovette, H. Middleton, H. Pfutzner, and K.A. Sweeton, submitted for publication to Nucl. Instr. Meth., 1993.

[Cor69] H. Cords, G.U. Din, and B.A. Robson, Nucl. Phys. A134 (1969) 561.

[Cro93] E.R. Crosson, K.A. Sweeton, H. Pfutzner, W.S. Wilburn, A.W. Lovette, T.B. Clegg, and H.J. Karwowski, submitted for publication to Nucl. Instr. Meth., 1993.

[Din93] D. Dinge, T.B. Clegg, E.R. Crosson, and H.W. Lewis, submitted for publication to Nucl. Instr. Meth., 1993.

[Fic85] D. Fick and H.M. Hofmann, Phys. Rev. Lett. 55 (1985) 1650.

[Fle92] K.A. Fletcher, T.C. Black, H.J Karwowski, E.J. Ludwig, and Y. Tagishi, accepted for publication in Nucl. Instr. Meth., 1992. Material from this paper has been reproduced here with the written permission of the publishers.

[Fon89] A.C. Fonseca, Phys. Rev. Lett. 63 (1989) 2036.

[Gal72] J.L. Gallant, Nucl. Instr. Meth. 102 (1972) 477.

[Gal85] J.L. Gallant, P. Dmytrenko, and R.H. Martin, Nucl. Instr. Meth. A236 (1985) 456.

[Gal87] J.L. Gallant and P. Dmytrenko, Nucl. Instr. Meth. A257 (1987) 29.

[Gar74] R. Garrett and W.W. Lindstom, Nucl. Phys. A224 (1974) 186.

[Gou81] C.R. Gould, L.G. Holzsweig, S.E. King, Y.C. Lau, R.V. Poore, and N.R. Roberson, IEEE Trans. Nucl. Sci. NS-28 (1981) 3708. See also pp. 3815,

3822, and 3834 in the same reference. IEEE Trans. Nucl. Sci. NS-30 (1983) 3758.

[Hae74] W. Haeberli, in *Polarization in Nuclear Physics*, edited by D. Fick (Springer-Verlag, 1974).

[Hal80] G.M. Hale and D.C Dodder, *Proc. Int. Conf. on Nucl. Cross Sections for Technology*, Knoxville, 1979, NBS Special Publication 594 (1980) 650.

[Hal90] G.M. Hale, D.C Dodder, J.D. Seagrave, B.L. Berman and T.W. Phillips, Phys. Rev. C42 (1990) 438.

[Hal91] G.M. Hale, Muon Catalyzed Fusion 5/6 (1990/91) 227.

[Hal92] G.M. Hale, private communication, 1992.

[Hof84] H.M. Hofmann and D. Fick, Phys. Rev. Lett. 52 (1984) 2038.

[Hof86] H.M. Hofmann, G.M. Hale, and R. Wölker in *Proc. Int. Workshop on Few-Body Approaches to Nuclear Reactions in Tandem and Cyclotron Energy Regions*, ed. S. Oryu, T. Sawada, (World Scientific, Singapore,1987).

[Iri73] Y. Irie, H. Yamamoto, H. Hasuyama, Y. Wakuta, Genshikaku-Kekyu 17 (1973) 567.

[Kap38] P.L. Kapur and R. Peierls, Proc. Roy. Soc. A166 (1938) 277.

[Kon48] E.J. Konopinski and E. Teller, Phys. Rev. 73 (1948) 822.

[Koo90] S.E. Koonin and M. Mukerjee, Phys. Rev. C42 (1990) 1639.

[Kra87] A. Kraus, H.W. Becker, H.P. Trautvetter, C. Rolfs, and K. Brand, Nucl. Phys. A465 (1987) 150.

[Kul82] R.M. Kulsrud, H.P. Furth, E.J. Valeo, and M. Goldhaber, Phys. Rev. Lett. 49 (1982) 1248.

[Lan58] A.M. Lane and R.G. Thomas, Rev. Mod. Phys. 30 (1958) 257.

[Lem90] S. Lemaître and H. Paetz gen. Schieck, Few-Body Systems 9 (1990) 155.

[Liu85] K.F. Liu, J.S. Zhang, and G.W. Shuy, Phys. Rev. Lett. 55 (1985) 1649.

[Mad70] *Proc. of the Third Int. Symp. on Polarization Phenomena in Nucl. Reactions*, Madison, Wisconsin, 1970. Edited by H.H. Barschall and W. Haeberli (Univ. of Wisconsin Press, 1971) p. xxv.

[McI67] L.C. McIntyre and W. Haeberli, Nucl. Phys. A91 (1967) 369.

[McQ50] A.D. McQuillan, Proc. Roy. Soc. London, Ser. A, 204 (1950) 309.

[Ohl71] G.G. Ohlsen, J.L. McKibben, G.P. Lawrence, P.W. Keaton, Jr., and D.D. Armstrong, Phys. Rev. Lett. 27 (1971) 599.

[Ohl73] G.G. Ohlsen and P.W. Keaton, Jr., Nucl. Instr. Meth. 109 (1973) 41.

[Opp35] J.R. Oppenheimer and M. Phillips, Phys. Rev. 48 (1935) 500.

[Pao89] P. Paolo, Nature 338 (1989) 711.

[Pfa85] E. Pfaff, A. Hofmann, E. Huttel, N. Kniest, M. Nau, G. Reiter, S. Tharraketta, and G. Clausnitzer, *Proc. Sixth Int. Symp. Polar. Phenom. in Nucl. Phys.*, Osaka, 1985, J. Phys. Soc. Jpn. 55 (1986) Suppl. 894.

[Pfa89] E. Pfaff, private communication (1989).

[Rol78] C. Rolfs, J. Gorres, K.U. Kettner, H. Lorenz-Wirba, P. Schmalbrock, H.P. Trautvetter, and W. Verhoeven, Nucl. Instr. Meth. 157 (1978) 19.

[Roo61] J.R. Rook and L.J.B. Goldfarb, Nucl. Phys. 27 (1961) 79.

[Sch87] H. Paetz gen. Schieck, private communication (1987).

[Sch88] H. Paetz gen. Schieck, Few-Body Systems 5 (1988) 171.

[Sch92] H. Paetz gen. Schieck, B. Becker, R. Randermann, S. Lemaître, P. Niessen, R. Reckenfelderbäumer, and L. Sydow, Phys. Lett. B276 (1992) 290.

[Ser72] V.A. Sergeyev, Phys. Lett. 38B (1972) 286.

[Sim74] M. Simonius, in *Polarization in Nuclear Physics*, edited by D. Fick (Springer-Verlag, 1974).

[Tag92] Y. Tagishi, N. Nakamoto, K. Katoh, J. Togawa, T. Hisamune and T. Yoshida, Phys. Rev. C46 (1992) R1155.

[Tan92] M. Tanifuji, Phys. Lett. B289 (1992) 233.

[Tho92] W.J. Thompson, Nucl. Instr. Meth. A317 (1992) 394.

[Til92] D.R. Tilley, H.R. Weller, and G.M. Hale, Nucl. Phys. A541(1992) 1.

[Ton80] S. A. Tonsfeldt, Ph.D. Thesis, University of North Carolina at Chapel Hill, 1980.(unpublished). Available from University Microfilms International, 300 N. Zeeb Rd. Ann Arbor, Michigan 48106.

[Vas90] V.S. Vasilevskiĭ, I. Yu. Rybkin and G.F. Filippov, Sov. J. Nucl. Phys. 51(1990)71.

[Vog59] E. Vogt, Chapter V in *Nuclear Reactions*, edited by P.M. Endt and M. Demeur (Interscience Pub., NY, 1959) p. 215

[Wal92] W. Waldo, private communication (1992).

[Wig47] E.P. Wigner and L. Eisenbud, Phys. Rev. 72 (1947) 29.

[Wil69] A.S. Wilson, M.C. Taylor, J.C. Legg and G.C. Phillips, Nucl. Phys. A126 (1969) 193.

[Yan48] C.N. Yang, Phys. Rev. 74 (1948) 764.

[Zha86] J.S. Zhang, K.F. Liu, and G.W. Shuy, Phys. Rev. Lett. 57 (1986) 1410.